

Design, Optimization, and Testing of a Combined  
Tri-Axial Polarized Energy Dispersive X-Ray  
Fluorescence and Energy Dispersive X-Ray  
Diffraction System for Biological Sample  
Classification

DESIGN, OPTIMIZATION, AND TESTING OF A COMBINED  
TRI-AXIAL POLARIZED ENERGY DISPERSIVE X-RAY  
FLUORESCENCE AND ENERGY DISPERSIVE X-RAY  
DIFFRACTION SYSTEM FOR BIOLOGICAL SAMPLE  
CLASSIFICATION

BY

ERIC JOHNSTON, B. A Sc.

A THESIS

SUBMITTED TO THE DEPARTMENT OF RADIATION SCIENCES

AND THE SCHOOL OF GRADUATE STUDIES

OF MCMASTER UNIVERSITY

IN PARTIAL FULFILMENT OF THE REQUIREMENTS

FOR THE DEGREE OF

DOCTOR OF PHILOSOPHY

© Copyright by Eric Johnston, September, 2017

All Rights Reserved

Doctor of Philosophy(2017)  
(Radiation Sciences)

McMaster University  
Hamilton, Ontario, Canada

TITLE: Design, Optimization, and Testing of a Combined Tri-Axial Polarized Energy Dispersive X-Ray Fluorescence and Energy Dispersive X-Ray Diffraction System for Biological Sample Classification

AUTHOR: Eric Johnston  
B. A Sc., (Engineering Physics)  
Queen's University, Kingston, Ontario

SUPERVISOR: Dr. Michael Farquharson  
Dr. Soo-Hyun Byun

NUMBER OF PAGES: xxiv, 211

*I dedicate this thesis to my parents, whose love and support made this possible.*

# Abstract

The examination of biological samples yields information regarding the function and structure of the sample tissue. Many non-destructive methods are employed to interrogate biological samples, helping to further our understanding of these complex systems.

A combined Polarized Energy Dispersive X-Ray Fluorescence and Energy Dispersive X-Ray Diffraction system was designed, tested, and optimized for the purpose of classifying biological samples. This system is capable of determining the elemental composition and structural components present within a biological sample. Using two energy dispersive techniques allowed for decreased data acquisition times, and a single x-ray source to be used by both setups.

The system was optimized to improve its performance when measuring biological samples. The x-ray fluorescence spectrometer uses metallic secondary targets that allow for low minimum detection limits in transition metals, which are usually very important to biological tissue function. The x-ray diffraction spectrometer was also optimized to examine structures commonly found in biological samples, while still providing an adjustable range of measurable momentum transfers. Other optimizations performed on both systems provided significant improvements when measuring biological samples.

The functionality of the combined system was tested by measuring several sets of tissue samples. Two sets of cancerous breast tissues, were examined to determine measurable differences between healthy and abnormal tissue. A set of rat organs overloaded with iron were also measured to examine the high customizability and sensitivity of the x-ray fluorescence spectrometer. Lastly, a series of calibration samples were measured to determine minimum detection limits of commonly found elements. All measurements agreed with published literature, and the combined spectrometers showed an improvement in both accuracy and speed over other available spectrometers when measuring biological samples.

# Acknowledgements

First, I would like to thank my supervisor Dr. Michael Farquharson, for giving me the opportunity to work on such an interesting and exciting project. I thoroughly enjoyed working on this project with you. Your input and encouragement were always helpful, and I learned a great deal working with you. I would also like to thank my co-supervisor Dr. Soo-Hyun Byun for all his help and guidance throughout my project. Your knowledge in radiation detection made this project possible.

Thanks to my other research group members, past and present, Alia Al-Ebraheem, Erica Dao, Nourhan Shalaby, Fozeyah Hamzi, Duaa Faisal, and Jenasee Mynerich. Your research helped me understand the importance of my project, and gave me goals to work towards. Working alongside such a wonderful group has been a pleasure. Special thanks also goes to the undergraduate volunteers Latifa Alshaikhqasem, Angelica Manalac, and Yasmeen El-Rayyes for assisting in measuring the final samples.

A special thank you goes out to Justin Bennett and Tony Marrone, and your army of undergraduate students. Your help with designing and machining equipment was invaluable.

I want to thank my officemates in 104/c. The time we spent together working and laughing made these past five years all worthwhile.

Last but certainly not least, I would like to thank my parents, who have always

supported me throughout my endeavours. This Ph.D. wouldn't have been possible without you, love you mom and dad!

# Notation & Abbreviations

**ADXRD** Angular Dispersive X-Ray Diffraction

**EDXRD** Energy Dispersive X-Ray Diffraction

**EDXRF** Energy Dispersive X-Ray Fluorescence

**HOPG** Highly Ordered Pyrolytic Graphite

**HPGe** High-Purity Germanium

**KN** Klein-Nishina

**MC** Monte Carlo

**MDL** Minimum Detection Limit

**PCA** Principal Component Analysis

**PEDXRF** Polarized Energy Dispersive X-Ray Fluorescence

**PLA** Polylactic Acid

**PPM** Parts Per Million

**PVC** Polyvinyl Chloride

**SDD** Silicon Drift Detector

**Si(Li)** Silicon (Lithium Drifted)

**SNR** Signal-to-Noise Ratio

**TXRF** Total Reflection X-Ray Fluorescence

**WDXRF** Wavelength Dispersive X-Ray Fluorescence

**XRD** X-Ray Diffraction

**XRF** X-Ray Fluorescence

# Contents

<b>Abstract</b>	<b>iv</b>
<b>Acknowledgements</b>	<b>vi</b>
<b>Notation &amp; Abbreviations</b>	<b>viii</b>
<b>1 Introduction</b>	<b>1</b>
1.1 Motivation & Objectives . . . . .	1
1.2 Outline . . . . .	9
<b>2 Theory</b>	<b>11</b>
2.1 X-ray Interactions . . . . .	12
2.1.1 Coherent Scattering . . . . .	13
2.1.2 Incoherent Scattering . . . . .	16
2.1.3 Photoelectric Effect . . . . .	19
2.2 X-ray Attenuation . . . . .	22
2.3 X-ray Sources . . . . .	23
2.4 XRF Spectrometry . . . . .	28
2.5 Polarized EDXRF Spectrometry . . . . .	29

2.6	XRD Spectrometry . . . . .	33
2.7	EDXRD Spectrometry . . . . .	35
<b>3</b>	<b>Design &amp; Implementation</b>	<b>38</b>
3.1	PEDXRF Design . . . . .	39
3.2	EDXRD Design . . . . .	49
3.3	Combined PEDXRF & EDXRD Design . . . . .	52
<b>4</b>	<b>Optimization</b>	<b>56</b>
4.1	PEDXRF Optimization . . . . .	56
4.1.1	Secondary Target Model . . . . .	56
4.1.2	Secondary Target Simulations & Experiment . . . . .	67
4.1.3	PEDXRF Geometry . . . . .	77
4.1.4	Fully Optimizing PEDXRF . . . . .	82
4.2	EDXRD Optimization . . . . .	103
<b>5</b>	<b>Application Testing</b>	<b>107</b>
5.1	Reproducibility . . . . .	108
5.2	Minimum Detection Limits . . . . .	113
5.3	Biological Sample Measurements . . . . .	121
5.3.1	Rat Organs . . . . .	122
5.3.2	Breast Tissue . . . . .	130
5.3.3	Lung Tissue . . . . .	143
<b>6</b>	<b>Conclusion</b>	<b>145</b>
6.1	Discussion & Conclusion . . . . .	145

6.2	Future Work . . . . .	150
6.2.1	PEDXRF Improvements . . . . .	151
6.2.2	EDXRD Improvements . . . . .	152
6.2.3	Future Measurements . . . . .	153
<b>A</b>	<b>GEANT4 Code</b>	<b>155</b>

# List of Tables

4.1	A non-exhaustive list of commonly used secondary targets and measurable elements for each <sup>[6]</sup> . . . . .	57
4.2	A table showing the optimal voltage, thickness, and a comparison of the fluorescence to scatter ratio at the optimal thickness to the ‘infinite thickness’ for various commonly used secondary targets. These results were taken from the model described in Section 4.1.1. . . . .	76
4.3	The results of how changing tube potential affects the SNRs in a PEDXRF system. . . . .	92
4.4	A table showing the possible momentum transfer values available at each angle, as well as the momentum transfer value where the tungsten $K_\alpha$ line occurs. . . . .	104
5.1	A table showing the certified values of trace elements found in the LUTS-1 standard reference material <sup>[42]</sup> . Any element not listed will be undetectable with the current PEDXRF setup. . . . .	109
5.2	Statistical results of the PEDXRF reproducibility study. . . . .	111
5.3	Statistical results of the EDXRD reproducibility study. . . . .	113
5.4	MDLs for the PEDXRF using the single measurement technique. All values are given in $\mu g/g$ . . . . .	116

5.5	MDLs for the PEDXRF using the calibration line approach. All values are given in $\mu g/g$ . . . . .	118
5.6	The concentrations of iron, copper, and zinc in LUTS-1, as measured by the PEDXRF system. . . . .	121
5.7	An exhaustive list of all measured elemental and structural components of the healthy and cancerous breast tissues, and whether or not the two population distributions were similar. . . . .	134
5.8	A table showing the statistical difference between the healthy and cancerous breast tissue distributions for different measurement times. The numerical values are p-values representing the likelihood that the two distributions are the same. . . . .	139

# List of Figures

2.1	A transverse electromagnetic wave, showing the direction of travel, and the oscillating electric ( $E$ ) and magnetic ( $B$ ) fields. The polarization of an electromagnetic wave is given by the direction of the E-field. . .	13
2.2	A plot showing the polarized KN differential cross section at three different incident photon energies. $\Psi$ refers the angle between the original photon polarization and the scattered photon direction. The differential cross section has been normalized to $\frac{d\sigma}{d\Omega}(\theta = 0)$ for all cases. . . .	18
2.3	A log-log plot of Photoelectric effect probability as a function of photon energy for a tungsten atom. The sharp jumps are caused by threshold requirement for Photoelectric effect, and are known as absorption edges. Data was taken from XCOM <sup>[17]</sup> . . . . .	20
2.4	The internal structure of an x-ray tube with a rotating anode <sup>[20]</sup> . Electrons emitted by the filament are accelerated to the anode, where they interact to produce x-rays. . . . .	25
2.5	The bremsstrahlung spectrum emitted from an electron with $150keV$ of energy. . . . .	26

2.6	The emission spectra of a tungsten anode x-ray tube with 1mm aluminum filtering <sup>[21]</sup> . The bremsstrahlung continuum and characteristic x-ray peaks are shown. . . . .	27
2.7	A figure showing the probability of polarized x-ray scatter as a function of polar angle. The photon is travelling in the $z$ direction, with a polarization vector in the $x$ direction, denoted by $\hat{\epsilon}$ . The probability for scattering in any direction is shown by the grey rings. If the photon scatters by a angle $90^\circ - \Psi$ in the direction $\hat{R}$ , then the new polarization vector $\hat{\epsilon}'$ will point in the $X$ direction. <sup>[4]</sup> . . . . .	31
2.8	The PEDXRF setup, showing the polarization vectors of the primary and secondary x-ray beams. . . . .	32
2.9	A diagram illustrating the Bragg condition. The path length difference between the two photons is $2d\sin\theta$ . . . . .	34
2.10	An example EDXRD experimental setup. The sample translator allows for different locations on the sample to be measured <sup>[28]</sup> . . . . .	36
3.1	The design of the sample holders used in the combined PEDXRF, EDXRD system. All dimensions are in $mm$ . . . . .	39
3.2	The first PEDXRF setup, with main components labelled. . . . .	40
3.3	Proof of concept experiment, varying $\Psi$ between the sample and detector. The count rate is shown on a log scale. . . . .	41
3.4	The second PEDXRF setup, with main components labelled. . . . .	43
3.5	A background spectrum collected by the second PEDXRF setup, showing the $5 - 11keV$ region. The iron and copper peaks are caused by contamination along the beam path. . . . .	44

3.6	The third PEDXRF setup, with main components labelled. The sample holder cannot be seen from this angle, but sits underneath the detector. . . . .	45
3.7	The adjustable collimators designed for the third PEDXRF setup. Each collimator size had 3 collimators made, so that one could be placed in each aluminum tube. . . . .	45
3.8	A spectrum collected by the third PEDXRF setup, showing the 0 – 15keV region. This measurement was of a 100 $\mu$ g/g iron phantom, excited using a molybdenum secondary target. . . . .	46
3.9	The fourth PEDXRF setup, with main components labelled. This design was made from a solid block of PVC. . . . .	48
3.10	A spectrum collected by the fourth PEDXRF setup, showing the 0 – 15keV region. This measurement was of deionized water phantom, excited using a molybdenum secondary target. . . . .	49
3.11	The final PEDXRF setup, with main components labelled. This design was 3D printed out of PLA, and contained grooves for the sample holder and secondary target holder to be firmly placed. . . . .	50
3.12	The disassembled components of the final PEDXRF system, with labels.	51
3.13	The design of the EDXRD angle block, with important dimensions and available angles shown. Note that all dimensions are in <i>mm</i> . . . . .	52
3.14	The slit collimator used for the EDXRD setup. This collimator has variable width and height, allowing for increased customization. . . .	53

3.15	The diffraction pattern from a calcium carbonate sample measured with two different slit collimator widths. The smaller slit collimator does not produce better results, but instead decreases fluence rate at the detector. . . . .	54
3.16	The entire EDXRD system, showing the detector, collimators, angle block, and sample holder. All components are fixed to the optics table to ensure proper alignment. . . . .	55
4.1	The simplified geometry used to model the effect of secondary target thickness on fluorescence and scatter fluence. The x-rays are incident on a secondary target of thickness $d$ , at a $45^\circ$ angle, and interact at a depth $x$ . The outgoing photons are leaving at an angle $90^\circ$ relative to the incident angle, making the outgoing beam path length $x$ as well. .	60
4.2	The predicted fluorescence response from a molybdenum secondary target as a function of target thickness. The colours represent various x-ray tube potentials. . . . .	63
4.3	The predicted scatter produced from a molybdenum secondary target as a function of target thickness. The colours represent various x-ray tube potentials. . . . .	64
4.4	The predicted fluorescence to scatter ratio produced from a molybdenum secondary target as a function of target thickness. The colours represent various x-ray tube potentials. . . . .	65
4.5	The predicted fluorescence to scatter ratios produced from copper and tin secondary targets as a function of target thickness. The colours represent various x-ray tube potentials. . . . .	66

4.6	The signal processing configuration used in the secondary target thickness experiment. . . . .	68
4.7	The experimental and simulated spectrum of an $^{55}\text{Fe}$ source, detected with an HPGe detector. The main emissions of $^{55}\text{Fe}$ are at 5.898 and 6.490keV. . . . .	70
4.8	Output spectra, for a molybdenum secondary target and a tungsten anode x-ray tube with a potential of 30kV. The counts have been normalized to the height of the molybdenum $K_\alpha$ peak for comparison purposes. The two peaks at 17.5keV and 19.6keV are the $K$ fluorescence peaks of molybdenum. All other features are a result of the tungsten anode x-ray tube spectrum being scattered. . . . .	71
4.9	An example of the curves fit to fluorescence peaks. This example features the $K$ lines of a molybdenum foil. . . . .	72
4.10	The fluorescence produced by a molybdenum secondary target, calculated using the theoretical model (left), simulation (middle), and experimentally (right). All graphs have identical axes to facilitate comparisons. . . . .	74
4.11	The scatter from a molybdenum secondary target, calculated using the theoretical model (left), simulation (middle), and experimentally (right). All graphs have identical axes to facilitate comparisons. . . . .	74
4.12	The fluorescence to scatter from a molybdenum secondary target, calculated using the theoretical model (left), simulation (middle), and experimentally (right). All graphs have identical axes to facilitate comparisons. . . . .	75

4.13	A histogram of the number of detected scatter photons for each degree of polarization, taken at the sample, for various stage two collimator diameters. The counts are normalized to compare the effect of collimator width on the overall degree of polarization. . . . .	80
4.14	A figure showing the degree of polarization as a function of collimator diameter, changing only one stage collimator at a time, keeping the other two stage collimators at $5mm$ . The error bars represent Poisson error in the number of counts. . . . .	81
4.15	A plot of simulated and experimental spectra obtained for an iron phantom from the thinnest Mo secondary target. . . . .	86
4.16	A plot of simulated and experimental spectra obtained for an iron phantom from the thinnest Mo secondary target, zoomed in on the $0 - 15keV$ range. . . . .	87
4.17	A plot of sample XRF counts, normalized to total counts, versus secondary target thickness for a Cu secondary target. The sample fluorescence stops increasing rapidly at approximately $50\mu m$ , and stops increasing altogether at approximately $100\mu m$ . . . . .	88
4.18	A plot of background counts, normalized to total counts, versus secondary target thickness for a Cu secondary target. The number of background counts increases rapidly until approximately $50\mu m$ , and stops increasing altogether at approximately $100\mu m$ . . . . .	89
4.19	A plot of SNR versus secondary target thickness for a Cu secondary target. The optimal thickness is found at $25\mu m$ , with SNR dropping rapidly after approximately $40\mu m$ . . . . .	90

4.20	A plot of experimentally measured SNRs versus secondary target thickness for a Cu secondary target at various input potentials. The optimal thickness is found at $25\mu m$ for all input voltages, and lower potentials provide better SNR on a per photon basis. . . . .	91
4.21	A plot of SNR versus secondary target thickness for a Mo secondary target. The optimal thickness is found at approximately $50\mu m$ , with SNR building up until $50\mu m$ , and dropping rapidly after approximately $80\mu m$ . . . . .	93
4.22	A plot of SNR versus secondary target thickness for a Sn secondary target. The optimal thickness is found at approximately $90\mu m$ , with SNR building up until $90\mu m$ , and dropping off slowly after $90\mu m$ . . .	95
4.23	The sample fluorescence as a function of total solid angle, changing collimators in one stage at a time. . . . .	98
4.24	The background counts as a function of total solid angle, changing collimators in one stage at a time. . . . .	98
4.25	The SNR as a function of total solid angle, changing collimators in one stage at a time. Only the experimental data is shown. . . . .	99
4.26	The SNR divided by total solid angle, as a function of total solid angle, changing collimators in one stage at a time. Only the experimental data is shown. . . . .	101
4.27	A picture of radiochromic x-ray film, showing the x-ray spot size on the sample holder. . . . .	103
4.28	The momentum transfer ranges of some common biological samples. It can be seen that most data lies between $0.5nm^{-1}$ and $3nm^{-1}$ . . . .	105



5.10	A comparison of skin and liver iron concentration in iron overloaded rats. A quadratic curve with $R^2$ is shown. . . . .	123
5.11	A comparison of skin and heart iron concentration in iron overloaded rats. The line of best fit with $R^2$ is shown. . . . .	124
5.12	A comparison of skin and kidney iron concentration in iron overloaded rats. The line of best fit with $R^2$ is shown. . . . .	124
5.13	A comparison of kidney iron concentration measured with the PEDXRF and Huber spectrometers. . . . .	125
5.14	A comparison of heart iron concentration measured with the PEDXRF and Huber spectrometers. . . . .	126
5.15	A comparison of liver iron concentration measured with the PEDXRF and Huber spectrometers. . . . .	126
5.16	A comparison of skin iron concentration measured with the PEDXRF and Huber spectrometers. . . . .	127
5.17	A comparison of skin iron concentration measured with the PEDXRF and Innov-X hand held spectrometers. . . . .	129
5.18	The measured spectra of a normal tissue and its matched tumour tissue, showing notable differences in the potassium, iron and zinc fluorescence peaks. Labels for the other fluorescence peaks can be found in Figure 5.1. . . . .	132
5.19	A histogram showing the distribution of copper in normal and cancerous breast samples. It can be seen that most of the data overlaps. . .	133

5.20	A histogram showing the distribution of zinc in normal and cancerous breast samples. It can be seen that only a small portion of the data overlaps. . . . .	133
5.21	A plot showing the results of performing PCA on the XRF breast data.	136
5.22	A plot showing the results of performing PCA on the XRD breast data.	136
5.23	A plot showing the results of performing PCA on the combined XRF and XRD breast data. . . . .	137
5.24	A plot showing the measured zinc in 19 normal and cancerous breast samples, using the final PEDXRF system. . . . .	139
5.25	A plot showing the results of performing PCA on the final PEDXRF breast data when measured for 600s. . . . .	140
5.26	A plot showing the results of performing PCA on the final PEDXRF breast data when measured for 300s. . . . .	140
5.27	A plot showing the results of performing PCA on the final PEDXRF breast data when measured for 150s. . . . .	141
5.28	A plot showing the results of performing PCA on the final PEDXRF breast data when measured for 60s. . . . .	141
5.29	A plot showing the results of performing PCA on the final PEDXRF breast data when measured for 30s. . . . .	142
5.30	A plot showing the results of performing PCA on the adenocarcinoma of the lung samples. . . . .	144

# Chapter 1

## Introduction

### 1.1 Motivation & Objectives

The scientific community has always been greatly interested in examining biological systems, which consist of vastly complex networks of tissues and organs that work together to perform some common goal, often relying on a series of chemical and physical interactions to function. In order to comprehend how a biological system accomplishes its goal, it is important to understand the underlying chemical and physical interactions that allow it to perform a function. Thus, the study of biological systems is not limited to the field of biology, but also involves chemistry and physics.

Due to their complexity, there are many advantages to examining biological samples using a variety of different techniques. There have been many different approaches developed to examine biological tissues, allowing for a wide range of different properties, structural components, and functions to be examined. To provide a comprehensive understanding of tissue function, both the elemental and structural make-up of the sample, as well as their interactions must be examined. By determining the

elements present in a biological system, and the structures they form, it is possible to learn about how that system behaves<sup>[1]</sup>. This is important not only to the field of biology, but also furthers our knowledge in both biochemistry and medicine. As such, there is a significant need to continue examining biological tissue.

Interrogating biological samples with only one method will not yield enough information to fully understand how those samples function. Instead, utilising several different methods for measuring tissue will yield an increased number of parameters from which the tissue can be classified. One potential area of inquiry is examining functioning biological systems to understand how they work. Another field of research, of particular interest, is the examination of diseased tissue. By investigating and comparing diseased tissue to healthy tissue, changes that are the cause of the disease, or are caused by the disease, can be discovered, studied, and understood. This can provide insight into disease pathology, which can lead to potential techniques for detecting the disease, mitigating its effects, and in some situations, treating it.

One approach to examining biological samples is to use x-rays to probe for elemental and structural compositions of the sample<sup>[1]</sup>. These x-ray methods are usually non-destructive (*i.e.* the sample remains after testing), allowing the samples to be remeasured at a later time, or have further tests performed on it. There are many different x-ray techniques that have been performed on biological samples<sup>[1]</sup>, but two that have been used with great success are X-Ray Fluorescence (XRF) spectrometry, which provides information on the elemental composition of the sample, and X-Ray Diffraction (XRD) spectrometry, which provides information on structures present within the sample<sup>[1-4]</sup>. When combined, these two techniques have been used to

classify tissue as cancerous or healthy, with some success<sup>[2,3]</sup>, leading to a potential method for disease detection. The purpose of this thesis was to design, optimize, and implement instrumentation capable of examining biological samples using two non-destructive x-ray techniques, Polarized Energy Dispersive X-Ray Fluorescence (PEDXRF) spectrometry, and Energy Dispersive X-Ray Diffraction (EDXRD) spectrometry.

XRF spectrometry, usually referred to as just XRF, refers to a large number of different techniques that rely on the characteristics of electronic de-excitation to determine the elemental composition of a sample. X-rays incident on the sample can excite the electrons within the sample. When undergoing de-excitation, the excited atom can emit an x-ray (known as a characteristic x-ray), whose energy is dependent on the element of the excited atom. As such, the goal of performing an XRF experiment is to determine which elements are present within a sample, and their concentrations<sup>[4,5]</sup>. There are several different types of XRF, each with their advantages, however they are all used to examine elemental make-up of the sample.

Energy Dispersive X-Ray Fluorescence (EDXRF) typically involves using a polychromatic x-ray source, usually an x-ray tube, to excite the sample. By having more than one input energy, a wide range of elements can be examined at the same time. EDXRF is generally one of the quickest forms of XRF, since x-ray tubes can produce high intensity beams and a large energy range can be measured simultaneously<sup>[5]</sup>. However, the emission spectra will not only contain the characteristic x-rays required to determine the elemental composition, but also an amount of background signal, caused by x-rays scattering off of the sample. Since the source is polychromatic, the background will be present at all energies up to the maximum tube voltage, which can

sometimes outnumber the measured fluorescence x-rays at that energy. Thus, this background can make it more difficult to determine the amount of characteristic x-rays measured, making it harder to detect elements present in low concentrations<sup>[4,5]</sup>.

In order to calculate the concentration of a specific element present within a sample, the number of characteristic x-ray must be determined from the recorded spectrum. While this is not a problem with elements that comprise a large portion of the sample, if the element composes a very small percentage of the sample it will be harder to measure the characteristic x-ray peak, due to the background noise. These elements are usually referred to as trace elements, since they have very small concentrations. The difficulty with detecting trace elements is that the number of photons fluoresced by them will be small. If number of fluoresced x-rays are significantly lower than the number of scattered photons, the fluorescence peak cannot be identified in the spectrum. The Minimum Detection Limit (MDL) is the lowest concentration of an element that can be detected within a sample. The MDL gives a measure of how precise measurements from a certain detection system can be, as well as a way to compare different methods of trace element quantification to each other. The detection limit of an EDXRF setup is limited by the amount of scatter incident on the detector, compared to the amount of fluorescence measured, since the two combine to form the spectrum. Thus, the two main approaches to improving MDLs is to increase the signal by making fluorescence more probable, or reduce the background by eliminating scattered photons from the spectrum.

XRF systems can typically measure trace elements in concentrations of a few Parts Per Million (PPM) or even sub PPM depending on the technique used. Of all the forms of XRF, EDXRF has some of the worst MDLs. This is due to the fact that it

has a high amount of scatter that interferes with the fluoresced signal. In contrast, Wavelength Dispersive X-Ray Fluorescence (WDXRF) and Total Reflection X-Ray Fluorescence (TXRF) have much lower detection limits than EDXRF, since they actively reject scatter via their experimental configurations. To reject this scatter, these setups requires specific geometrical considerations, expensive components, and increased counting times when compared to EDXRF systems<sup>[6]</sup>. Another method which improves MDLs is PEDXRF, which can have detection limits on the same order as WDXRF and TXRF. PEDXRF makes use of the characteristics of polarized x-ray interactions to actively reject scatter, while still maintaining the key characteristics of EDXRF; a wide range of measurable elements and short acquisition times. In addition, the detection limits are also comparable to destructive methods of elemental analysis, making PEDXRF a powerful technique<sup>[6,7]</sup>.

PEDXRF is used in many different fields of research to perform non-destructive testing. Due to its low MDLs in the transition metals range, it is commonly used to examine metallic substances, such as historical artifacts<sup>[8,9]</sup>, geochemical samples<sup>[10]</sup>, and in environmental science applications<sup>[11,12]</sup>. Its uses are not limited to these fields, as PEDXRF has been used previously to search for lead in bone<sup>[13]</sup>, and EDXRF has been used to examine soft tissues<sup>[2]</sup>.

When discussing biological samples, the trace elements can often have a large impact on tissue function. Specifically, many transition metals are found in trace amounts in biological tissue, but play a major role in functionality of the tissue<sup>[1,2]</sup>. Looking at changes in transition metals between similar types of tissue can therefore be used to determine functional differences, which can be caused by diseases, genetic disorders, or external factors. In other cases, elements not usually found in tissue may

be stored if those elements have a similar chemical structure to something commonly stored.<sup>[1,2]</sup> When this happens, the tissue can be examined to search for accidental exposures to rare elements. Therefore, using a PEDXRF system devoted to examining soft tissue should allow for a quick, yet accurate interrogation of these samples, due to its high sensitivity for transition metals.

XRF experiments are also commonly performed on biological samples to look for heavy metal contamination, which usually comes from external sources<sup>[1,13]</sup>. In these cases, a PEDXRF system will still be capable of accurately measuring these samples. While PEDXRF systems provide the best MDLs in the transition metals range<sup>[9,10]</sup>, they are still quite sensitive to heavy metals<sup>[8-12]</sup>. As such, a PEDXRF system will be able to accurately measure the elemental composition of trace elements found in all biological samples, while maintaining the multi-elemental analysis and low data acquisition times of EDXRF systems.

In addition to performing the PEDXRF experiment on the biological samples, which provides detailed information on the elemental composition, this system also allows for XRD spectrometry to be performed. XRD spectrometry, usually referred to as just XRD, is used to gather information on the structure of a sample. XRD relies on the wave-like nature of x-rays to produce interference patterns, caused by x-rays interacting with each other. As x-rays traverse a material they will not always interact at the same depth, but instead can interact with many atoms along the beam path. If two x-rays are scattered in the same direction, but one travelled further, the x-rays may be out of phase, which will cause a destructive interference effect. Conversely, if the two x-rays end up in phase, a constructive interference effect is seen. Since x-rays interact with individual atoms, the distance between neighbouring

atoms in the sample are what determine the changes in path length, and thereby the diffraction pattern produced<sup>[4]</sup>. Thus, the net result of an XRD experiment is related to the spacing of the atoms present in the sample, and therefore the structure of multi-elemental components present in the sample.

The two basic types of XRD are Angular Dispersive X-Ray Diffraction (ADXRD) and EDXRD<sup>[4]</sup>. ADXRD involves using a mono-energetic beam, measuring the resultant x-ray intensity at various angles to produce the diffraction pattern. This is usually accomplished by moving the detector or x-ray source during data acquisition, or employing large, multi-element detectors, capable of measuring the x-ray intensity at several locations. Instead, EDXRD uses a polychromatic x-ray source, allowing for several different atomic spacings to be interrogated simultaneously, without the need for moving parts or multi-element detectors. Once again, the use of polychromatic x-rays beams allow for higher intensity beams to be used, leading to decreased data acquisition times. However, there are a few drawbacks to using EDXRD over ADXRD. The diffraction patterns produced are subject to increased noise, caused by incoherently scattered and fluoresced x-rays. Additionally, the analysis requires the additional step of normalizing to the source intensity at each energy to make results comparable to other methods of XRD. In general, EDXRD systems provide less accurate measurements of atomic spacings, while providing the benefit of requiring no moving parts, and having a shorter data acquisition time<sup>[4]</sup>.

XRD experiments are commonly used on highly structured materials, such as crystals and powders<sup>[4]</sup>. The materials contain repeated patterns in the spacing of atoms, where the spacing along a single beam path will be consistent (in the case of crystals) or an average of all spacings (for powder diffraction). The interference

patterns produced will have very high intensity where constructive interference occurs, and almost no intensity where destructive interference occurs, creating very distinct diffraction patterns. In contrast, not all biological samples produce obvious diffraction patterns, unless there is significant underlying structure. Nevertheless, EDXRD has been successful in discovering certain structures within various biological samples, *e.g.* bone<sup>[14,15]</sup> and soft tissues<sup>[2,3]</sup>. Since most biological samples do not produce distinct diffraction patterns, the lower accuracy of EDXRD experiments does not greatly impact the results.

The main goal of this project was to design, optimize, and test a combined PEDXRF and EDXRD system that can be used to examine the elemental composition and structure of biological samples. This system was optimized to measure trace transition metals present in the sample, and determine whether underlying structure is present in the sample. Altogether, this information can be combined to examine diseased tissue, improving our understanding of how the disease functions, and providing insight into how we might diagnose, treat, or track disease progression.

There are many different techniques researchers use to examine biological samples, including destructive chemical processes, and many other non-destructive techniques not mentioned, some of which use x-rays<sup>[1]</sup>. Out of these, PEDXRF and EDXRD provide complimentary information, and have been combined into a single system capable of using many of the same components. While there may be other methods that provide similar or information, this combined technique has shown promise in examining cancerous tumours<sup>[3]</sup>, where it allows for differentiation between cancerous and healthy tissue<sup>[2,3]</sup>. By using a high powered x-ray tube, this system can provide fast measurements, allowing for a larger quantity of samples to be measured, improving

tissue classification libraries. As such, this combined system should be extremely useful for examining large quantities of biological samples, providing fast, accurate results.

## 1.2 Outline

This thesis is broken into six chapters. Following this introduction, Chapter 2 thoroughly describes the theory behind PEDXRF and EDXRD. Both techniques rely heavily on exploiting characteristics of x-ray interactions which will be discussed in-depth. When necessary, the effects of x-ray polarization will also be discussed. This chapter includes a brief section covering the methods of producing the x-rays required for these techniques. The methodology of the two techniques, PEDXRF and EDXRD, will also be described here. Both require very specific geometries to function, which will be explained in-depth, as separate systems.

Chapter 3 discusses the design of the combined PEDXRF and EDXRD system. This covers the iterative design process of each system independently, as well as how the two were combined. The process of combining the two systems discusses specific design considerations made to accommodate the required geometries of the two systems simultaneously. Earlier models of each system will be presented and the successes and failures of each will be examined, leading to the final design, discussing critical choices made to the overall design of the system.

Optimizations made during the design and implementation of the systems are discussed thoroughly in Chapter 4. These optimizations were fully realized in the final design, but a more in-depth discussion of them is presented in this chapter. Significant improvements to the PEDXRF technique are presented here, as well as

optimizations of the diffraction system for soft tissue analysis. Following that, the initial testing of these systems is presented here. These tests were used to ensure that the system was functioning properly, and capable of producing reliable results.

Chapter 5 covers the application testing of the combined PEDXRF and EDXRD system. These tests include determining MDLs for several elements of interest and measurements of standard reference materials. Finally, this chapter concludes with measurements on several sets of biological samples, proving the success of this project. These results are compared to measurements taken on other XRF and XRD setups, providing a comparison between the different techniques used, and the overall usefulness of this setup.

Chapter 6 is an in-depth discussion on the results of the application testing, followed by a conclusion and considerations for future work. This discussion refers to potential uses of the combined technique, its strengths and shortcomings, as well as improvements that could be made in the future.

# Chapter 2

## Theory

In order to properly describe both PEDXRF and EDXRD, various x-ray interactions must be explored. PEDXRF requires a thorough understanding of the Photoelectric effect as well as polarized x-ray scattering, while EDXRD makes use of non-polarized x-ray scattering characteristics<sup>[4,5]</sup>. This chapter discusses x-ray interactions, with a focus on the interactions relevant for PEDXRF and EDXRD. Interactions that have a high energy threshold, or a very small interaction probability at low energies will not be discussed. Pair production can be ignored, since it requires the photons to have at least  $1.022MeV$  of energy, and the x-rays used in this system have a maximum energy of  $160keV$ , meaning that pair production will never occur. Similarly, all photonuclear and two-photon interactions can be ignored since energies and fluence rates are sufficiently low<sup>[4,5]</sup>.

Following the discussion of x-ray interactions, the methods of producing x-rays will be briefly examined. The advantages and disadvantages of each method will be presented, as well as the energies, fluence rates, and polarizations of each production method.

Lastly, the experimental configurations for PEDXRF and EDXRD will be outlined. This will cover the typical geometries associated with each technique, the interaction processes that are required for the technique to work, and any other processes that may interfere or alter the results. The combination of the two techniques will be discussed in Chapter 3.

## 2.1 X-ray Interactions

X-rays are a form of ionizing electromagnetic radiation, and are produced by electronic transitions, *i.e* when electrons change energy states or accelerate. Because of this, the energy range of x-rays is not strictly defined, however, typical x-ray energies are above ultraviolet and below gamma-rays, roughly  $100eV$  to  $200keV$ <sup>[4,5]</sup>. Due to their short wavelengths, x-rays may behave as a wave, or as a particle referred to as a photon. When exhibiting wave-like properties, x-rays act as transverse electromagnetic waves, meaning that they have an oscillating electric ( $E$ ) and magnetic ( $B$ ) field which are mutually perpendicular to the direction of travel and each other, as shown in Figure 2.1. By convention, the polarization of an x-ray is taken to be the direction of the E-field<sup>[4,5]</sup>. Knowing the polarization and direction of the x-ray allows for the direction of the B-field to be determined, since they are mutually perpendicular. As such, there is no need to name or provide information on the direction of the B-field.

X-rays typically interact via the Coulomb force, and thus can interact with any charged particle, although most x-ray interactions occur with the electrons of an atom<sup>[4,5]</sup>.

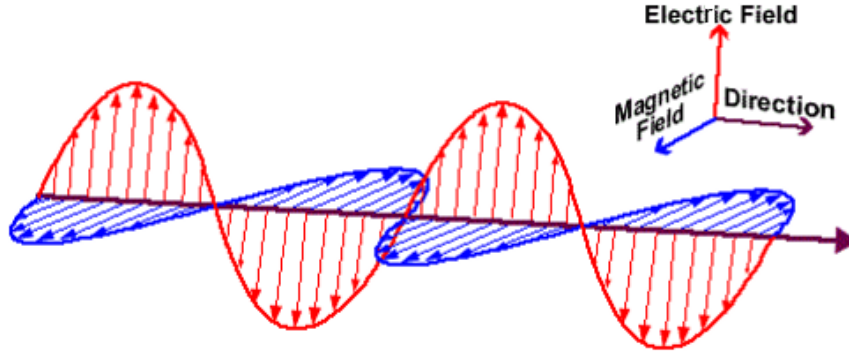


Figure 2.1: A transverse electromagnetic wave, showing the direction of travel, and the oscillating electric ( $E$ ) and magnetic ( $B$ ) fields. The polarization of an electromagnetic wave is given by the direction of the E-field.

### 2.1.1 Coherent Scattering

The first x-ray interaction of interest is known as coherent scattering, which can occur when an x-ray interacts with electrons bound to a nucleus. The defining characteristic of coherent scattering is that the x-ray energy remains unchanged throughout, only the direction is changed.

A precursor to this effect was first examined by Thomson, who looked at the interaction of a photon with a free electron, referred to as Thomson scattering. In Thomson scattering, the free electron is influenced by the oscillating E-field of the x-ray, which causes the electron to oscillate. This electron experiences an acceleration of  $e\vec{E}/m_e$ , which causes it to radiate as a dipole, resulting in the scattered x-ray. By looking at the time averaged power of dipole radiation per unit solid angle, the differential cross section can be determined as shown in Equation 2.1. It is worth noting that for a polarized beam of x-rays, there is a zero probability of a scattered

photon being emitted in the direction of polarization.

$$\left(\frac{d\sigma}{d\Omega}\right)_{T,pol} = \frac{e^4}{m_e^2 c^4} \sin^2 \Psi = r_e^2 \sin^2 \Psi \quad (2.1)$$

Where:

$\left(\frac{d\sigma}{d\Omega}\right)_{T,pol}$  is the polarized Thomson scattering differential cross section

$\Psi$  is the angle between emitted photon and polarization of the original photon

$r_e = e^2/m_e c^2$ , the classical electron radius

In order to obtain the non-polarized Thomson scattering cross section, Equation 2.1 should be averaged over all possible incident polarizations. In the case where the original photon is polarized perpendicularly to the polar scatter angle,  $\Psi = \pi/2$  for all azimuthal angles. For the case where the original photon is polarized in the same plane as the polar scatter angle,  $\Psi = \pi/2 - \theta$  for all azimuthal angles. Averaging these two values leads to the non-polarized Thomson scattering cross section, shown in Equation 2.2.

$$\left(\frac{d\sigma}{d\Omega}\right)_{T,unpol} = \frac{r_e^2}{2} (1 + \cos^2 \theta) \quad (2.2)$$

Moving to a more realistic situation, coherent scattering governs the scattering between an x-ray and an atom. In this case, a photon with incident wave vector  $\vec{k}_\gamma$  is absorbed by the atom, followed by the emission of a photon with wave vector  $\vec{k}'_\gamma$ , with the initial and final states of the atom being the ground state. After a formal derivation, the differential cross section for coherent scattering is shown in

Equation 2.3.

$$\left(\frac{d\sigma}{d\Omega}\right)_{coh} = r_e^2 \langle 0 | \sum_{j=1}^Z e^{i\vec{q}\cdot\vec{r}_j} | 0 \rangle^2 (\hat{\epsilon} \cdot \hat{\epsilon}')^2 \quad (2.3)$$

Where:

$\left(\frac{d\sigma}{d\Omega}\right)_{coh}$  is the coherent scattering differential cross section

$|0\rangle$  is the ground state wavefunction for the atom

$\vec{q} = \vec{k}_\gamma - \vec{k}'_\gamma$ , the momentum transfer

$\hat{\epsilon}$  is the polarization direction original photon

$\hat{\epsilon}'$  is the polarization direction scattered photon

Noting that the previously used angle  $\Psi$  refers to the angle between the original photon polarization and the final direction, the term  $(\hat{\epsilon} \cdot \hat{\epsilon}')^2$  can be written as  $\sin^2\Psi$ . Thus, Equation 2.3 simplifies to Equation 2.4.

$$\left(\frac{d\sigma}{d\Omega}\right)_{coh} = \left(\frac{d\sigma}{d\Omega}\right)_T |F(q)|^2 \quad (2.4)$$

Where:

$F(q) = \langle 0 | \sum_{j=1}^Z e^{i\vec{q}\cdot\vec{r}_j} | 0 \rangle$ , known as the form factor

Implementing the form factor  $F(q)$  allows for a much simpler representation and calculation of the coherent scattering differential cross section. On a more physical scale, the form factor represents a measure of the number of electrons that interact coherently to produce the scattering effect, with the limiting cases of  $F(0) = Z$  and  $F(q \rightarrow \infty) = 0$ . Of high importance is that the polarized scattering characteristics are identical to those of Thomson scattering, meaning that the scattered photon cannot be emitted in the direction of polarization of the original photon.

The other two interesting features of coherent scattering are the energy and atomic number dependence. While Thomson scattering was calculated for a single electron, an atom with atomic number  $Z$  has  $Z$  electrons to interact with, and a nucleus with charge  $Ze$ , and a mass that approximately depends linearly on  $Z$ . Taking these into account, to a first order approximation, the coherent scattering differential cross section varies as  $Z^2$ . Similarly, considering all effects, the differential cross section varies roughly as  $E^{-2}$ , except at low energies where the form factor term dominates<sup>[4]</sup>.

### 2.1.2 Incoherent Scattering

The next interaction of interest is incoherent scattering, where the scattered photon energy differs from the initial photon energy. While there are other forms of incoherent scattering, only Compton scattering is relevant in this energy range. Once again, this interaction occurs between an x-ray and an entire atom, but usually only considers a single electron at first.

The Compton scattering equation, shown in Equation 2.5, is the kinematic solution to a photon scattering by an angle  $\theta$  from a loosely bound electron. In this derivation, it is assumed the binding energy of the electron is so small compared to its final energy, that it may be ignored, hence the term loosely bound. After the interaction, the electron is no longer bound, and is free to move with an energy  $\epsilon = E_\gamma - E'_\gamma$ .

$$E'_\gamma = \frac{E_\gamma}{1 + \frac{E_\gamma}{m_e c^2} (1 - \cos\theta)} \quad (2.5)$$

The differential cross section for this particular interaction was first calculated by

Klein and Nishina, and is shown in its polarized form in Equation 2.6<sup>[16]</sup>.

$$\left(\frac{d\sigma}{d\Omega}\right)_{KN,pol} = \frac{r_e^2}{4} \left(\frac{E'_\gamma}{E_\gamma}\right)^2 \left(\frac{E'_\gamma}{E_\gamma} + \frac{E_\gamma}{E'_\gamma} - 2 + 4\sin^2\Psi\right) \quad (2.6)$$

The relationship between polar scattering angle and cross section is much more difficult to examine analytically in this case, since it is found in both  $E'_\gamma$  and  $\Psi$ . Instead, Figure 2.2 shows the polarized Klein-Nishina (KN) differential cross section as a function of  $\Psi$ . Unlike coherent scattering, where the cross section drops to zero when  $\Psi = 0^\circ$ , the KN cross section does not. In the energy range of interest however, the KN cross section still reaches a minimum, but this value increases with increased incident photon energy. Thus, for sufficiently low energies, this cross section may be approximated as a  $\sin^2\Psi$  relationship.

As before, to determine the cross section for non-polarized photons, the average of the two polarizations can be taken, resulting in Equation 2.7. This cross section closely resembles the shape of the coherent scattering case, but becomes more forward scattering for higher energies. As with the polarized case, the deviation from the expected case is fairly small at the energies of interest.

$$\left(\frac{d\sigma}{d\Omega}\right)_{KN,unpol} = \frac{r_e^2}{2} \left(\frac{E'_\gamma}{E_\gamma}\right)^2 \left(\frac{E'_\gamma}{E_\gamma} + \frac{E_\gamma}{E'_\gamma} - \sin^2\theta\right) \quad (2.7)$$

Moving onto the case where the electron is bound to an atom, another form factor term,  $S(q, Z)$ , is added to correct for contributions of the other atomic electrons and nucleus. Thus, the correct form for Compton scattering cross section is shown in Equation 2.8. Once again, this form factor does not affect the angular distribution of

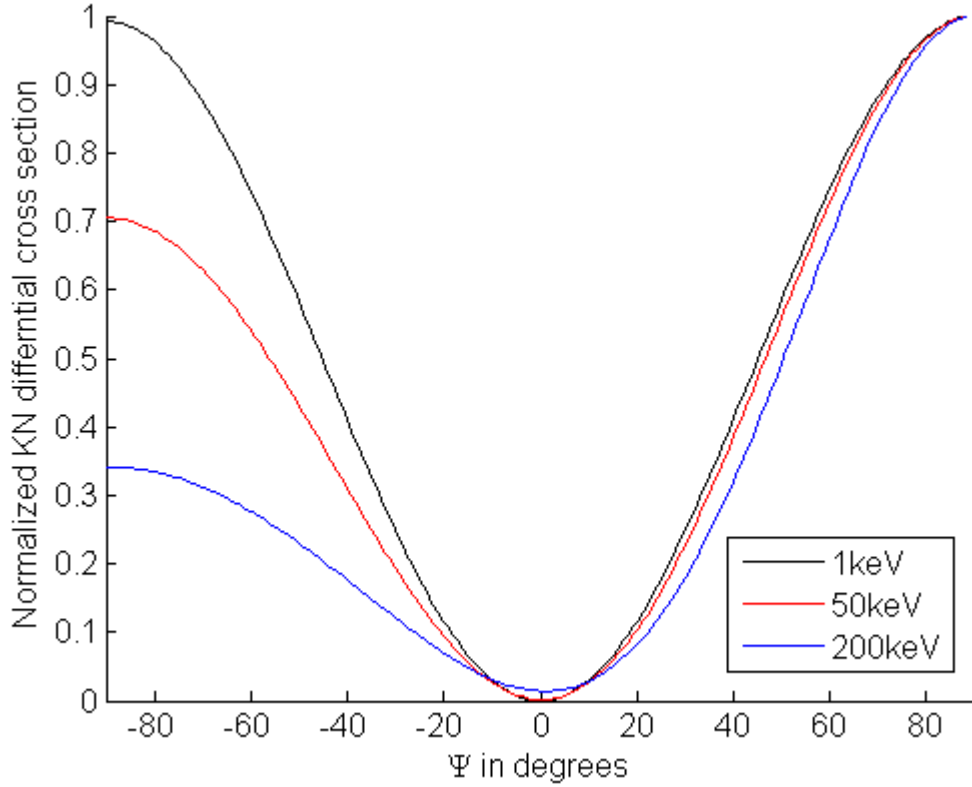


Figure 2.2: A plot showing the polarized KN differential cross section at three different incident photon energies.  $\Psi$  refers the angle between the original photon polarization and the scattered photon direction. The differential cross section has been normalized to  $\frac{d\sigma}{d\Omega}(\theta = 0)$  for all cases.

the scattered photons.

$$\left(\frac{d\sigma}{d\Omega}\right)_{inc} = S(q, Z) \left(\frac{d\sigma}{d\Omega}\right)_{KN} \quad (2.8)$$

As for energy and atomic number dependence, Compton scattering is roughly independent of  $Z$  over a wide range of elements, instead depending on electron density<sup>[4]</sup>. At low energies, the cross section is dominated by binding energy effects,

causing an increase in cross section with incident photon energy, while at high energies, the electrons may be considered free, and the cross section decreases with increased energy<sup>[4]</sup>.

### 2.1.3 Photoelectric Effect

The last interaction of interest is the Photoelectric effect. This interaction also occurs between a bound electron and a photon, except this time the electron is not loosely bound. In the Photoelectric effect, the photon is absorbed completely, transferring its energy to the electron, ejecting it from the atom. If the photon energy is below the binding energy, then the Photoelectric effect will not occur, thus there is the condition that  $E_\gamma - E_b > 0$  for the Photoelectric effect to be possible. If the photon energy is significantly above the binding energy of the innermost electrons, interaction with the inner electrons dominate the interaction, and the cross section can be approximated by Equation 2.9. In this case,  $\theta$  refers to the polar emission angle of the emitted electron, thus the electron direction is dependent on photon polarization.

$$\left(\frac{d\sigma}{d\Omega}\right)_{PE} = 2\sqrt{2}r_e^2 Z^5 \left(\frac{m_e c^2}{E_\gamma}\right)^{7/2} \sin^2\theta \quad (2.9)$$

Due to the photon energy threshold caused by the binding energy effects, which depend on atomic number, and relativistic effects not taken into account in Equation 2.9, the Photoelectric effect cross section is usually said to depend on  $Z^{\sim 3.5-4.5}$ . Additionally, the energy dependence is non-trivial due to the threshold requirement. A plot of the Photoelectric cross section, as a function of energy is shown in Figure 2.3, for a tungsten atom<sup>[17]</sup>.

After undergoing the Photoelectric effect, the atom is left with a vacancy in an

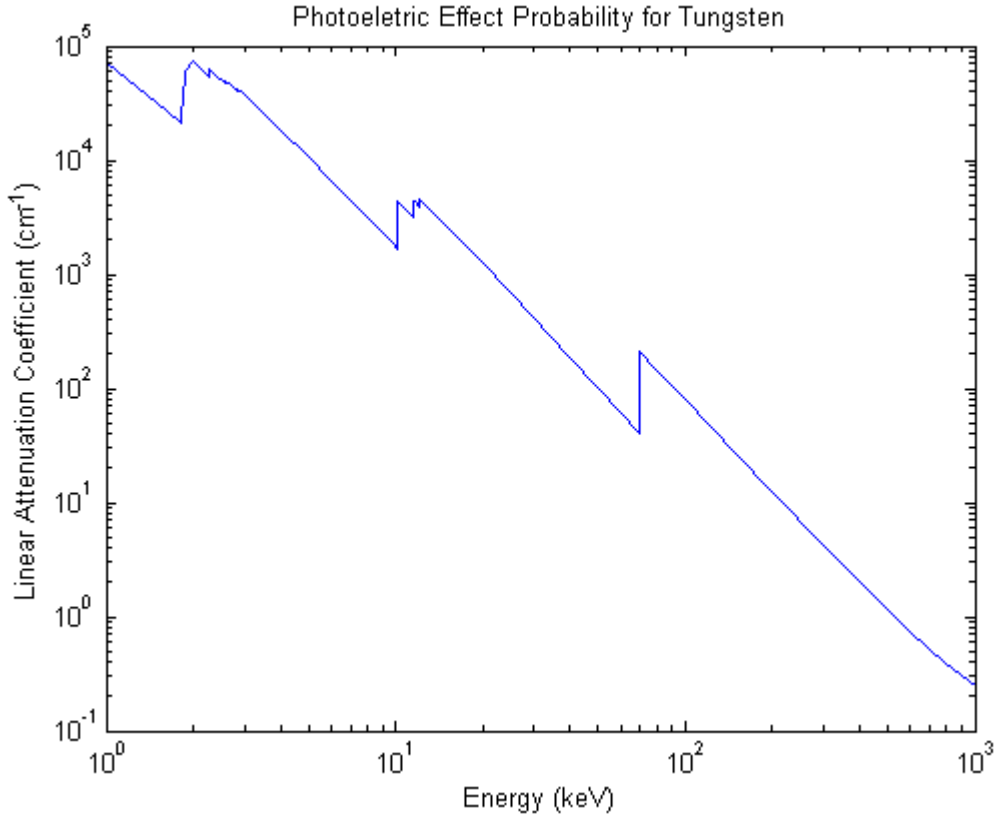


Figure 2.3: A log-log plot of Photoelectric effect probability as a function of photon energy for a tungsten atom. The sharp jumps are caused by threshold requirement for Photoelectric effect, and are known as absorption edges. Data was taken from XCOM<sup>[17]</sup>.

electron orbital. In general, the Photoelectric effect interacts preferentially with inner shell electrons, making the vacancy in an inner shell orbital, leaving the atom in an excited state. The atom would prefer to be in its ground state, so it will de-excite by having an outer shell electron fill the inner shell vacancy. This process releases energy, which may be emitted in the form of a fluoresced x-ray, known as a characteristic x-ray. The atom may also de-excite via a process known as the Auger effect.

Characteristic x-ray fluorescence occurs when an inner shell electron orbital is filled by an electron from an outer shell. Since the binding energies of electron orbitals

are dependent on the atomic number, the differences in energy between orbitals will be different for each element<sup>[4]</sup>. As an atom de-excites, the fluoresced x-ray will have an energy characteristic to that element. Examining characteristic x-rays can therefore be used to determine the element that contained the vacancy. Although this process occurs after the Photoelectric effect, the directions and polarizations of the initial photon and emitted electron have no effect on the direction or polarization of the characteristic x-ray. Instead, this photon will be emitted isotropically, with a randomly defined polarization<sup>[6,7,18,19]</sup>.

A naming convention has been adopted to differentiate between characteristic x-rays from the same element. Atoms have several different orbitals that the electrons may be found in, which can be further broken into subshells. Thus, the convention describes the initial and final shells of the electron, fully defining the energy of the characteristic x-ray. First, the characteristic x-ray is given a letter depending on the final shell of the electron, which is also the shell with the vacancy to be filled. Historically, the most tightly bound shell is given the letter K, with L being the next tightly bound, then M, *etc.* Next, a subscript is added depending on how many shells above the final shell the electron starts in,  $\alpha$  for one shell,  $\beta$  for two, and  $\gamma$  for three. Finally, if there are subshells involved, the subscript is appended with a Roman numeral so they can be distinguished. As an example, the characteristic x-ray emitted from an electron moving from the L-shell to the K-shell would be referred to as a  $K_\alpha$  x-ray, while the transition from N-shell to L-shell results in an  $L_\beta$  x-ray.

This process is always competing against a process known as the Auger effect. Instead of emitting an x-ray to conserve energy, an outer shell electron may be ejected instead. The probability of either characteristic x-ray emission or Auger electron

emission depends heavily on the atomic number. This ratio, usually quoted as the probability of characteristic x-ray emission from the K-shell, per electron vacancy in the K-shell, is shown in Equation 2.10. The second half of Equation 2.10 was determined empirically, but shows that as  $Z$  increases, so does the probability of characteristic x-ray fluorescence. When combined with the strong dependence of Photoelectric effect with  $Z$ , characteristic x-ray fluorescence yield increases quite rapidly with atomic number.

$$\omega_K = \frac{\# \text{ of fluoresced } x - \text{ rays}}{\# \text{ of inner shell vacancies}} = \frac{(Z + 0.85)^4}{(32.5)^4 + (Z + 0.85)^4} \quad (2.10)$$

Where:

$\omega_k$  is the probability of K-shell fluorescence as opposed to Auger electron emission

## 2.2 X-ray Attenuation

While each x-ray interaction is a discrete process, if a statistically significant number of x-rays are incident on a sample, then an interaction probability can be applied. The interaction coefficient  $\mu$ , often referred to as the linear attenuation coefficient, can be calculated using the differential cross section, solid angle, and target number density, as shown in Equation 2.11. While not explicitly stated above, differential cross-sections are energy dependent, so  $\mu$  is only valid for a single energy.

$$\begin{aligned} d\mu &= n_T \left( \frac{d\sigma}{d\Omega} \right) d\Omega \\ \mu &= n_T \int d\phi \int d\theta \sin\theta \left( \frac{d\sigma}{d\Omega} \right) \end{aligned} \quad (2.11)$$

$\mu$  is only defined for a single cross section, so it usually given a subscript for each interaction. If an attenuation coefficient for multiple interactions is to be calculated, the individual coefficients can be added as shown in Equation 2.12.

$$\mu_{tot} = \mu_{PE} + \mu_{coh} + \mu_{inc} + \dots \quad (2.12)$$

If an x-ray is incident on some target material, then the beam is attenuated according to the Beer-Lambert law<sup>[4]</sup>, shown in Equation 2.13.

$$I/I_0 = e^{-\mu x} \quad (2.13)$$

Where:

$I/I_0$  is the ratio of beam intensity to initial beam intensity

$x$  is the distance travelled in the material.

## 2.3 X-ray Sources

In order to perform x-ray based experiments, a strong source of x-rays must be used. These sources usually fall into one of three groups, radioisotope sources, x-ray tubes, or synchrotron radiation. Each x-ray source has its own advantages and disadvantages, as well as applications well-suited to each.

Radioisotope x-ray sources are perhaps the simplest x-ray source that can be used for x-ray based techniques<sup>[4,5]</sup>. These sources rely on the radioactive decay of elements to produce the x-rays required for experiments. After undergoing radioactive decay, the atom may be left in an excited state, producing x-rays and gamma-rays which may be used to perform experiments. Both the x-rays and gamma-rays from the source can

be used, as they are both electromagnetic waves. Radioisotope sources provide very specific x-ray energies which are fixed for a given radioisotope, suitable for experiments that require mono-energetic x-rays. These x-rays are non-polarized and are usually emitted isotropically. These sources also tend to be small and lightweight, making them very easy to transport and implement. However, radioisotope sources depend on radiation emission to produce x-rays, resulting in a limit to their fluence rates based on the size and half-life of the source; the source activity also decay exponentially over time. As such, radioisotopes tend to have the lowest x-ray fluence rate of all x-ray sources.

Another common x-ray source is an x-ray tube<sup>[4,5]</sup>. An example figure of an x-ray tube is shown in Figure 2.4. X-ray tubes are an evacuated tube with a high potential placed between a cathode and anode. Electrons are emitted from the filament (cathode) via thermionic emission, starting with effectively zero kinetic energy. These electrons are then accelerated towards the anode due to the applied potential. When they reach the anode, they will have a kinetic energy equal to  $e \cdot V$ , where  $V$  is the applied potential. Once the electrons hit the anode, they will undergo one of two interactions, either radiative stopping, or a collision interaction with an atomic electron. In either case, the electron loses energy, and can produce x-rays to ensure energy conservation.

When moving electrons are slowed, the energy may be conserved via the emission of bremsstrahlung x-rays. In the case of x-ray tubes, the bremsstrahlung is caused by partial or complete stopping of accelerated electrons by the anode. As such, the maximum energy x-ray emitted via bremsstrahlung will be equal to the kinetic energy of the electron,  $e \cdot V$ . If less energy is emitted, the electron will still have

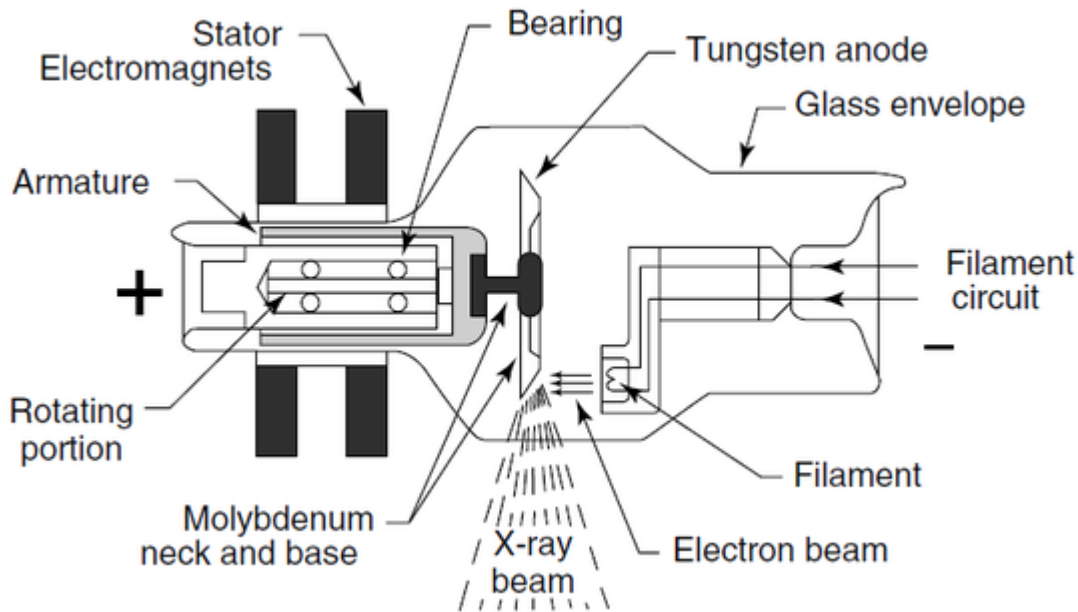


Figure 2.4: The internal structure of an x-ray tube with a rotating anode<sup>[20]</sup>. Electrons emitted by the filament are accelerated to the anode, where they interact to produce x-rays.

kinetic energy, which may be emitted as a second bremsstrahlung x-ray. As a result, the number of emitted x-rays at each energy is inversely proportional to energy. Low energy x-rays are subject to self-attenuation effects, resulting in the typical bremsstrahlung shape shown in Figure 2.5. While all x-rays will be attenuated by the anode material, the decrease in attenuation coefficients at higher energies makes the effect more pronounced in lower energy x-rays.

The other interaction that produces x-rays is inelastic scattering of the accelerated electron with an anode electron. If the accelerated electron has energy greater than the binding energy of the anode electron, the anode electron may be emitted, resulting in a vacancy in an atom's electron orbital. The atom will undergo de-excitation, possibly emitting a characteristic x-ray. Analogous to the Photoelectric effect, if the

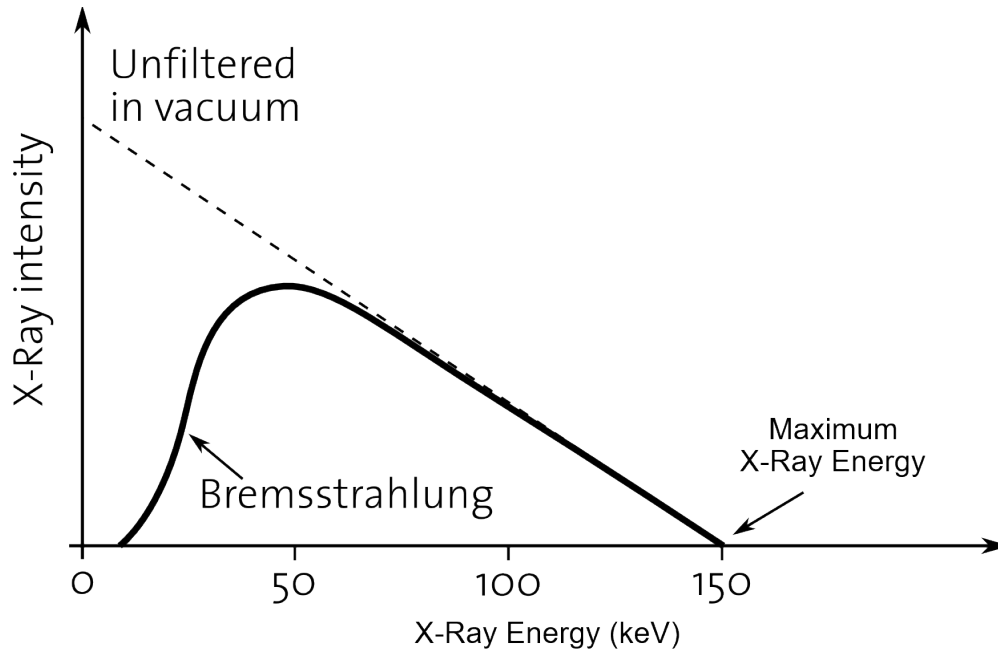


Figure 2.5: The bremsstrahlung spectrum emitted from an electron with  $150\text{keV}$  of energy.

electron energy is below the absorption edge of the anode material, no characteristic x-rays will be emitted.

The x-rays emitted from an x-ray tube are also filtered. Filters lower the beam intensity via attenuation, usually dominated by the Photoelectric effect. Since the Photoelectric effect probability is greatly reduced at increased energies, filters generally act to remove low energy x-rays from the spectrum. Together, the characteristic x-ray emission and bremsstrahlung, combined with filters, make the expected x-ray tube output spectrum, shown in Figure 2.6 for a tungsten anode. A polychromatic source can be made mono-energetic through the use of x-ray optics known as a monochromator<sup>[4,5]</sup>, however these devices greatly reduce fluence rates.

The energetic electrons incident on the anode cause it to heat up, which limits x-ray fluence rate that can be produced. To combat this, most x-ray tubes have either

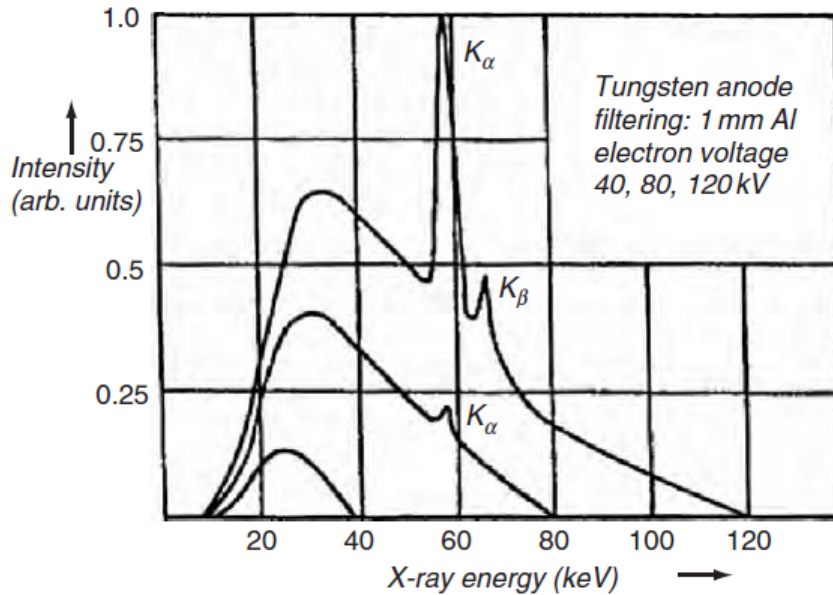


Figure 2.6: The emission spectra of a tungsten anode x-ray tube with 1mm aluminum filtering<sup>[21]</sup>. The bremsstrahlung continuum and characteristic x-ray peaks are shown.

a rotating anode or active cooling of the anode. In these cases, the fluence rate of x-ray tubes is generally several orders of magnitude higher than a radioisotope source. The beam is unpolarized, polychromatic and fairly directional but diverging. High powered sources are usually stationary due to their active cooling or rotating anodes, but lower powered tubes can be made portable<sup>[9]</sup>.

The last common x-ray source is provided by synchrotrons, ring-shaped particle accelerators. Synchrotrons accelerate electrons around the ring shaped beam path, producing photons at bends used to keep electrons on the circular path. X-rays may also be produced at other points of the beam path using devices known as wigglers and undulators<sup>[4]</sup>. Synchrotrons also produce polychromatic x-ray beams, however these beams are polarized, highly directional, and have extremely high fluence rates.

As such, synchrotron sources tend to be the best for performing x-ray experiments, however there are limited facilities worldwide and they are in high demand.

## 2.4 XRF Spectrometry

X-Ray Fluorescence (XRF) spectrometry is a technique that allows the elemental composition of a sample to be determined, by examining the characteristic x-rays emitted by the sample. Due to the dependence of XRF on the Photoelectric effect, experiments are typically designed to maximize this effect. Thus, the x-ray source energy is often chosen to increase the probability of Photoelectric absorption. If only a single element is being examined, then an x-ray energy slightly above the absorption edge will maximize Photoelectric absorption, and therefore characteristic fluorescence.

In Energy Dispersive X-Ray Fluorescence (EDXRF), the primary x-ray source is typically polychromatic, usually produced from an x-ray tube. Having a wide range of input energies allows for interrogation of multiple elements simultaneously. However, this also leads to increased noise in the form of scattered x-rays. When looking to measure trace elements on the order of single PPM, it is often important to consider the effect that the scattered x-rays will have on the detected signal. If there is a significant amount of scattered x-rays at the same energy as the characteristic x-rays, it can make resolving the fluorescence peak impossible. This usually determines the Minimum Detection Limits (MDLs) of the experimental setup, *i.e.* the minimum concentration of an element present to be detected by the current system.

In XRF experiments, considerations are always made to reduce the amount of scatter detected. There are several types of XRF, each with its own unique characteristics used to excite the sample, and reduce scatter. Mono-energetic XRF techniques are

quite good at rejecting scatter, however they have a harder time exciting a large number of elements. On the other hand, polychromatic techniques, like EDXRF are much better for exciting a wide variety of elements, but have increased scatter<sup>[5,6]</sup>. One purpose of this project was to examine a large set of trace elements found in biological samples, many of which have low atomic numbers, resulting in low fluorescence probabilities. Thus, an XRF technique involving a polychromatic source was chosen.

Recently, focus in EDXRF experiments have shifted to performing EDXRF with polarized x-ray beams. Since x-ray scattering is strongly suppressed in the direction of polarization, by employing a specific geometry, scatter towards the detector can be significantly reduced<sup>[22]</sup>. This technique has been shown to work for both coherent<sup>[4,23,24]</sup> and incoherent<sup>[23-25]</sup> scattering. As a result, using a polarized x-ray beam results in a reduction of the scatter incident on the detector, improving MDLs. It was decided that a PEDXRF setup would be the most suitable method of scatter reduction for this project, while keeping the advantages of having a polychromatic beam and high fluence rates.

## 2.5 Polarized EDXRF Spectrometry

Polarized Energy Dispersive X-Ray Fluorescence (PEDXRF) uses a tri-axial setup with specific geometry to polarize the x-rays incident on the sample, which in turn can be used to reduce the scatter towards the detector. This improvement leads to improved MDLs, and decreased fluence rates at the detector, allowing for higher power x-ray tubes to be used resulting in faster acquisition times. While using a polarized beam reduces the number of scattered photons incident on the detector,

the x-rays fluoresced by the sample are not polarized, and may be emitted in any direction. Hence, using a beam of polarized x-rays to perform EDXRF means that there is no decrease in the number of x-rays fluoresced, only the scatter.

As discussed earlier, for sufficiently low energies, the approximate relationship between the differential cross-section for both types of scatter and the direction of polarization is shown in Equation 2.14.

$$\left(\frac{d\sigma}{d\Omega}\right) \propto \sin^2\Psi \quad (2.14)$$

From this relation it is easy to see that x-rays do not scatter in the direction of their polarization. It is important to note that the scatter follows a  $\sin^2\Psi$  relationship, with the maximum scatter occurring perpendicular to the direction of polarization. Therefore, even within small angles around the direction of polarization, scatter is minimized. Figure 2.7 shows a graphical representation of scatter probability as a function of polar angle.

Another important feature shown in Figure 2.7 is the polarization of the scattered photon. It turns out that the scattered photon polarization will be the projection of the original polarization onto a plane perpendicular to the scattered photon direction<sup>[4,19]</sup>. Using this characteristic, a non-polarized beam can become polarized, using appropriate geometry. Figure 2.8 shows the experimental setup used. This geometry is often referred to as a tri-axial, or Cartesian geometry, but for consistency will be referred to the Polarized Energy Dispersive X-Ray Fluorescence (PEDXRF) setup.

The polarization vectors of the primary beam are shown in Figure 2.8. Since the output of an x-ray tube is non-polarized, it can be represented as a sum of two perpendicular polarization vectors,  $\vec{E}_x$  and  $\vec{E}_z$  in the figure. The primary beam is

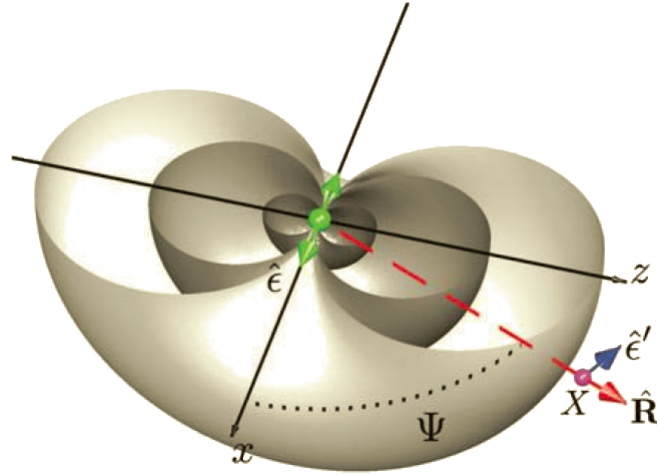


Figure 2.7: A figure showing the probability of polarized x-ray scatter as a function of polar angle. The photon is travelling in the  $z$  direction, with a polarization vector in the  $x$  direction, denoted by  $\hat{e}$ . The probability for scattering in any direction is shown by the grey rings. If the photon scatters by an angle  $90^\circ - \Psi$  in the direction  $\hat{R}$ , then the new polarization vector  $\hat{e}'$  will point in the  $X$  direction.<sup>[4]</sup>

then scattered off of a secondary target, and the sample is placed perpendicular to the original direction. Since the x-rays polarized in the  $\vec{E}_x$  direction cannot be scattered towards the sample, the secondary beam (the beam scattered off the secondary target) must all be polarized in the  $\vec{E}_z$  direction. The secondary beam is used to excite the sample, which either leads to scatter or fluoresced x-rays. The detector is placed in the direction that is mutually perpendicular to both the primary and secondary beams, therefore it receives no scatter from the primary beam, only fluoresced x-rays from the sample.

Clearly, the secondary target is required to polarize the primary x-ray beam, so secondary target material choice is very important. There are three main types of secondary targets used, Barkla scatterers, metallic fluorescers, and Bragg polarizers<sup>[6]</sup>. Barkla scatterers are used to provide the polarized secondary beam, without greatly

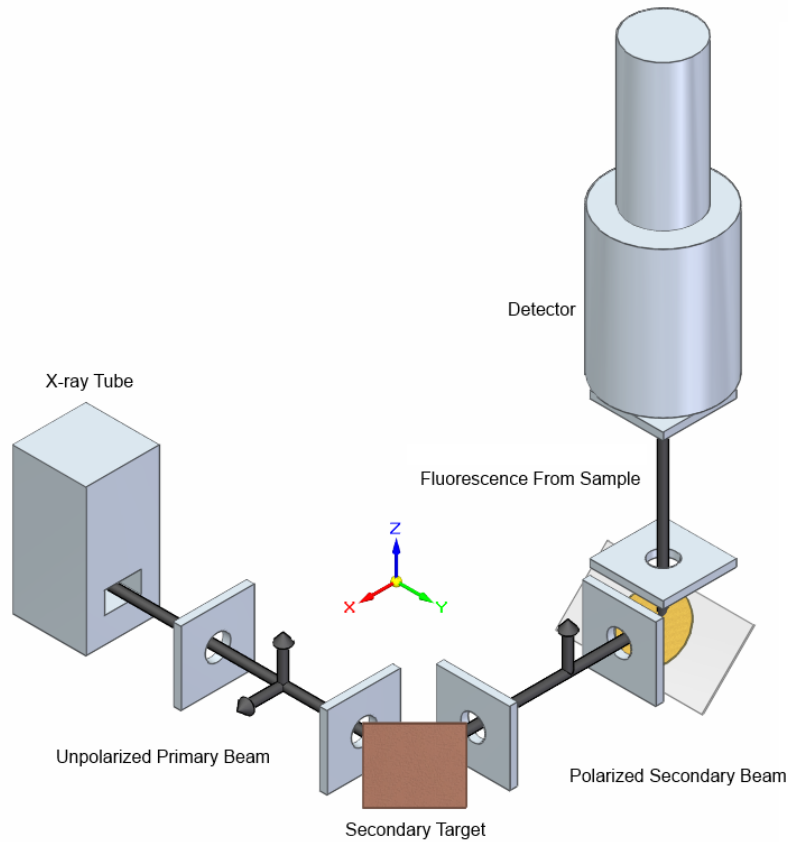


Figure 2.8: The PEDXRF setup, showing the polarization vectors of the primary and secondary x-ray beams.

affecting the beam energy<sup>[6,23,24,26]</sup>. These targets are usually made of low atomic number materials, such as  $Al_2O_3$  or plastics<sup>[6,26]</sup>. While they do provide a polarized secondary beam, they are generally fairly inefficient and rarely used.

Instead, metallic fluorescers and Bragg polarizers are much more commonly used. These two types of secondary targets modify the secondary beam energy, by adding fluorescence or via diffraction respectively. While Bragg polarizers result in a fully polarized beam, the energies they produce make them effective for performing XRF on elements with very low atomic numbers<sup>[6]</sup>. However, for the trace elements found

in biological samples, metallic fluorescers are the most efficient type of secondary target<sup>[6,27]</sup>.

Since the secondary target can be any material, it is frequently chosen to be a material which has a slightly higher x-ray fluorescence energy than binding energy of the element(s) of interest in the sample. This leads to an overall increase in the number of fluoresced x-rays of the sample, since more of the incident x-rays have an energy close to the sample's Photoelectric absorption edge. There is a downside though, since the fluorescence produced by the secondary target is non-polarized, it will be able to scatter towards the detector. This effect is negligible compared to the vastly improved Photoelectric effect probability, which is why it is the most effective secondary target for many trace elements<sup>[6,7,27]</sup>.

In addition to secondary target choice, collimation is also very important in PEDXRF<sup>[18,27]</sup>. If the beam paths are infinitely narrow, then there will be a zero probability of polarized scatter reaching the detector face. In reality, the beam must be allowed to have some width, otherwise the fluence rate incident on the sample becomes vanishingly small. As a result, optimizations between beam width, degree of polarization, and fluence rate must be considered<sup>[18,27]</sup>.

## 2.6 XRD Spectrometry

X-Ray Diffraction (XRD) spectrometry is a technique used to determine the structural components of a material. Using the fact that x-ray photons are electromagnetic waves, they must be able to perform superposition. Interference patterns caused by constructive and destructive interference of x-rays provides information on the structure the x-ray scattered off of.

In XRD the main interaction of interest is coherent scattering<sup>[4]</sup>. As the x-rays traverse the medium, they can either interact with an atom, or continue moving in their original direction. As the photons scatter off of individual atoms, diffraction patterns will emerge based on the spacing of the atoms. As such, highly ordered materials like crystals and powders are ideal candidates for XRD<sup>[4]</sup>.

The simplest type of XRD is known as Bragg diffraction<sup>[4]</sup>. Figure 2.9 shows the theoretical framework for Bragg diffraction. Consider two sets of atoms, separated by an atomic spacing  $d$ , with an x-ray beam incident at an angle  $\theta$ , as shown in Figure 2.9. For constructive interference to occur between the two scattered x-rays, the difference in path length travelled must be some multiple of the wavelength. This leads to the Bragg condition, shown in Equation 2.15<sup>[4]</sup>.

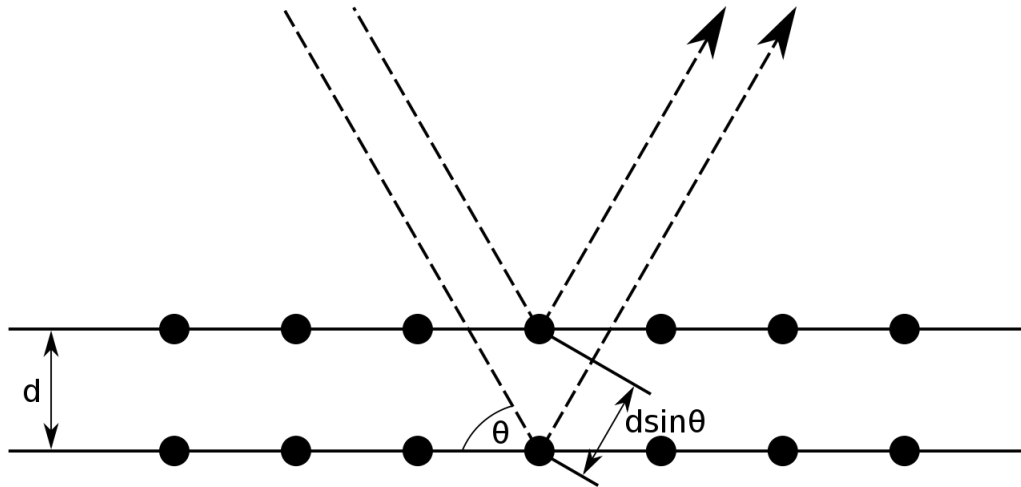


Figure 2.9: A diagram illustrating the Bragg condition. The path length difference between the two photons is  $2d \sin \theta$ .

$$n\lambda = 2d \sin \theta \quad (2.15)$$

The purpose of an XRD experiment is to determine the atomic spacings  $d$  by

looking for constructive interferences. In reality, the atomic spacings  $d$  will not be a single distance in the direction of the original photons, but will be a collection of spacings in three dimensions. In crystal and powder diffraction, the list of  $d$  spacings can be calculated using the Miller indices<sup>[4]</sup>. For less-ordered materials, such as biological samples, distinct atomic spacings are replaced by average spacings, resulting in broader, less distinct diffraction patterns. Regardless, by examining the atomic spacings of a sample, information regarding the structure of that material can be learned.

Two common methods of XRD exist, ADXRD and EDXRD<sup>[4,14,15]</sup>. In ADXRD, a mono-energetic (and therefore single wavelength) x-ray source is used to interrogate the sample. To determine  $d$ , the angle of incidence  $\theta$  must be varied, either through changing the experimental geometry, or using a position sensitive detector. Instead, EDXRD uses a polychromatic source, providing a range of input wavelengths. In this case, only a single angle is required, resulting in a fixed geometry experiment. Since polychromatic sources tend to have higher fluence rates, EDXRD experiments tend to take less time than ADXRD experiments. While both have been used previously on biological samples<sup>[3,14,15]</sup>, an EDXRD setup was decided to simplify geometry, decrease data acquisition time, and make full use of the polychromatic x-ray source.

## 2.7 EDXRD Spectrometry

Figure 2.10 shows an example EDXRD experimental configuration<sup>[28]</sup>. X-ray tubes are used to provide the polychromatic x-ray source, which must be collimated to a straight beam. This beam is incident on the sample, and a single angle must be chosen using a second collimator. The collimator width must be kept fairly small,

in order to preserve the scattering angle. If wide collimators are used,  $\theta$  becomes  $\theta \pm \Delta\theta$ , and referring to Equation 2.15, for a single  $d$  spacing, there will be multiple wavelengths that provide constructive interference. This in essence broadens the diffraction pattern measured. However, if too small a width is chosen, fluence rate can suffer drastically. As such, there is a trade-off between data acquisition time and diffraction peak width. However in samples with low structure, diffraction peaks are already broad, lessening the effect of large collimator width.

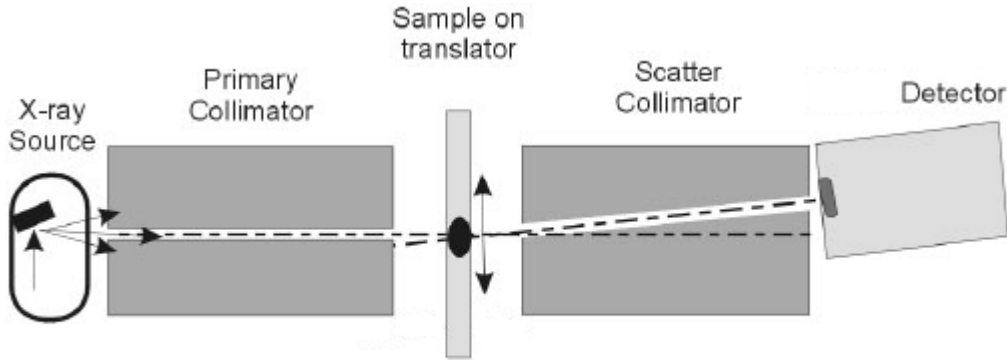


Figure 2.10: An example EDXRD experimental setup. The sample translator allows for different locations on the sample to be measured<sup>[28]</sup>.

In order to compare results of different XRD techniques, the momentum transfer is typically used<sup>[3,4,14,15]</sup>. The momentum transfer  $\chi$  can be calculated as shown in Equation 2.16. Using momentum transfer allows for EDXRD and ADXRD results to be directly compared, since the energy and angular factors are combined into a common term.

$$\chi = \frac{1}{\lambda} \sin\left(\frac{\theta}{2}\right) = \frac{E_{\gamma}}{hc} \sin\left(\frac{\theta}{2}\right) \quad (2.16)$$

It should be noted that EDXRD results must also be corrected for differences in

beam intensity at different energies. While ADXRD results will have a consistent beam intensity, EDXRD results will be inputting a spectrum of energies. Simply dividing the measured results by the beam intensity at each energy provides a good approximate correction for this effect.

# Chapter 3

## Design & Implementation

The process of designing the combined PEDXRF and EDXRD system was iterative. While most design work was done for each technique independently, certain considerations were made in the final designs to combine the two. Mirroring this approach, this chapter focuses on the design of each system independently, followed by a brief discussion on implementing them together.

Both x-ray techniques chosen were energy dispersive, requiring a polychromatic source. This simplified source choice consideration, as x-ray tubes are the most commonly used polychromatic x-ray source. The x-ray tube used for all work was a Varian NDI-160-21, a water cooled tungsten anode x-ray tube with max voltage of  $160kV$  and max current of  $25mA$ .

A common sample holder was also decided upon, which allowed for samples to be run on both systems without modification. Figure 3.1 shows the sample holders designed for these experiments. One side of the sample holder is covered with Ultralene<sup>®</sup> film, a film specifically designed not to interact strongly with x-rays, the sample is placed in the holder, then the other side is covered with the film. The x-rays

were collimated to match the size of the hole in the sample holder, which ensures that x-rays interact with only the sample and not the holder. The holders were 3D printed out of Polylactic Acid (PLA), which unfortunately contained trace amounts of  $TiO_2$  used to provide colouring. As such, it was important to ensure the x-rays did not hit the sample holder, otherwise titanium fluorescence was detected. The small hole at the bottom of sample holder was added to assist in aligning the sample holders, but was ultimately left unused.

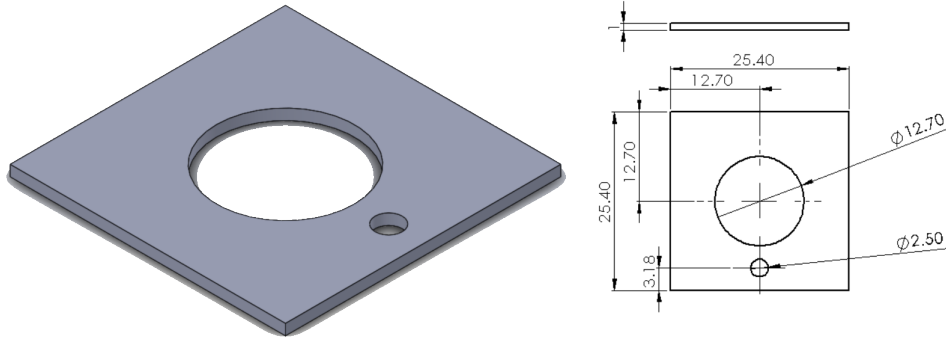


Figure 3.1: The design of the sample holders used in the combined PEDXRF, EDXRD system. All dimensions are in  $mm$ .

### 3.1 PEDXRF Design

Work originally began with the PEDXRF system, which required the most effort to implement due to the strict geometry requirements. The original PEDXRF model is shown in Figure 3.2. This model had no collimators, and relied on large distances between the x-ray tube, secondary target, sample, and detector to provide the required  $90^\circ$  angles. The detector used was a High-Purity Germanium (HPGe) detector from Ortec. The crystal had a diameter  $25mm$ , with a length of  $13mm$ , and an energy

resolution of  $300\text{eV}$  at  $5.898\text{keV}$  ( $^{55}\text{Fe}$  energy).

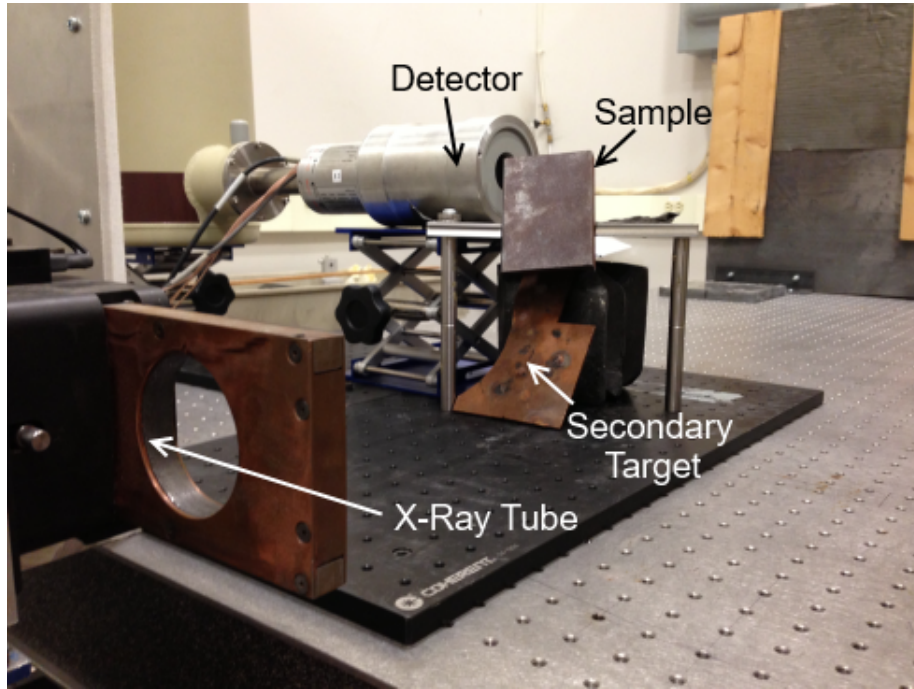


Figure 3.2: The first PEDXRF setup, with main components labelled.

The first model PEDXRF system was used in a proof of concept experiment, determining the effectiveness of the polarized scatter reduction. To examine this effect, the final scatter angle, the angle between the detector and sample, was changed from  $\Psi = 0^\circ - 90^\circ$  in steps of  $22.5^\circ$ . This provided information on the most and least scatter detected, as well as the non-polarized case (which occurs at  $45^\circ$ ). For this test, the secondary target was made of copper, while the sample was steel, which is mostly composed of iron. The results of this experiment are shown in Figure 3.3.

During the experiment, x-ray voltage was set to  $40\text{kV}$ , and tube current was increased to provide roughly the same count rate for all angles, illustrating one advantage of using PEDXRF, the lack of scatter allows for higher powered sources

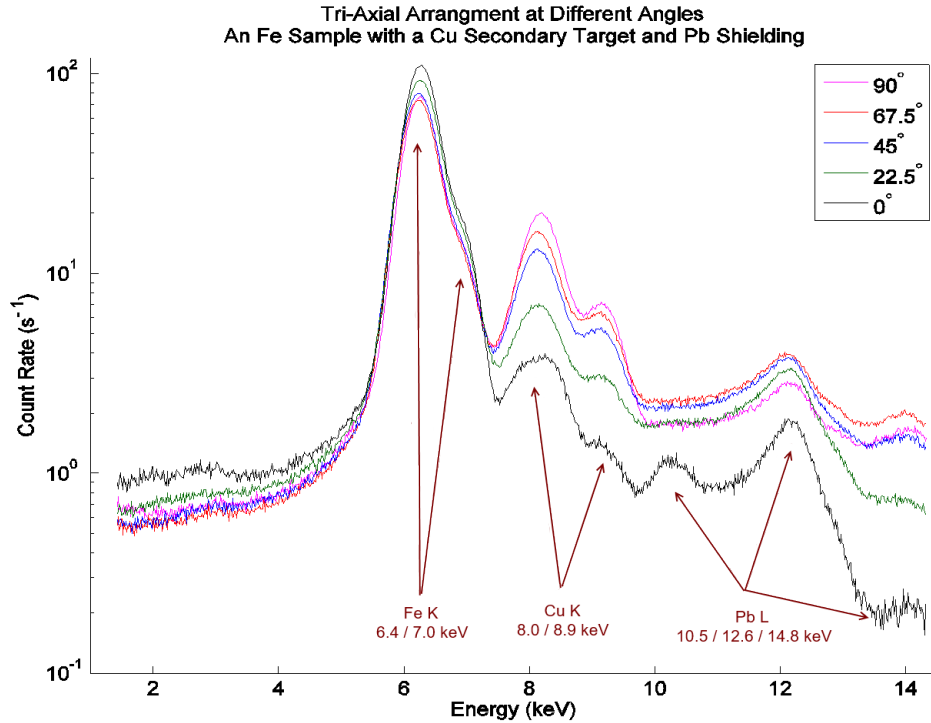


Figure 3.3: Proof of concept experiment, varying  $\Psi$  between the sample and detector. The count rate is shown on a log scale.

without drastically increasing system dead time<sup>[27,29]</sup>. The results of the proof of concept experiment were normalized so that count rate was consistent across all angles. The peaks at  $6.4\text{keV}$  and  $7.0\text{keV}$  correspond to the  $K_{\alpha}$  and  $K_{\beta}$  of iron, respectively, coming from the sample. The copper secondary target provides  $K$  fluorescence peaks at  $8.0\text{keV}$  and  $8.9\text{keV}$ . The peaks at  $10.5\text{keV}$ ,  $12.6\text{keV}$ , and  $14.8\text{keV}$  are lead  $L_{\alpha}$ ,  $L_{\beta}$ , and  $L_{\gamma}$  respectively, caused by lead shielding used during the experiment. The rest of the spectrum consists of scattered photons.

The results in Figure 3.3 clearly show a reduction in scatter at lower angles, while the fluorescence peak rose as a result of higher x-ray tube current. Worth noting is the appearance of Pb  $L_{\alpha}$  in the  $\Psi = 0^{\circ}$  measurement, further illustrating

that high amounts of scatter can overpower weak fluorescence signals. In all other measurements, the lead  $L_\alpha$  peak appears to vanish within the scatter.

Although this model PEDXRF system was functioning as expected, it was quickly realized that while it was capable of measuring fluorescence from a material made almost entirely of iron, it struggled to measure trace elements in samples, due to the lack of collimation and therefore well-defined beam path. Instead, scatter dominated the spectra of samples with trace elements.

The second PEDXRF design is shown in Figure 3.4, which featured several collimators to restrict the x-ray beam geometry. The collimators were chosen to be made from aluminum, which is suitable for attenuating low energy x-rays up to  $\sim 15keV$ . Places that required extra shielding also had pieces of lead followed by aluminum for filtering. Lead provides effective shielding against high energy x-rays, but has  $L$  fluorescence that may interfere with elements of interest. As such, using a combination of lead and aluminum to shield allows for high energy x-rays to be attenuated by the lead, while the aluminum absorbs the lead fluorescence. Two other major improvements in this model were the addition of a secondary target holder, which allowed for secondary targets to be changed easily and accurately, and the angled sample holder, which was capable of holding liquid phantoms and soft tissue samples. At this point, the detector was also switched to a Silicon (Lithium Drifted) (Si(Li)) detector, also from Ortec. This detector had a crystal diameter of  $16mm$ , with a length of  $5mm$ , and an energy resolution of  $220eV$  at  $5.898keV$  ( $^{55}Fe$  energy).

This model proved much more effective at measuring trace elements, due to the improved collimation. However, it was found that even this setup allowed for too much scatter to reach the detector, resulting in poor results when examining elements

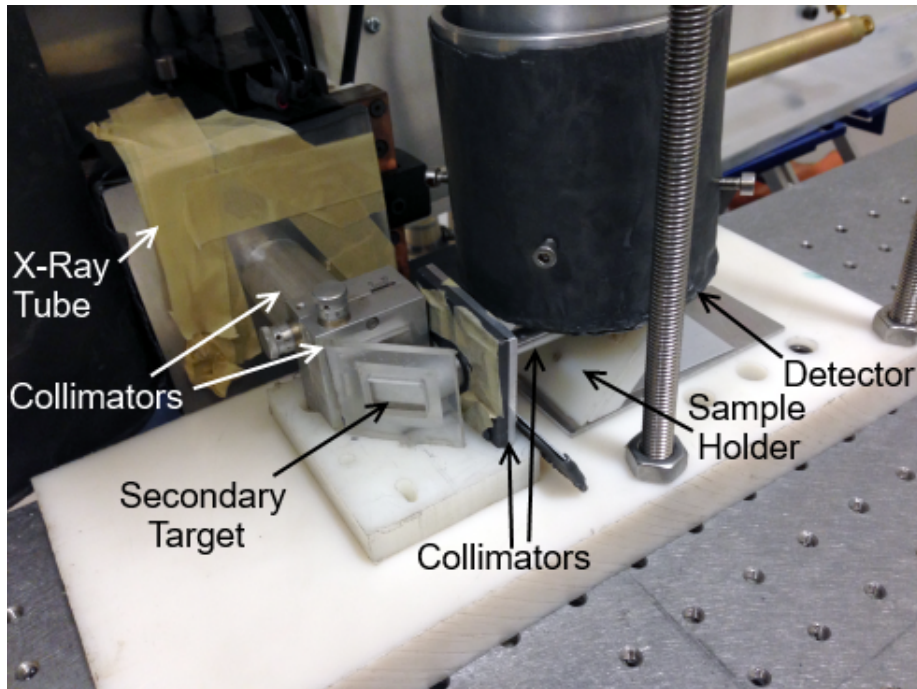


Figure 3.4: The second PEDXRF setup, with main components labelled.

at concentrations as low as  $100\mu\text{g/g}$ . The background (*i.e.* a measurement with no sample) for the second model is shown in Figure 3.5, zoomed in on the  $5 - 11\text{keV}$  region.

From Figure 3.5, it is obvious that there are iron and copper fluorescence peaks present in the background spectrum, as well as lead from shielding. This suggested that the beam was not travelling where it was expected, the aluminium was not filtering a significant amount of lead fluorescence, and that there was iron and copper present along the beam path. Unfortunately, iron and copper are important trace elements to measure in biological samples<sup>[1-3]</sup>, so the system had to be improved to remove these peaks from the background spectrum.

This led to the third design of the PEDXRF system. This design, shown in Figure 3.6, used three pieces of aluminum tubing welded together at right angles,

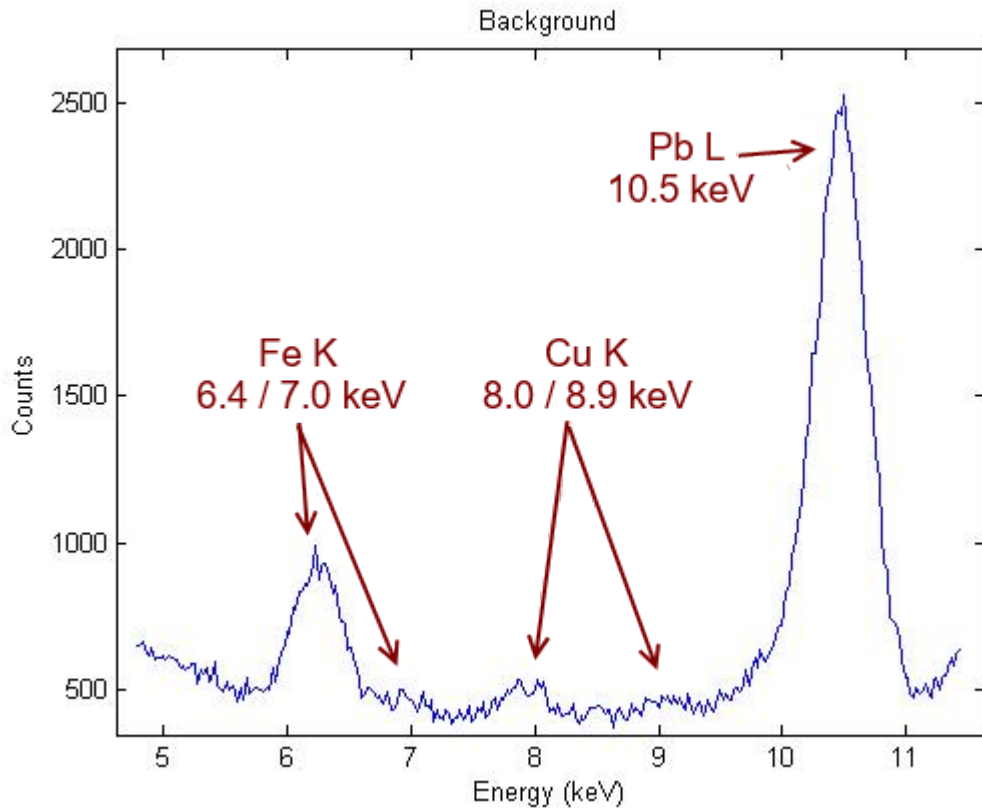


Figure 3.5: A background spectrum collected by the second PEDXRF setup, showing the 5 – 11 keV region. The iron and copper peaks are caused by contamination along the beam path.

to guide the beam path. Because they were welded, the x-rays had to follow the expected beam path, or be attenuated by the aluminum. To eliminate higher energy x-rays, the aluminum tubes were surrounded by lead.

The secondary target and sample holders were placed at  $45^\circ$  to the beam path in specially designed grooves, which helped to improve the accuracy and repeatability of measurements using this setup. This setup was also outfitted with different sized collimators that could be slotted into the aluminum tubes, shown in Figure 3.7. These collimators allowed for customization of the beam width and experimentation with

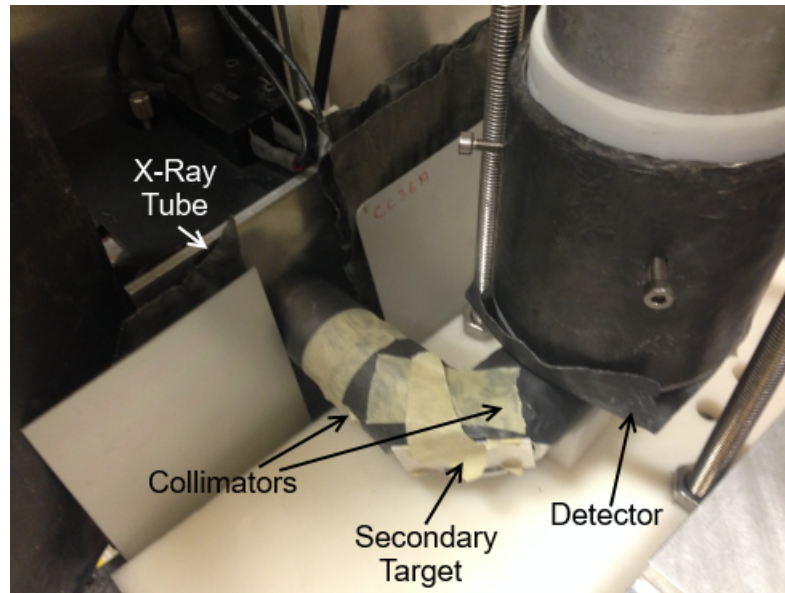


Figure 3.6: The third PEDXRF setup, with main components labelled. The sample holder cannot be seen from this angle, but sits underneath the detector.

various geometries, as discussed in Chapter 4.

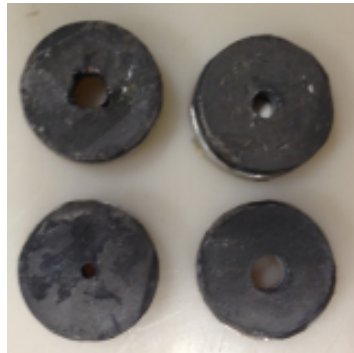


Figure 3.7: The adjustable collimators designed for the third PEDXRF setup. Each collimator size had 3 collimators made, so that one could be placed in each aluminum tube.

This PEDXRF setup worked fairly well, providing useful measurements of iron and zinc in the  $100\mu\text{g}/\text{g}$  range within 30 minutes. An example measurement of an iron phantom is shown in Figure 3.8. The iron  $K$  fluorescence is very clear in this

measurement, but it also shows that the lead fluorescence is still present, as well as a very small copper fluorescence peak. One major concern with this setup was the counting time required to measure  $100\mu\text{g/g}$  phantoms, as this is quite a high value for a trace element. Typical PEDXRF counting times are 10 minutes or less, having a higher sensitivity than this setup<sup>[6]</sup>. It was determined that the large distances between each component of the system (x-ray tube, secondary target, sample, and detector) were causing a significant loss in fluence rate. Unfortunately, due to the large frame of the Si(Li) detector, there was no way to shorten some of these distances. This led to the development of the fourth PEDXRF setup.

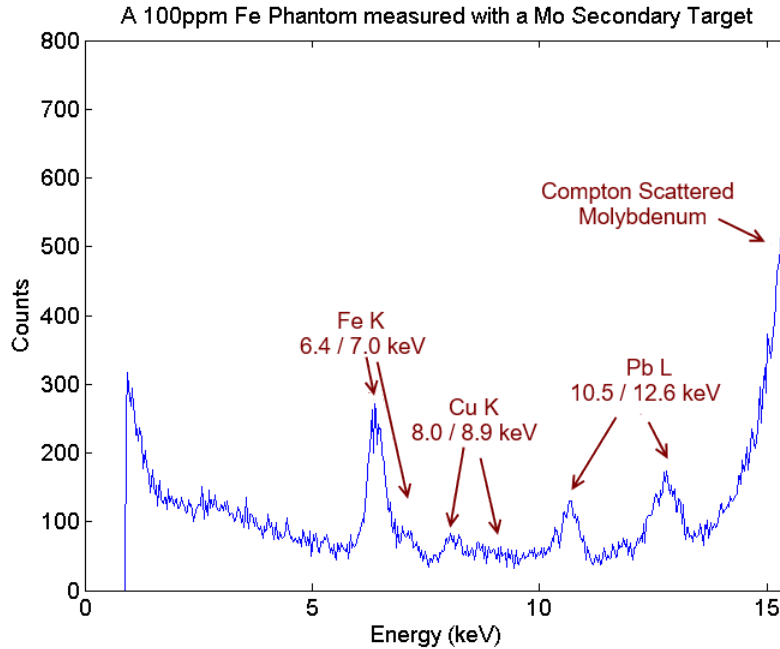


Figure 3.8: A spectrum collected by the third PEDXRF setup, showing the 0 – 15 keV region. This measurement was of a  $100\mu\text{g/g}$  iron phantom, excited using a molybdenum secondary target.

The next PEDXRF setup utilized a Silicon Drift Detector (SDD) instead of a Si(Li) detector, with a crystal area of  $7\text{mm}^2$  and an energy resolution of  $200\text{eV}$  at  $5.898\text{keV}$

( $^{55}\text{Fe}$  energy). These detectors typically have a much smaller frame, allowing them to be placed closer to the sample. Switching to a smaller detector allowed for the entire system size to be reduced, increasing the x-ray fluence rate incident on the detector. Figure 3.9 shows the fourth PEDXRF system designed. Instead of using aluminum tubes, this setup was machined from a solid block of Polyvinyl Chloride (PVC). It was hypothesized that the trace iron and copper peaks measured in previous attempts was caused by impurities in the aluminum, x-rays scattering off of the table, or residue left from the machining process. In order to test this hypothesis, this system was made without the use of aluminum, instead allowing the x-rays to travel freely. Since PVC has a relatively low effective atomic number, it was expected that the x-rays would mostly pass through the plastic instead of interacting, allowing for the setup to work without collimators.

After thorough testing, it was determined that collimators are required for proper functioning of the PEDXRF setup, which is not surprising due to the strict geometrical requirements. However, this time they were fashioned out of only lead, except for the collimator between secondary target and sample, which was made of aluminum surrounded by lead. This turned out to provide significant improvements to the experimental results. Figure 3.10 shows a deionized water phantom measurement run on this setup. This sample was made of Aristar Plus deionized water 87003-652 purchased from VWR<sup>®</sup>, which was injected into an empty sample holder. The sample was measured using a molybdenum secondary target, for 30 minutes, with x-ray tube settings  $50\text{kV}$  and  $25\text{mA}$ .

From Figure 3.10, it can be seen there is still some iron and copper contamination present within the background spectrum, the deionized water used has almost no

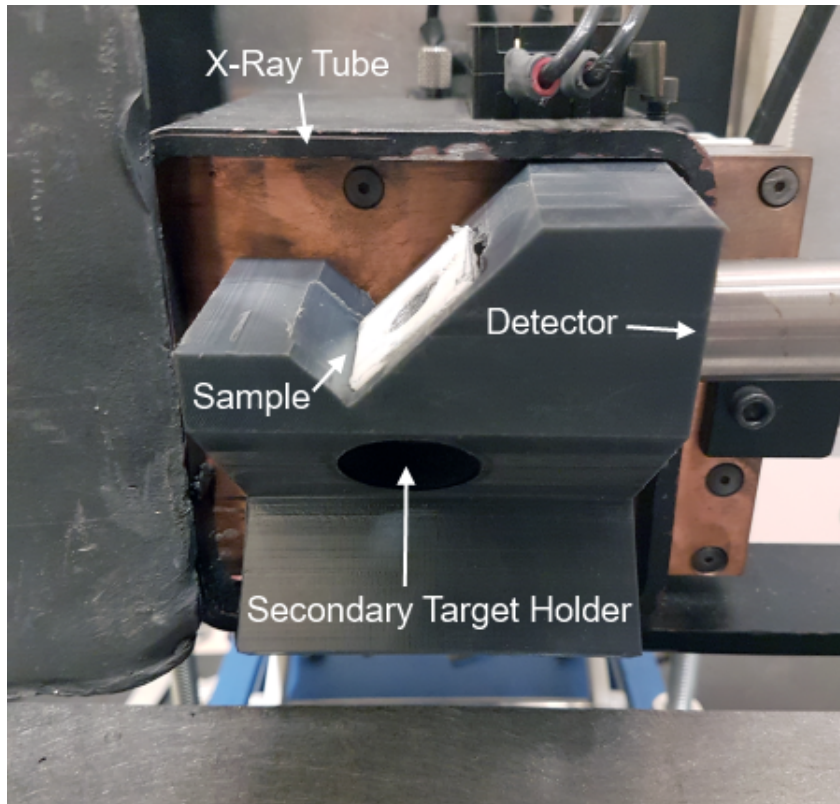


Figure 3.9: The fourth PEDXRF setup, with main components labelled. This design was made from a solid block of PVC.

iron and copper in it. However, when compared to previous results, this was still a great improvement over previously measured background spectra. It should be noted that the lead  $L$  lines are much larger now due to the lack of aluminum filtering. Also seen in this spectrum is an argon peak ( $3.0keV$ ), which comes from the air, a chlorine peak ( $2.6keV$ ) from the PVC and sample, a titanium peak ( $4.5keV$ ) which comes from the sample holder. The nickel ( $7.5keV$ ) and zinc ( $8.7keV$ ) are known contaminants in this deionized water. While not perfect, this setup was capable of finishing the optimization work discussed in Chapter 4.

The final PEDXRF setup was designed taking into account all previous results,

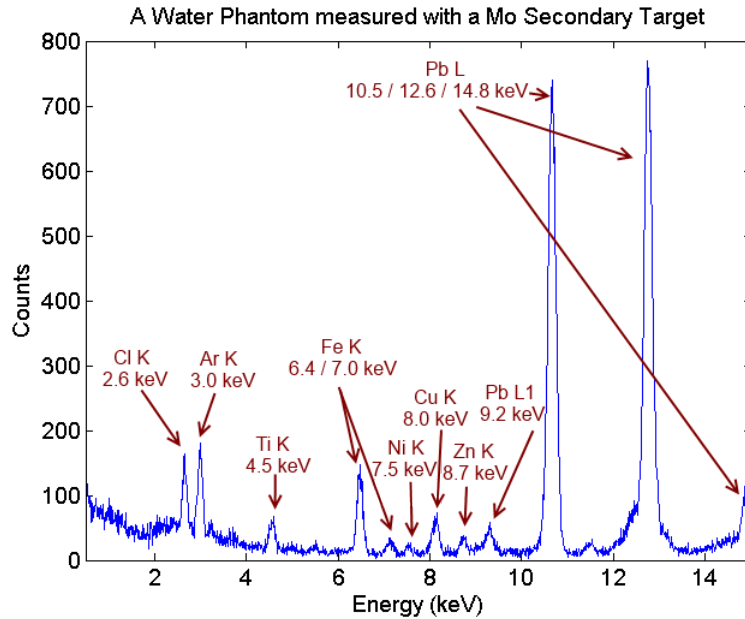


Figure 3.10: A spectrum collected by the fourth PEDXRF setup, showing the 0 – 15 keV region. This measurement was of deionized water phantom, excited using a molybdenum secondary target.

providing the best setup available. Continuing with the solid plastic block approach, the final model was 3D printed out of PLA. Switching to a 3D printed model greatly reduced manufacturing time, produced high quality results, and removed all chlorine and machining contamination from the final product. Figure 3.11 shows the finished PEDXRF design, while Figure 3.12 shows the setup disassembled, showing the collimators, secondary target holders, and sample holders.

## 3.2 EDXRD Design

The EDXRD system had been used in previous work designed to perform XRD on cancerous breast tissue<sup>[28]</sup>, so much of the design process was completed previously. Figure 3.13 shows the design of main EDXRD angle block. This angle block was

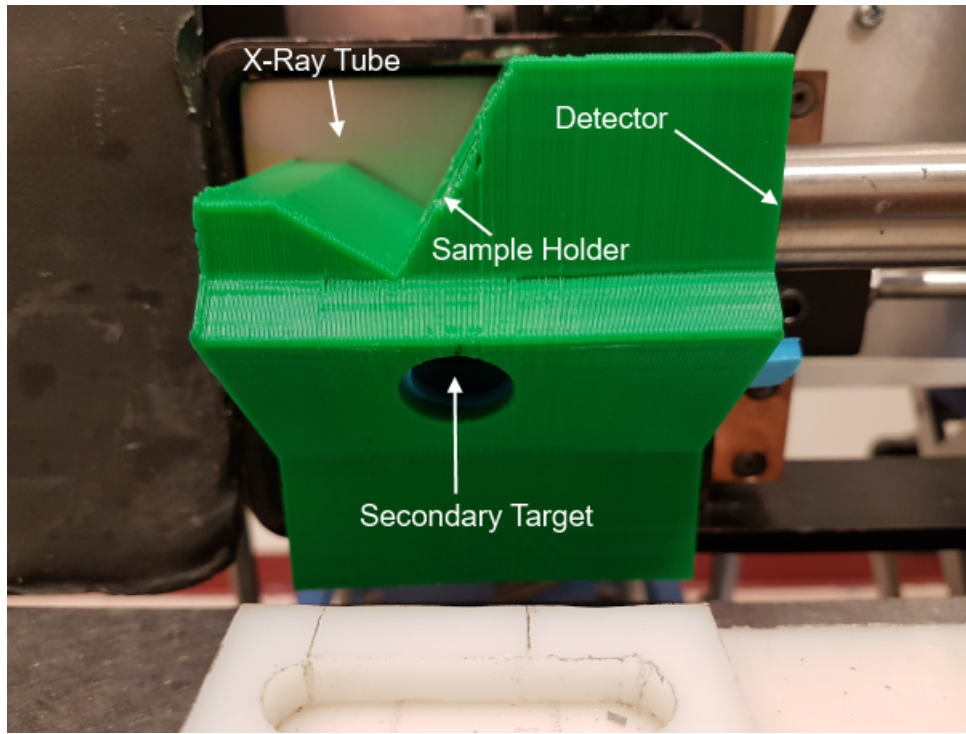


Figure 3.11: The final PEDXRF setup, with main components labelled. This design was 3D printed out of PLA, and contained grooves for the sample holder and secondary target holder to be firmly placed.

designed to facilitate a number of different scattering angles, which may be necessary to achieve optimal results. The holes at the back end of the block are used to attach lead shields, which allow for measurement of a single angle at a time.

Unlike the setup shown in Figure 2.10, the primary collimator was made significantly shorter. It was determined that as long as the primary collimator was a narrow slit collimator, then the EDXRD system functioned properly. Thus, the slit collimator shown in Figure 3.14 was chosen, and fixed to the optics table. The collimator was placed such that the back was  $35.5\text{mm}$  from the EDXRD angle block, placing the middle of a  $1\text{mm}$  thick sample in the focal spot of all angles. As such, the samples are held in contact with the slit collimator via a sample holder. The slit collimator

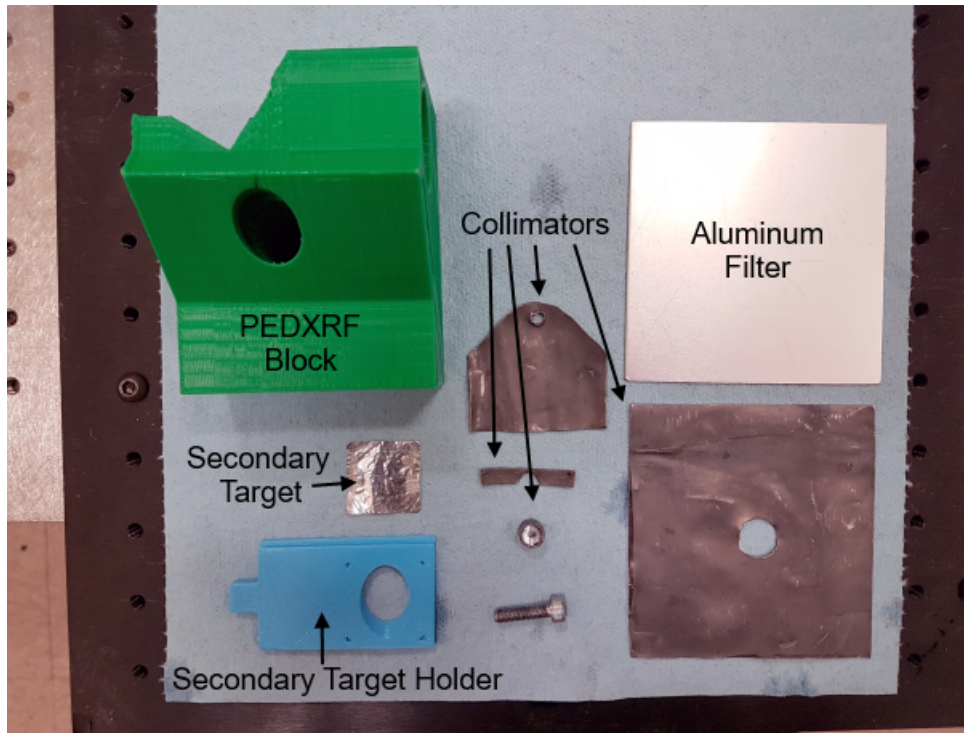


Figure 3.12: The disassembled components of the final PEDXRF system, with labels.

height and width ( $10\text{mm}$  and  $1\text{mm}$  respectively) were set to match the height and width of the slits in the EDXRD angle block. After testing, it was determined that making the primary collimator narrower does not significantly improve results, but drastically reduces fluence rate at the detector. This can be seen easily by examining Figure 3.15, which shows a calcium carbonate sample measured using the EDXRD block, with a diffraction angle of  $6^\circ$ , and x-ray tube settings of  $70\text{kV}$  and  $15\text{mA}$ .

Figure 3.16 is a picture of the entire EDXRD setup, showing the collimator, sample holder, angle block, and detector. The detector used is an HPGe detector from Ortec, outfitted with a slit collimator matching the slit width of the EDXRD angle block. This detector had a crystal diameter of  $25\text{mm}$ , a crystal length of  $13\text{mm}$  and an energy resolution of  $300\text{eV}$  at  $5.898\text{keV}$  ( $^{55}\text{Fe}$  energy).



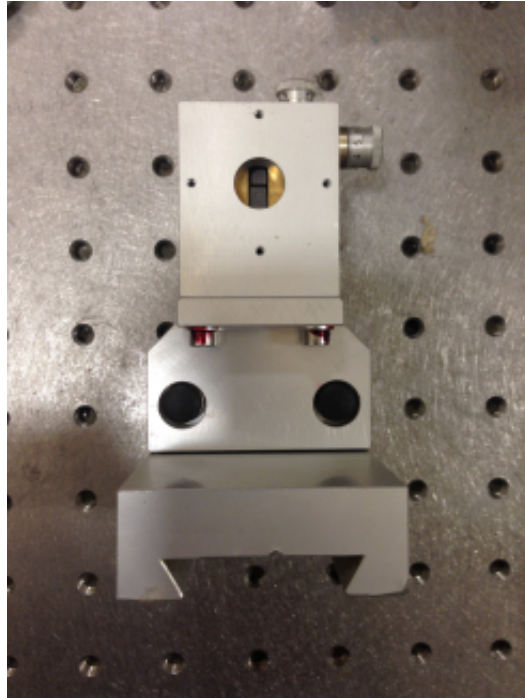


Figure 3.14: The slit collimator used for the EDXRD setup. This collimator has variable width and height, allowing for increased customization.

of the PEDXRF system will not interfere with the EDXRD setup. Thus, if the secondary target is removed from the PEDXRF setup, the x-rays travel through the primary PEDXRF collimator until they reach with EDXRD slit collimator. Since the PEDXRF equipment is much smaller and requires a higher fluence rate than the EDXRD setup, placing it first is the logical choice.

Each setup uses a different radiation detector, so there was no concern with moving the detectors. The PEDXRF requires the SDD to provide minimal geometry as well as a high efficiency at low energies. In contrast, the EDXRD setup uses the full range of the x-ray tube, often requiring x-rays energies up to  $120\text{keV}$ . In this case, an HPGc detector is the most suitable at measuring these higher energy x-rays. It was noted that using a  $2\text{mm}$  aluminum filter on the x-ray output provided better EDXRD

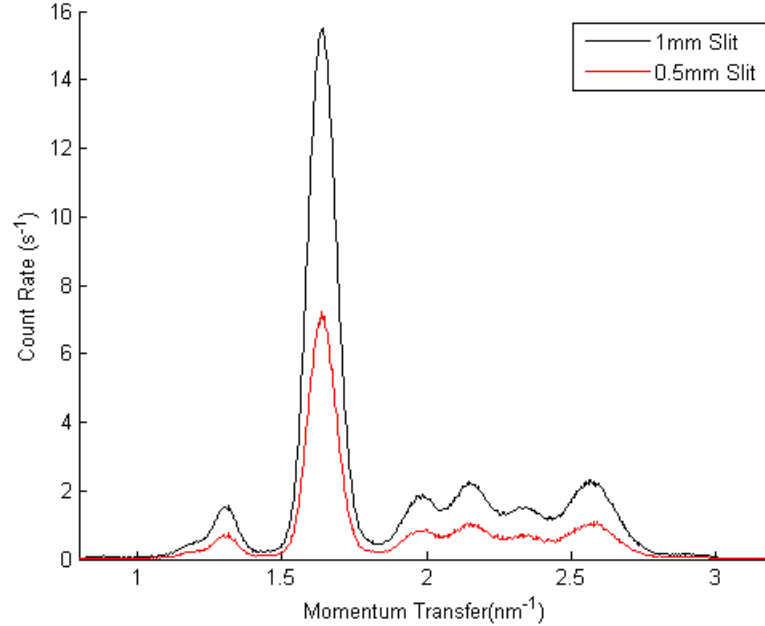


Figure 3.15: The diffraction pattern from a calcium carbonate sample measured with two different slit collimator widths. The smaller slit collimator does not produce better results, but instead decreases fluence rate at the detector.

results, by removing the tungsten  $L$  lines from the spectrum which only served to increase the detector dead time. It was found that this aluminum filtering did not significantly reduce the PEDXRF results, apart from reducing the fluence rate, leaving only higher energy x-rays. However, in the PEDXRF setup, the primary beam energy can be altered using the secondary target to provide an optimal excitation energy. It was decided that the improvement to the EDXRD results outweighed the losses in fluence rate experienced by the PEDXRF setup, and the aluminum filter was applied directly to the x-ray tube output, before the PEDXRF system.

Since both setups use samples in the same sample holder, samples can be transferred from one system to the other very quickly. Additionally, the secondary target

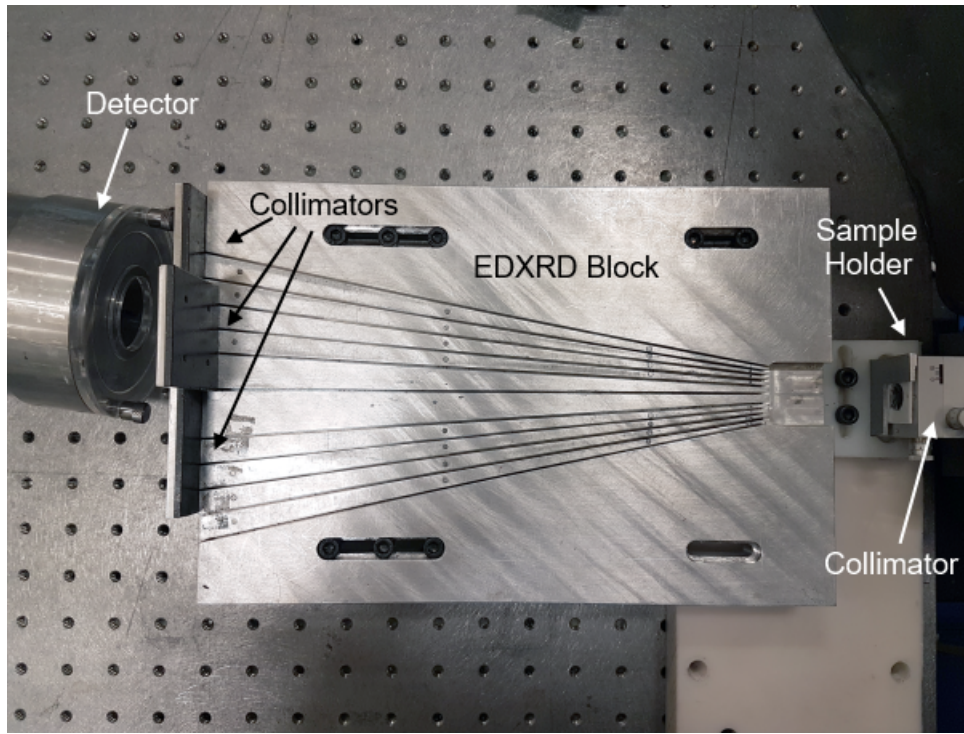


Figure 3.16: The entire EDXRD system, showing the detector, collimators, angle block, and sample holder. All components are fixed to the optics table to ensure proper alignment.

holders can be removed easily, and the x-ray tube potential can be adjusted to optimal settings in approximately one minute. Going from one experiment to the other does not require moving any additional components, or any other work. Altogether, switching between the two setups, requires roughly two minutes, proving the simplicity and usefulness of this combined system.

# Chapter 4

## Optimization

In order to provide the best results, both the PEDXRF and EDXRD systems were optimized for biological samples. For the PEDXRF system, this consisted of a study that focused on optimizing the secondary target, geometry, and exposure parameters. For the EDXRD system, proper x-ray energies and diffraction angles had to be selected to provide the best results. All the optimizations presented were included in the final designs of each system discussed in Chapter 3.

### 4.1 PEDXRF Optimization

#### 4.1.1 Secondary Target Model

Optimizing the PEDXRF system was a significant project, since there were several parameters to optimize. The process was started by first examining the secondary target, selecting which targets were useful, and determining if there were properties of the targets that could be optimized.

Since the secondary target is a component unique to PEDXRF experiments, other experimental setups were examined to determine the best secondary target choice. Each secondary target type has its own benefits, and there have been previous studies to determine which is best for each element to be analyzed<sup>[6]</sup>. Table 4.1 shows a summary of which secondary target is best for each element. Since most elements of interest in biological samples are transition metals, specifically elements from potassium to strontium, it was decided to work with metallic fluorescers as the only type of secondary target.

Table 4.1: A non-exhaustive list of commonly used secondary targets and measurable elements for each<sup>[6]</sup>.

<b>Type</b>	<b>Secondary Target</b>	<b>Measurable Elements</b>
Bragg Polarizer	HOPG	Na-Cl
Metallic Fluorescer	Co	K-Mn, Sm
	Mo	Fe-Y, Hf, Ta, W, Hg, Tl, Pb, Bi, Th, U
Barkla Scatterer	$Al_2O_3$	Zr, Nb, Mo, Ag, Cd, In, Sn, Sb, Te, I, Cs, Ba, La, Ce, Pr, Nd

Now that the secondary targets were narrowed down to a single type, further optimizations could be performed. The main benefit of using a metallic fluorescer as a secondary target comes from the ability to change the energy spectrum of the x-ray beam incident on the sample. The closer the incident x-ray energy is to the Photoelectric absorption edge of the analyte(s), the higher the probability of undergoing the Photoelectric effect, thus increasing fluorescence probability. Even though the fluorescence from a metallic fluorescer will be non-polarized, and thus able to scatter towards the detector, this detriment is outweighed by the increase in sample fluorescence.

When examining multiple elements, the metallic fluorescer must have fluorescence at a higher energy than the absorption edge of all the measured elements. As such, a given metallic fluorescer will be able to excite all elements below it on the periodic table (when looking for  $K$  fluorescence), but will provide the best response for the elements closest to it. Looking at the elements of interest in biological samples, it is possible to excite them all with a molybdenum secondary target. However, for the elements with lower atomic numbers, which are harder to detect due to their lower fluorescence energies and emission probability (refer to Equation 2.10), it is preferable to switch to a secondary target closer on the periodic table. As a result, multiple secondary targets were chosen for this system, to provide highly efficient measurements for all elements of interest. A molybdenum target was chosen due to its ability to measure all elements of interest, while zinc and copper foils were chosen to improve sensitivity when measuring the lower atomic number elements.

Continuing to focus on the secondary target, it was hypothesized that the thickness of the secondary target should be controlled to provide optimal results. Making the secondary target thicker will increase the amount of target fluorescence and scatter produced, but eventually, the target will be too thick for its fluorescence photons to escape, due to self-absorption. At this thickness, no additional fluorescence is being emitted from the target but the scatter may continue to increase. This is due to the fact that the fluorescence is produced at a specific characteristic energy, which must be lower than that of the incident photon. This makes the self-absorption of fluorescence photons more likely to occur than absorption of the scattered photons, which tend to have a higher energy. If the thickness is increased further, eventually the scatter response of the material will reach a maximum, again due to self-absorption. At this

point, the material is said to act ‘infinitely thick’ because increasing its thickness further will have no effect on the fluorescence yield. For the rest of the thesis, any mention of ‘infinite thickness’ will refer to the distance at which no more fluorescence or scatter can come from a secondary target. Since the overall goal of PEDXRF is to minimize the scatter reaching the detector, there must be an optimal secondary target thickness, which maximizes the fluorescence yield to scattered photon fluence ratio.

In order to quantify the effect that secondary target thickness has on the fluorescence yield and scattered fluence, a simplified theoretical model was designed. It was assumed that the primary beam was a narrow pencil beam, incident on the secondary target at  $45^\circ$ , and that both the scattered photons and the fluorescence photons were emitted  $90^\circ$  relative to the direction of the incident beam. Choosing only one angle of interaction allowed for exact expressions to be written, and this geometry, shown in Figure 4.1, makes it so that the photons have to travel the same distance through the material while entering and leaving, simplifying the mathematical expressions.

For a mono-energetic x-ray beam with incoming energy  $E_i$ , the probability of fluorescence being produced at a distance of  $x$  to  $x + dx$  into the material is given by:

$$P_{prod} = \omega_k \mu_{PE}(E_i) e^{-\mu_{tot}(E_i)x} dx \quad (4.1)$$

and the probability of that characteristic fluorescence x-ray, with energy  $E_f$ , escaping the material is:

$$P_{escape} = e^{-\mu_{tot}(E_f)x} \quad (4.2)$$

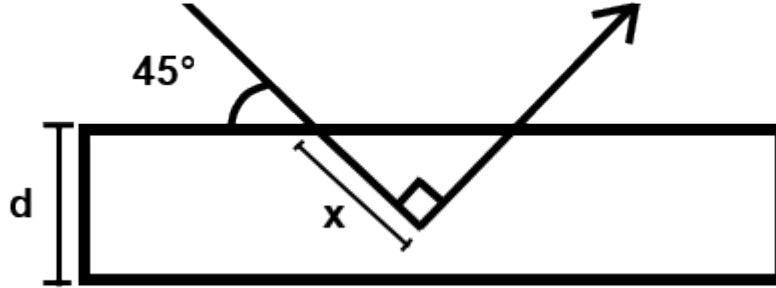


Figure 4.1: The simplified geometry used to model the effect of secondary target thickness on fluorescence and scatter fluence. The x-rays are incident on a secondary target of thickness  $d$ , at a  $45^\circ$  angle, and interact at a depth  $x$ . The outgoing photons are leaving at an angle  $90^\circ$  relative to the incident angle, making the outgoing beam path length  $x$  as well.

Combining Equation 4.1 and Equation 4.2, the total probability of fluorescence production from a secondary target of thickness  $d$  is given by Equation 4.3.

$$\begin{aligned}
 P_{fluo} &= \int dx P_{prod} P_{escape} \\
 &= \int_0^{\sqrt{2}d} dx \omega_k \mu_{PE}(E_i) e^{-(\mu_{tot}(E_i) + \mu_{tot}(E_f))x} \\
 &= \frac{\omega_k \mu_{PE}(E_i) \left(1 - e^{-(\mu_{tot}(E_i) + \mu_{tot}(E_f))\sqrt{2}d}\right)}{\mu_{tot}(E_i) + \mu_{tot}(E_f)}
 \end{aligned} \tag{4.3}$$

Where:

$\mu_{PE}$  is the Photoelectric absorption attenuation coefficient

$\mu_{tot}$  is the total interaction attenuation coefficient

Similarly, the probability that an incoming x-ray will scatter between the distance

$x$  and  $x + dx$  in the material is given by:

$$P_{scx} = \mu_{sc}(E_i)e^{-\mu_{tot}(E_i)x}dx \quad (4.4)$$

and the probability that the x-ray, now at energy  $E_{sc}$  will escape from there is given by:

$$P_{survive} = e^{-\mu_{tot}(E_{sc})x} \quad (4.5)$$

Again, Equation 4.4 and Equation 4.5 can be combined to provide the probability of an incident photon scattering off a secondary target of thickness  $d$ , shown in Equation 4.6.

$$\begin{aligned} P_{sc} &= \int dx P_{scx}P_{survive} \\ &= \int_0^{\sqrt{2}d} dx \mu_{sc}(E_i)e^{-(\mu_{tot}(E_i)+\mu_{tot}(E_{sc}))x} \\ &= \frac{\mu_{sc}(E_i) \left(1 - e^{-(\mu_{tot}(E_i)+\mu_{tot}(E_{sc}))\sqrt{2}d}\right)}{\mu_{tot}(E_i) + \mu_{tot}(E_{sc})} \end{aligned} \quad (4.6)$$

Where:

$\mu_{sc}$  is the scatter attenuation coefficient, either Compton or coherent

$E_{sc}$  is the scattered photon energy

It should be noted that the probabilities for coherent and Compton scattering must be calculated separately, as the energy,  $E_{sc}$ , is different for each case. For coherent scatter,  $E_{sc}$  is the same as  $E_i$ , whereas for Compton scatter,  $E_{sc}$  is the energy of the

photon after interaction (see Equation 2.5), with the scatter angle chosen to be  $90^\circ$ , as shown in Figure 4.1.

Equation 4.3 and Equation 4.6, which are valid for a mono-energetic x-ray beam, can be easily extended to include an entire x-ray tube spectrum. The x-ray tube output spectrum must first be determined and put into energy bins, and the fluorescence and scatter probabilities must be calculated at each of those energies. Then, multiplying the probability by the number of photons in each bin will give the overall likelihood of the interaction occurring. If normalized tube output is used, the probability of the interaction occurring is calculated per photon being emitted by the x-ray tube. Additionally, the above formulas do not include any angular distributions of the scattering functions, for simplicity. However, assuming the geometry is held constant, any quantitative results made using this model must be corrected by an appropriate geometric scaling factor.

Using the model, the fluorescence and scatter probabilities for several secondary targets were calculated. The software program Report78 Spectrum Processor<sup>[30]</sup> was used to determine the expected x-ray tube output at different voltage settings, corresponding to the x-ray tube used for the combined PEDXRF and EDXRD setup. Report78 is a software package that produces histograms of x-ray intensities at  $0.5keV$  energy intervals, based on x-ray tube anode material, angle, and voltage setting, using lookup tables. The voltages chosen ranged from  $30kV$  to  $150kV$  in  $5kV$  steps.  $30kV$  is the lowest voltage the Varian NDI-160-21 will allow, while  $150kV$  is the highest voltage Report78 will provide output data for. The NIST XCOM database<sup>[17]</sup> was used to determine the attenuation coefficients required for each secondary target material at all energies corresponding to the Report78 output.

The model was first used to examine a molybdenum secondary target, due to its high popularity as a secondary target for PEDXRF systems. The fluorescence response of the molybdenum target is shown in Figure 4.2. As expected, the fluorescence response increases with increased thickness up to the escape depth of the fluorescence x-rays, after which, there is no increase in yield. It should be noted the x-ray tube potential also affects the fluorescence response on a per photon basis, as higher tube potentials will have an average potential closer to the  $K$  edge of molybdenum (due to the  $L$  lines of tungsten). As a result, to maximize fluorescence production, the highest x-ray tube potential should be selected.

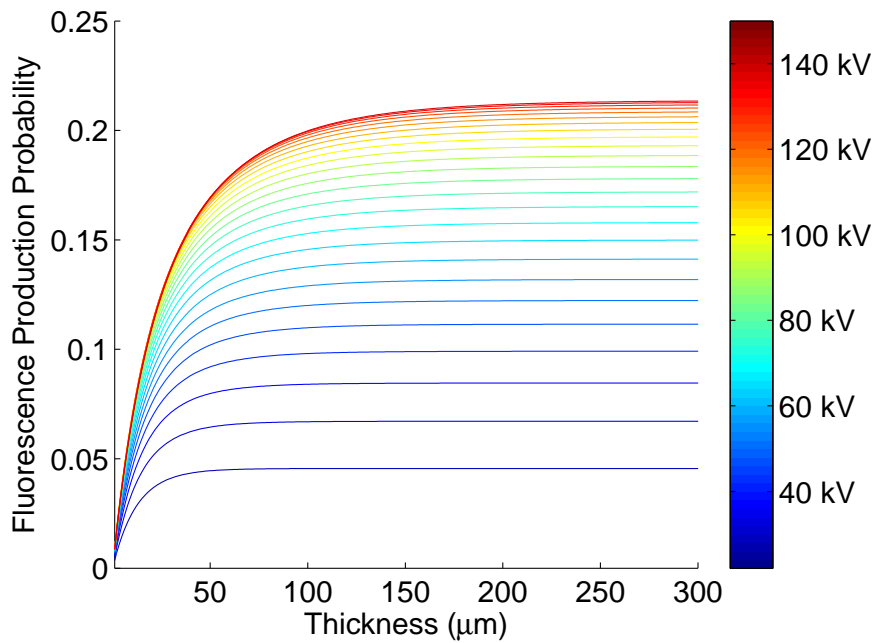


Figure 4.2: The predicted fluorescence response from a molybdenum secondary target as a function of target thickness. The colours represent various x-ray tube potentials.

Figure 4.3 shows the scatter produced from a molybdenum secondary target at various thicknesses and x-ray tube potentials. Once again, the model behaves as

expected, with the scatter produced increasing with increasing thickness, up to some maximum value. In this case, the maximum thickness depends strongly on the chosen potential, as higher energy x-rays are more penetrating, allowing the scatter to occur, and escape, from deeper within the target.

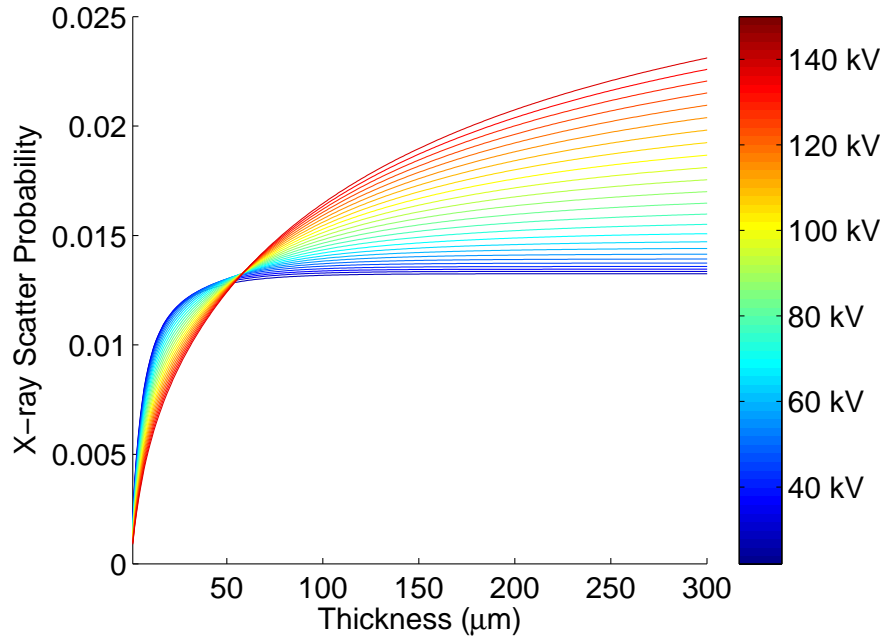


Figure 4.3: The predicted scatter produced from a molybdenum secondary target as a function of target thickness. The colours represent various x-ray tube potentials.

In order to quantify an optimal thickness of secondary target, the fluorescence to scatter ratio should be examined. While this value may not correspond directly into improved MDLs for a PEDXRF setup, it should provide an approximate thickness at which the secondary target may be most useful. Figure 4.4 shows the fluorescence to scatter ratio for a molybdenum secondary target, illustrating that there exists a thickness where this ratio is a maximum. This thickness occurs at approximately  $35\mu m$ , which represents a very thin secondary target. Another interesting feature of

Figure 4.4 is that there is an optimal x-ray tube potential, in this case  $150\text{kV}$ , and there is an ‘infinite thickness’ for the secondary target, at which point any additional thickness does not alter its response.

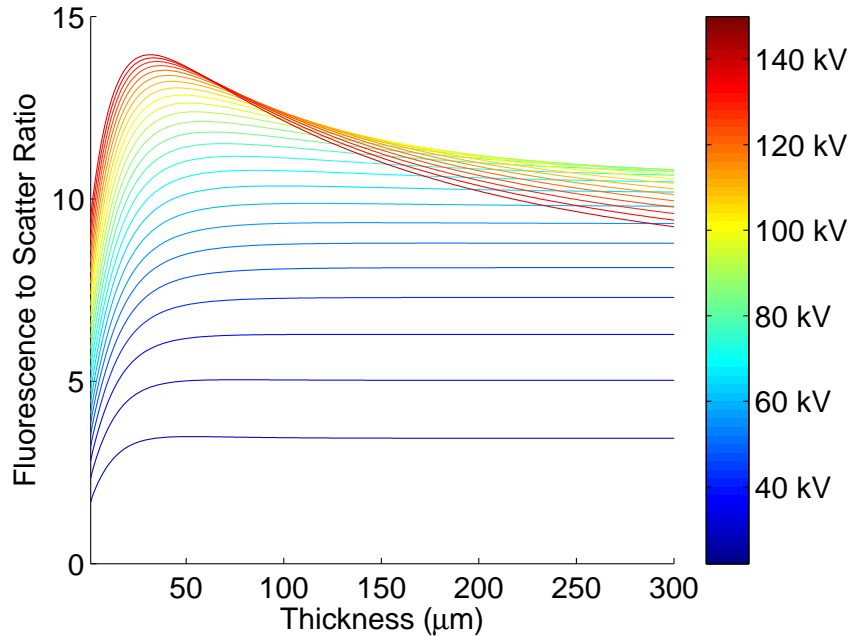


Figure 4.4: The predicted fluorescence to scatter ratio produced from a molybdenum secondary target as a function of target thickness. The colours represent various x-ray tube potentials.

To verify how the model’s predictions vary with atomic number, two other secondary target candidates were modelled, copper and tin. Copper is a common metallic secondary target<sup>[31–33]</sup>, while tin was chosen to see if the theory was valid at higher atomic numbers. Figure 4.5 shows the modelled fluorescence to scatter ratio for the copper and tin secondary targets. Once again, there exists an optimal thickness and x-ray tube potential for each of these targets, although that thickness and potential varies for each target. As seen with the molybdenum secondary target, the materials also exhibit an ‘infinite thickness’ point, which can occur at thicknesses as low as few

hundred microns. This means that unless a very thin secondary target was chosen purposefully, most current PEDXRF designs likely use ‘infinitely thick’ secondary targets.

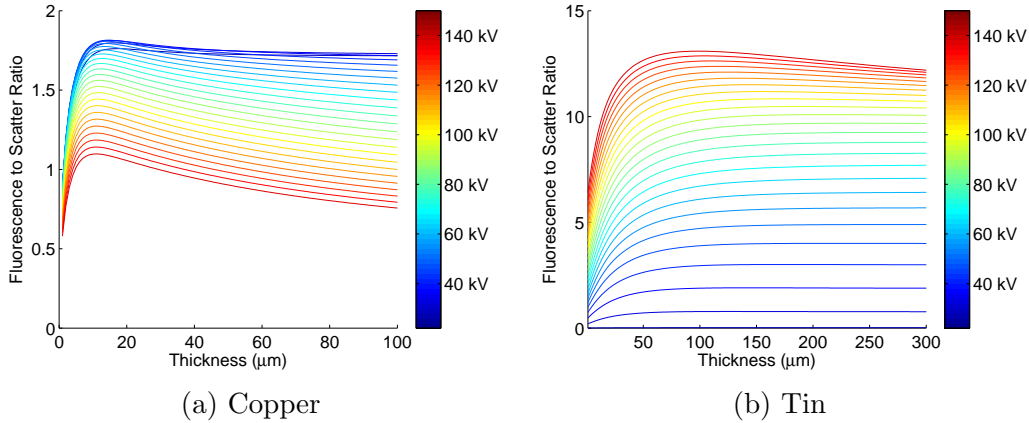


Figure 4.5: The predicted fluorescence to scatter ratios produced from copper and tin secondary targets as a function of target thickness. The colours represent various x-ray tube potentials.

This revelation merited further research, so in order to test the accuracy of the model, a Monte Carlo (MC) simulation and an experiment were performed, matching the model criteria. The GEANT4 MC code was chosen because of its custom physics libraries that allow for low energy x-rays to be simulated precisely<sup>[19,34]</sup>. Using the *LowEMLivermorePhysics* library allowed for the tracking of low energy x-rays that are very likely to scatter or be absorbed. This physics library also handles Doppler broadening and polarization effects of low energy x-rays. The simulations were used to verify that the assumptions made in the theory had only a minor effect on the overall result. In order to compare the simulation to the experimental results, the physical characteristics of the detector used were also simulated.

### 4.1.2 Secondary Target Simulations & Experiment

In order to verify the results found using the secondary target thickness model, an experiment and MC simulation were run in tandem. The experimental configuration was set to closely resemble Figure 4.1, but allowing for a realistic beam width, to test whether the assumptions made in the theoretical model (incident line beam, single defined scatter angle) would affect the outcomes in a real world situation.

Metal targets of various thicknesses were purchased to experimentally determine the optimal thickness. The metal targets ranged from the thinnest easily obtainable thickness of  $1/1000^{th}$  of an inch ( $25.4\mu m$ ) to  $6/1000^{ths}$  of an inch ( $152.4\mu m$ ), which is approximately the point at which the chosen targets start to act infinitely thick. For the copper and tin targets, the thicknesses increased in steps of  $1/2000^{th}$  of an inch ( $12.7\mu m$ ), whereas the molybdenum targets increased in steps of  $1/1000^{th}$  of an inch ( $25.4\mu m$ ). For the GEANT4 simulation, all secondary targets were modelled starting at  $25\mu m$  thick, increasing in steps of  $12.5\mu m$ , up to  $150\mu m$ .

An Ortec HPGe detector ( $13mm$  crystal thickness,  $10cm^2$  active area), with an energy resolution of  $360eV$  at  $5.9keV$  ( $^{55}Fe$  energy), was used to detect the x-rays coming from the secondary targets. For each metal thickness and tube voltage setting, three separate 240s counts were performed. The current was chosen to be  $0.3mA$ , which provided a dead time of 20% for the thickest targets at the highest voltage setting. All other dead times were lower than this value, the lowest being 2% at the lowest voltage setting. The output from the detector was fed to an Ortec 672 spectroscopy amplifier with a  $6\mu s$  shaping time, then to an Ortec 921E multi-channel buffer, and lastly to MAESTRO for spectrum collection. Figure 4.6 shows a block diagram of the signal processing configuration. The spectra were recorded and the

amount of target fluorescence produced was determined using the area under the characteristic x-ray peaks. The amount of scatter produced was set to be everything else in the obtained spectrum; the background radiation count rate for the setup was approximately  $20cps$ , which was significantly lower than the scatter obtained in each spectrum, making this a reasonable assumption.

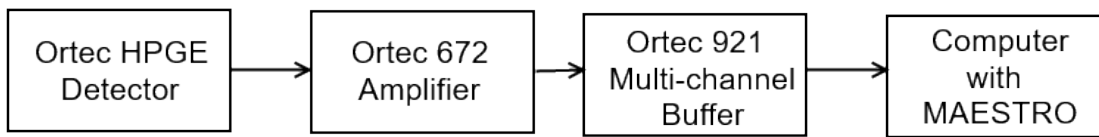


Figure 4.6: The signal processing configuration used in the secondary target thickness experiment.

The x-ray source was collimated down to a spot on the secondary target of  $10mm$  diameter, much smaller than the  $25.4mm \times 25.4mm$  secondary target. This was accomplished using two collimators with  $8mm$  diameter holes placed  $90mm$  apart between the x-ray tube and secondary target, leading to a beam divergence of  $10^\circ$ . The detector was placed  $90^\circ$  from the direction of the original x-ray beam,  $5cm$  away from the midpoint of the secondary target, non-collimated. This distance was chosen as it lowered dead time to acceptable levels. The geometry is analogous to Figure 4.1, which was used for the theoretical calculations. This geometry was re-created for the simulation as well, so that the experimental and simulated results could be directly compared to the theoretical calculations.

For the GEANT4 simulation, a more realistic cone beam was chosen for the x-ray source output, using the same output files from Report78<sup>[30]</sup> for the energy spectrum. This source energy distribution was coded in GEANT4 using histograms. The size and angular distribution of the initial beam was chosen to mimic the experimental setup,

producing a spot  $10\text{mm}$  in diameter on the secondary target, with a  $10^\circ$  divergence angle.

The detector used in the experiment was also modelled, to detect the photons escaping the target, so that the results from the simulation could be compared to both theoretical and experimental findings. This was accomplished by inputting the physical detector characteristics in the simulation program (dimensions, materials and dead layers) and placing it  $5\text{cm}$  away from the midpoint of the secondary target, non-collimated, and at  $90^\circ$  from the direction of the original beam, matching the experimental setup. As photons travelled through the detector, the amount of energy each photon deposited into the detector active volume was tracked. More than 99% of the photons incident on the detector were fully absorbed, so this deposited energy was taken to be the total energy of the photon itself. These energies were recorded, and also blurred randomly using a Gaussian distribution, providing the broadening of energy resolution. The blurring weight was determined empirically by comparing the results of simulations to experimentally obtained results.

Of course, the GEANT4 simulation results also had to be tested for their accuracy. To do this, the results were compared to experiments performed using the real setup. The detector efficiency was verified and compared to the detector used in experiments using a simulated  $^{55}\text{Fe}$  source placed  $2\text{cm}$  away from the detector face. The results of this simulation and experiment can be seen in Figure 4.7. After simulating one million photons, the absolute peak efficiency was calculated and compared to the experimental absolute peak efficiency of the HPGe detector with the same  $^{55}\text{Fe}$  source placed  $2\text{cm}$  away. The two efficiencies were within 2% of each other.

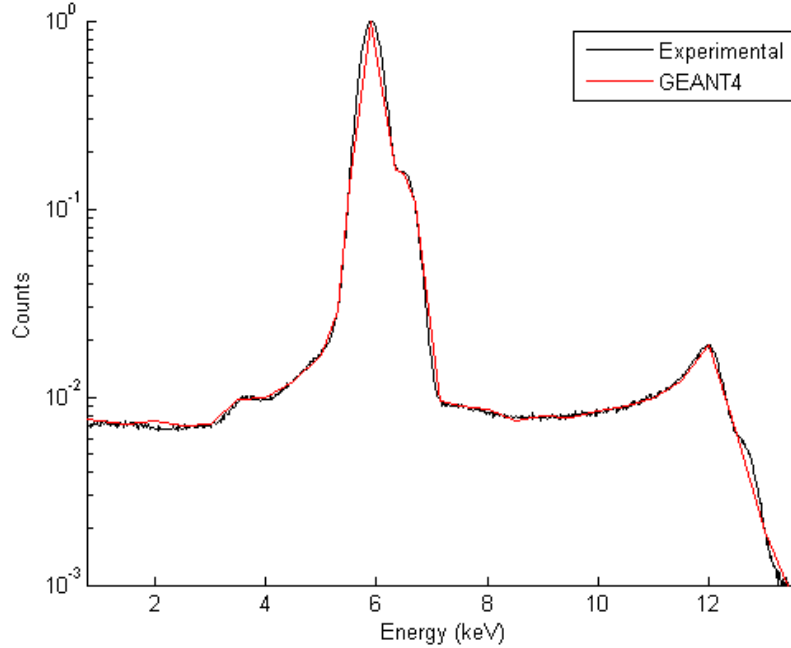


Figure 4.7: The experimental and simulated spectrum of an  $^{55}\text{Fe}$  source, detected with an HPGe detector. The main emissions of  $^{55}\text{Fe}$  are at 5.898 and 6.490keV.

The physics library used for the simulation was the *LowEMLivermorePhysics* library, which allows for accurate simulations of photons, electrons and protons down to the sub-keV level<sup>[19,34]</sup>. For each trial, ten billion photons were simulated such that the number of scatter and fluorescence peak area counts within the detector always exceeded 10000, making the statistical error  $< 1\%$ . Using GEANT4, it is possible to differentiate which physics process created the particle entering the detector volume, which makes identifying whether the particle scattered from the secondary target or was fluoresced possible. Deposited energy spectra of all particles incident on the detector were collected so that they could be compared to experimental results. Figure 4.8 show a comparison of the experimental output spectrum and GEANT4 output spectrum. The deposited energy spectra of the fluoresced and scattered photons were

also collected separately and were used to determine the probabilities for fluorescence production or scattering without having to curve fit the overall spectrum. In this case, the total number of photons from each interaction were simply integrated and set to be the total counts.

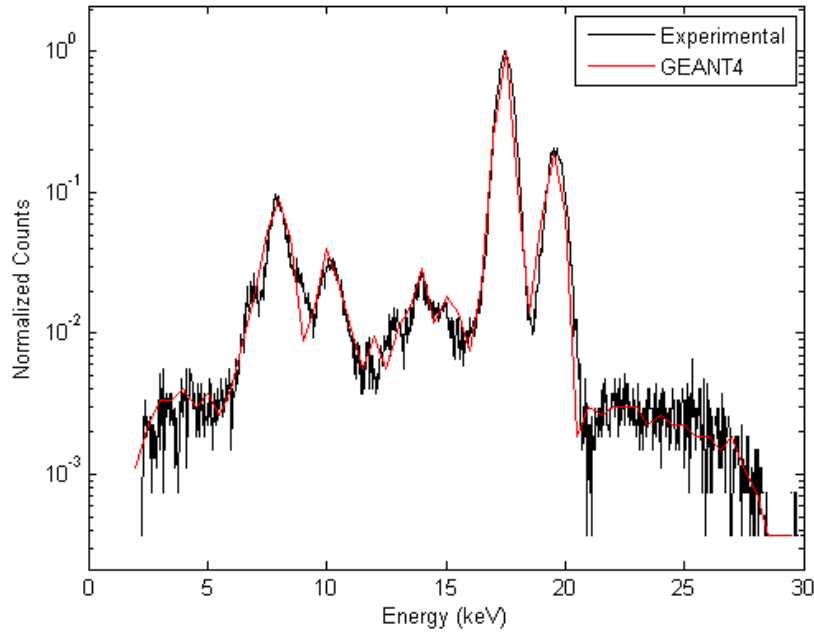


Figure 4.8: Output spectra, for a molybdenum secondary target and a tungsten anode x-ray tube with a potential of  $30kV$ . The counts have been normalized to the height of the molybdenum  $K_{\alpha}$  peak for comparison purposes. The two peaks at  $17.5keV$  and  $19.6keV$  are the  $K$  fluorescence peaks of molybdenum. All other features are a result of the tungsten anode x-ray tube spectrum being scattered.

For the experimental results, both the amount of fluorescence and scatter produced were determined from the spectra obtained. The spectra were fitted with curves in Matlab, taking the area under the fluorescence peaks to be the fluorescence signal and everything else being scatter. The spectra obtained were fit using an inverse variance weighted, non-linear least-squares method, which produces a result with the lowest

variance<sup>[35–38]</sup>. The curves were fit with an appropriate number of Gaussian curves, and a linear background. An example fit result is shown in Figure 4.9. The results then had to be normalized to the number of photons produced, since the theoretical results are based on a per photon interaction probability. To accomplish this, the theoretical x-ray production spectra taken from Report78 were used to determine the relative intensities produced at varying tube voltages.

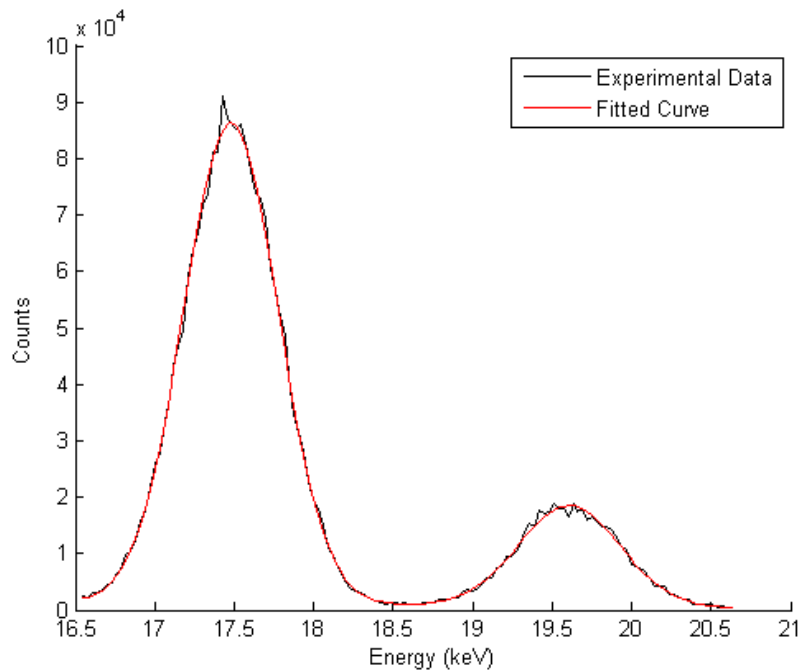


Figure 4.9: An example of the curves fit to fluorescence peaks. This example features the  $K$  lines of a molybdenum foil.

The theoretical model assumed that the incoming and outgoing x-rays travelled in a pencil beam geometry, which is not the case. Coherent and incoherent scattering do not occur isotropically, but they do have the same angular distribution (for low energy x-rays), whereas fluorescence production occurs isotropically. However, since geometry was consistent between the simulation and experimental results, angular

distributions can be ignored. When comparing to the theoretical results, only a solid angle correction was applied, to account for the actual geometry used. It is worth noting that minor discrepancies between the theoretical results and the simulation and experimental results may arise from this assumption. The solid angle between the x-ray tube and the secondary target, as well as between the secondary target and the detector were calculated analytically<sup>[39,40]</sup>. This was then turned into a geometric efficiency factor and all simulation and experimental spectra were corrected for it.

With these corrections, it was then possible to compare results from all three trials. To reduce the number of figures to represent the collected data, the simulation and experimental data points were connected with smoothed lines with colour matching the model results, allowing the general trends of the model to be easily verified.

Figure 4.10 shows the XRF production from a molybdenum secondary target, determined using all three methods, while Figure 4.11 and Figure 4.12 show the scatter produced and the fluorescence to scatter ratio respectively. Looking at the graphs, it is evident that the simulation follows the same trend as the theoretical model, with the only major differences occurring at lower thicknesses. This is further exemplified in the experimental work, in which thinner secondary targets produce much less fluorescence than expected at lower thicknesses. This is most likely caused by geometric effects not taken into account in the theoretical derivation, as it appears in both the simulation and experimental work.

Examining the figures, it is evident that the experimental and simulation results closely follow the trends calculated using the theoretical model. Similar results were found for all three secondary targets tested. This suggests that it should be safe to use an analytical calculation to determine the optimal thickness of secondary targets,

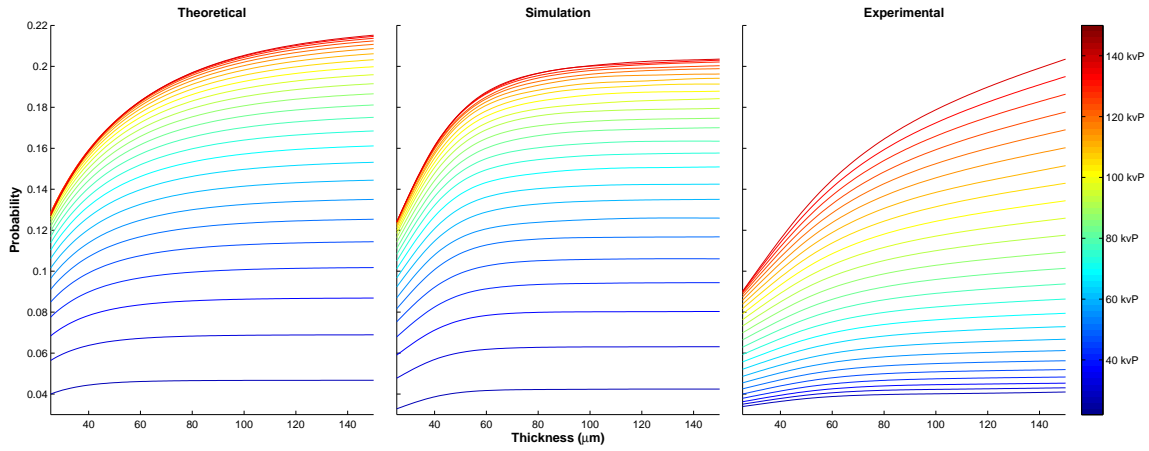


Figure 4.10: The fluorescence produced by a molybdenum secondary target, calculated using the theoretical model (left), simulation (middle), and experimentally (right). All graphs have identical axes to facilitate comparisons.

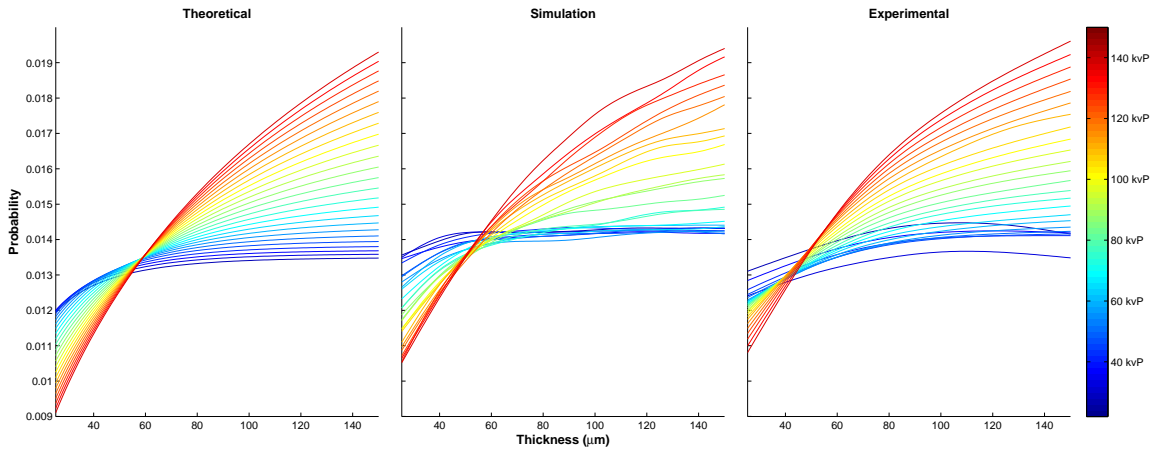


Figure 4.11: The scatter from a molybdenum secondary target, calculated using the theoretical model (left), simulation (middle), and experimentally (right). All graphs have identical axes to facilitate comparisons.

proving the usefulness of the model.

An important aspect to secondary target thickness selection is noting how much

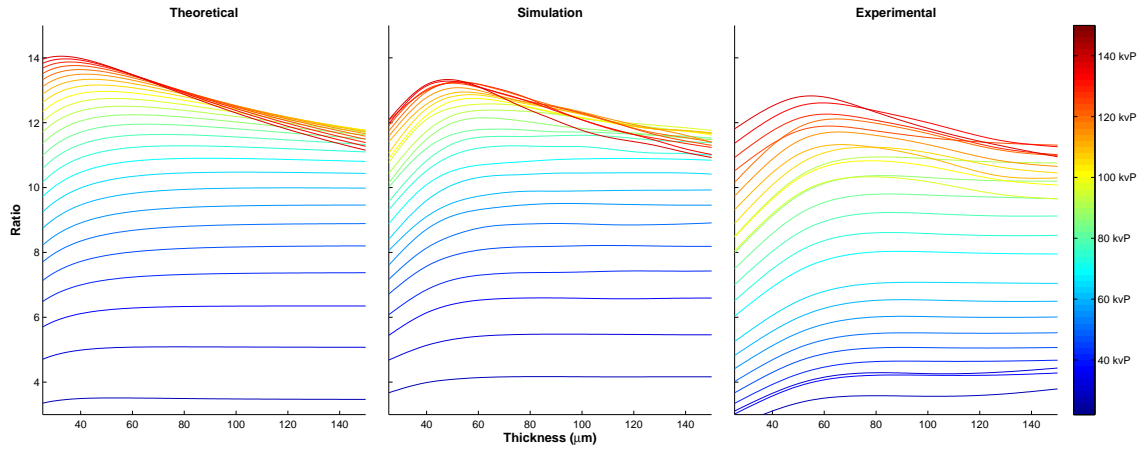


Figure 4.12: The fluorescence to scatter from a molybdenum secondary target, calculated using the theoretical model (left), simulation (middle), and experimentally (right). All graphs have identical axes to facilitate comparisons.

of an effect it will have on the overall system. To make a valid comparison, the value of the ratio of fluorescence to scatter at the optimal voltage and optimal thickness is compared to the ‘infinitely thick’ value at the optimal voltage. The secondary targets start to appear ‘infinitely thick’ at various points, but for the targets generally used, this occurs at thicknesses much lower than  $1\text{mm}$ . Unless the secondary target thickness received special consideration, it is likely that most experimental PEDXRF setups use targets that behave ‘infinitely thick’. Therefore, comparing the effect of choosing the optimal thickness to that of the ‘infinitely thick’ value is logical. Equation 4.7 shows the ratio of fluorescence to scatter produced by an infinitely thick secondary target.

$$\lim_{d \rightarrow \infty} \left( \frac{\frac{\omega_k \mu_{PE}(E_i) (1 - e^{-(\mu_{tot}(E_i) + \mu_{tot}(E_f))\sqrt{2d}})}{\mu_{tot}(E_i) + \mu_{tot}(E_f)}}{\frac{\mu_{sc}(E_i) (1 - e^{-(\mu_{tot}(E_i) + \mu_{tot}(E_{sc}))\sqrt{2d}})}{\mu_{tot}(E_i) + \mu_{tot}(E_{sc})}} \right)$$

$$= \frac{\omega_k \mu_{PE}(E_i) (\mu_{tot}(E_i) + \mu_{tot}(E_{sc}))}{\mu_{sc}(E_i) (\mu_{tot}(E_i) + \mu_{tot}(E_f))} \quad (4.7)$$

This result is valid for a single energy, so it must be calculated at each energy and weighted with the tube output spectrum before it can be compared to the optimal thickness value. Table 4.2 shows the optimal tube potential and thickness. It also compares the fluorescence to scatter ratio at the optimal thickness value to the ‘infinite thickness’ value. This comparison shows the improvement in fluorescence to scatter ratio when selecting the optimal thickness.

Table 4.2: A table showing the optimal voltage, thickness, and a comparison of the fluorescence to scatter ratio at the optimal thickness to the ‘infinite thickness’ for various commonly used secondary targets. These results were taken from the model described in Section 4.1.1.

<b>Secondary Target</b>	<b>Optimal Voltage (kV)</b>	<b>Optimal Thickness (<math>\mu m</math>)</b>	<b>Optimal/Infinite Thickness</b>
<b>Copper</b>	40	25	1.06
<b>Molybdenum</b>	150	32	1.95
<b>Tin</b>	150	99	1.27

It can be seen that both the optimal thickness and tube potential vary for each target material. In addition, the voltages (and therefore thicknesses) will change depending on specific x-ray tube characteristics, which will alter the output spectrum. It is evident from the last column in Table 4.2 that these calculations are worthwhile,

since choosing the optimal secondary target thickness can result in up to a two times increase in fluorescence to scatter ratio when compared to the ‘infinitely thick’ solution. Even in the lowest cases, a 6% increase in fluorescence to scatter ratio should help improve the results of a PEDXRF system.

It is worth noting that optimizing the fluorescence to scatter ratio of the secondary target does not necessarily translate into improved MDLs for a PEDXRF system. In PEDXRF, the MDLs are limited by the Signal-to-Noise Ratio (SNR)<sup>[27]</sup>, which can be defined as shown in Equation 4.8<sup>[18]</sup>.

$$MDL \propto \frac{1}{SNR}, \quad SNR = \frac{fluorescence}{\sqrt{background}} \quad (4.8)$$

It should be noted that in this definition of SNR, the background refers only to counts in the same region as the fluorescence. While the fluorescence to scatter ratio calculated using the model should provide some improvement to the MDLs, the fact that the scatter is polarized, can still interact with the sample to provide sample fluorescence, and must interfere with the fluorescence peak to be considered background, the effect is not immediately evident. As a result, the effects of secondary target thickness on the MDLs of a PEDXRF system are discussed thoroughly in Section 4.1.4.

### 4.1.3 PEDXRF Geometry

Another area of PEDXRF systems that can be optimized is the geometry. As discussed previously, the geometry chosen for PEDXRF systems use two mutually perpendicular 90° beam paths to reduce scatter incident on the detector. In order to completely reject scatter, the beam paths would have to be infinitely narrow,

and exactly  $90^\circ$  from each other. In reality, the beam paths have some width and beam divergence, which makes optimizing the geometry a worthwhile endeavour. If the beam is too narrow, then the fluence detected (both signal and scatter) drops drastically, while too large of a beam path reduces the effectiveness of a polarized system.

A theoretical model for optimized PEDXRF geometry was previously developed, which focused on optimizing the SNR<sup>[18]</sup>. This work suggests that there is a relationship between the solid angle of a collimated beam,  $\Omega$ , and its degree of polarization,  $P$ , stating that  $P \propto \Omega$ .

Assuming the collimators are all identical in the setup, providing a solid angle  $\Omega$ , it is reasonable to assume that the fluorescence response of the sample should be proportional to  $\Omega^3$ , since it does not rely on any polarized effects. The scatter however, which depends on the degree of polarization, is therefore related to  $\Omega^4$ <sup>[18]</sup>. This results in a SNR related to  $\Omega$ , according to Equation 4.8. This suggests that it is ideal to have all collimators as large as possible, as the benefit of increased solid angle outweighs the increased scatter response.

This approach to optimizing the geometry makes a number of assumptions about the system, the largest being that all solid angles along each beam path are the same, and contribute equally to the detected signal. In order to examine the effects of each beam path, the GEANT4 code described in Section 4.1.2 was adapted to include the full tri-axial geometry shown in Figure 2.8, with various collimator sizes and placements. Simulations were run with a copper secondary target,  $25\mu\text{m}$  thick, with the same x-ray tube described above.

The detector was switched for this experiment from an HPGe detector to a Si(Li),

which is more suitable for the energy range of interest. The detector was an ORTEC Si(Li) detector (5.62mm crystal thickness, 8cm<sup>2</sup> active area), with an energy resolution of 220eV at 5.9keV (<sup>55</sup>Fe energy). The sample was chosen to be a distilled water phantom, with 100μg/g of iron added, which mimics a soft tissue sample with increased iron content. The iron was added in the form of an iron standard solution, ULTRAgrade ICP-026, purchased from Ultra Scientific, 1000μg/mL, mixed with distilled water and 2% HNO<sub>3</sub>. The rest of the simulation setup is discussed thoroughly in Section 4.1.4. For notation purposes, the collimators along each beam path were numbered, *i.e.* the collimators between x-ray tube and secondary target were referred to as stage one collimators, stage two between secondary target and sample, stage three between sample and detector.

Using the GEANT4 code, it is possible to determine the polarization of each photon at any point. It was decided to track the polarization at the sample (before interaction), of all photons incident on the detector, providing information on how each collimator stage affects the overall polarization of detected photons. The polarization measurements are reported as a normalized three dimensional vector, corresponding to the components of the polarization along each cardinal axis. To quantify the polarization of a single photon, the square of the component along the expected polarized axis is used (in this case, the *Z* axis). Figure 4.13 shows the degree of polarization of scattered photons (not fluoresced from the secondary target) at the sample, with various stage two collimator diameters. It is evident that a smaller solid angle yields a higher degree of polarization, as expected.

To compare the effectiveness of each stage collimator on polarization, the overall degree of polarization is used. To determine the overall degree of polarization, the

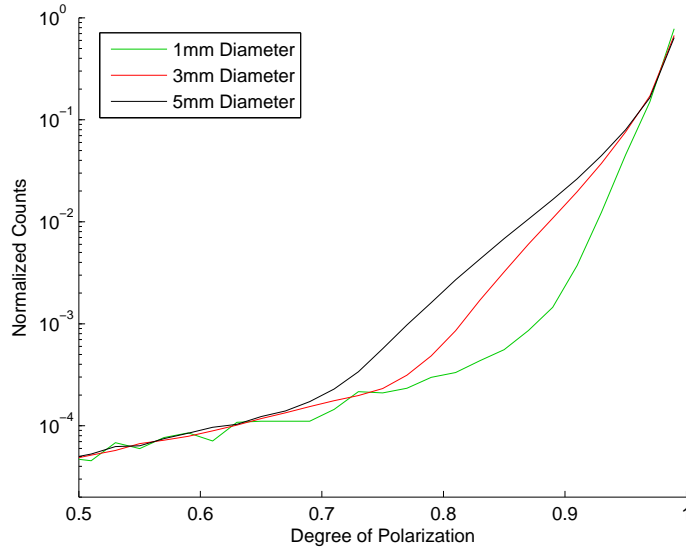


Figure 4.13: A histogram of the number of detected scatter photons for each degree of polarization, taken at the sample, for various stage two collimator diameters. The counts are normalized to compare the effect of collimator width on the overall degree of polarization.

degree of polarization for each photon is summed, normalized to total photon number, as shown in Equation 4.9. This yields the average degree of polarization for the entire beam.

$$\text{Overall Polarization} = \frac{1}{N} \sum_{i=1}^N \text{Degree of Polarization} \quad (4.9)$$

The collimators were varied from 1 – 5mm in diameter, along each stage individually, keeping the other two collimators at 5mm. Looking at just the scattered photons, the overall degree of polarization for various collimator widths was determined, shown in Figure 4.14. Again, fluorescence counts from the sample and secondary target were excluded, since they are expected to be non-polarized. It is evident from Figure 4.14

that the three stages do not contribute equally to the overall polarization of the scattered photons. Rather, the stage two collimators seem to have the greatest effect on overall polarization, while the third stage collimators provide almost no effect, other than limiting overall fluence.

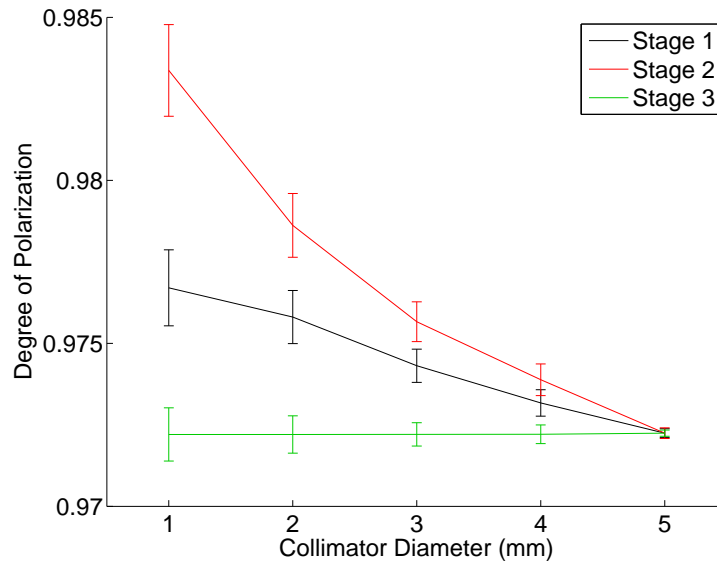


Figure 4.14: A figure showing the degree of polarization as a function of collimator diameter, changing only one stage collimator at a time, keeping the other two stage collimators at  $5\text{mm}$ . The error bars represent Poisson error in the number of counts.

This experiment warranted further research into whether this information could be exploited to affect the MDLs of the overall PEDXRF system, by looking at optimizing the collimators of each beam path separately. This work is covered in Section 4.1.4.

## 4.1.4 Fully Optimizing PEDXRF

### Introduction

After a thorough examination of both the secondary target and collimators, it was evident there was room to improve on current PEDXRF designs. A GEANT4 simulation was setup to correspond to the full experimental setup, and two experiments were run. The first experiment involved varying the secondary target thickness, and exposure settings, to see if the optimal fluorescence to scatter ratio affects SNR (and therefore the MDLs) when measuring a sample. The second experiment focused on the SNR for various collimator configurations, comparing to the theoretical model described in Section 4.1.3. Together, these results were combined to fully optimize the PEDXRF system.

The following results presented in this chapter were accepted for publication in X-Ray Spectrometry<sup>[27]</sup>. The simulation and experimental work was performed by the author of this thesis, under the supervision of Dr. Michael J. Farquharson and Dr. Soo-Hyun Byun. The data, figures, results, and conclusions presented in that paper were reformatted and edited, with permission from the copyright holder, to produce the remainder of this chapter.

### Theory

As discussed earlier, it is of great interest to investigate whether an increase in the fluorescence to scatter ratio coming from the secondary target would play a significant role in the MDLs of a system. While it is true that the MDLs depend partly on the sample fluorescence to scatter ratio, it is not trivial to determine the effect that the secondary target fluorescence to scatter ratio has on the detected spectrum

analytically. This is compounded by the fact that the scatter from the secondary target is polarized, while the fluorescence is not, making an analytical approach significantly more difficult. Such an approach would require a separate solution for the polarized and non-polarized photons, at each energy, over all solid angles, which must then be properly summed and normalized. Instead, a MC simulation and experiment were designed to directly determine the effect of the secondary target thickness on the detected spectrum from a sample.

Examining the effect that varying collimation has on the performance of a PEDXRF system is another difficult task. It is well known that the differential cross section for polarized x-ray scatter follows a  $\sin^2\Psi$  relationship, where  $\Psi$  is the angle between the scattering direction and the polarization direction<sup>[22]</sup>. Restricting the number of available scatter angles will improve scatter rejection, but will reduce the total solid angle, decreasing the probability of measuring the fluorescence signal. The addition of multiple scattering stages, with potentially different collimation, makes an analytical solution impossible without significant simplifications.

The MDL was chosen as the most important factor for a PEDXRF system; the goal of the system is to produce the lowest MDL, shown in Equation 4.8. Any further discussion of optimization focuses on maximizing the SNR, thus reducing the MDL .

## Materials and Methods

Two experiments were performed to determine the effects of secondary target thickness and collimation on the SNR for a PEDXRF geometry. In the secondary target thickness experiment, the geometry was fixed and metallic fluorescers of various thickness were used. In the geometry experiment, the secondary target was fixed,

and collimators with different hole sizes were used to limit solid angle. In order to determine the effect of secondary target thickness, and from the model outlined in Section 4.1.3 for collimation, simulations of the experiments to be run were done using the GEANT4 MC code. The simulation setup was identical the setup outlined in Section 4.1.2, except it used the *EMLivermorePolarizedPhysics* list, which includes polarized photon interactions.

For a single simulation (one secondary target thickness and collimator setup),  $10^9$  photons were simulated. Each photon was tracked until its energy was below the  $500eV$  cut-off for the physics list, at which point all remaining energy was deposited in the local medium. All energy deposited from a single photon in the sensitive volume of the detector was recorded, and put into a spectrum. This allowed for a direct comparison between the simulated spectra and experimentally obtained results. After the simulations were performed, the experiments were carried out in the lab.

The x-ray tube used was described previously in Section 4.1.2, while the detector used was the Si(Li) detector described in Section 4.1.3. The PEDXRF apparatus, shown in Figure 3.6 consisted of three lengths of aluminum tubing with an inner radius of  $12.7mm$ . The aluminum tubes were welded at  $90^\circ$  angles, and cut at the corners to allow for secondary target and sample placement. For the MC simulations, the tubes were all  $2cm$  long, while experimentally, the stage 1 tube was  $2.5cm$  long, the stage 2 tube was  $2cm$  long and the stage 3 tube was  $1.5cm$ . These distances were required to work around other equipment in the lab room. As a result, the MC solid angles and experimental solid angles do not match perfectly, but rather provide a larger range of tested solid angles.

For the secondary target thickness experiment, the secondary targets chosen to

be examined were copper (Cu), molybdenum (Mo) and tin (Sn). Cu and Mo are two common metallic secondary targets<sup>[9-11,13,31-33]</sup>, while Sn was chosen to see if the trend was consistent at higher atomic numbers. The secondary target thicknesses were identical to those used in Section 4.1.2. The voltage was chosen to be  $30kV$  for the Cu trial, and  $50kV$  for the Mo and Sn, which allowed for significant x-ray production in the energy range of interest, while avoiding the production of higher energy x-rays that are much more likely to scatter. In order to fully utilize a metallic secondary target, the primary spectrum must contain a significant number of photons above the Photoelectric absorption edge of the secondary target. This is why the higher potential of  $50kV$  was chosen for the Mo and Sn targets.

A measurement was also performed to determine the effects of changing the input voltage, but was only run with the Cu secondary target material. For this measurement, the voltage was varied from  $30kV$  to  $50kV$  in steps of  $10kV$ . For all measurements, the current was set to be  $20mA$ , and spectra were collected for 60 minutes real time. Dead time effects were negligible, but nonetheless corrected for using the non-paralyzable dead time model.

For the collimation experiment, interchangeable collimators with various hole sizes were made. Annular lead collimators, shown in Figure 3.7, were made with inner radii  $0.8mm$ ,  $1.6mm$ ,  $2.4mm$ ,  $3.2mm$ , and  $4.8mm$ , all with an outer radius of  $12.7mm$ . The collimators in each stage were changed separately, while a  $4.8mm$  collimator was placed in the other two stages. This allowed for examination of the individual effect of collimating each stage had on the SNR. The collimators were placed  $5mm$  into each stage tube, measured in the beam direction. For this experiment, a  $25.4\mu m$  Mo secondary target was used, the tube was set to  $50kV$  and  $25mA$ , and spectra were

collected for 60 minutes real time. For the GEANT4 simulations, the collimators were made with  $1\text{mm}$ ,  $2\text{mm}$ ,  $3\text{mm}$ ,  $4\text{mm}$ , and  $5\text{mm}$  holes, and the Mo target was  $25\mu\text{m}$  thick. The total solid angle was calculated numerically for each configuration.

## Results and Discussion

### Comparing Simulation and Experimental Results

In order to verify that the MC simulation was providing valid results, the output spectra should be compared to the experimental output spectra. Figure 4.15 shows the comparison of an experimental spectra with a simulated one, for the  $25.4\mu\text{m}$  Mo secondary target. The experimental spectrum is shown in blue, while the simulated spectrum is shown in red. Figure 4.16 is a figure of the same spectra, zoomed in on the  $0 - 15\text{keV}$  range, showing more detail.

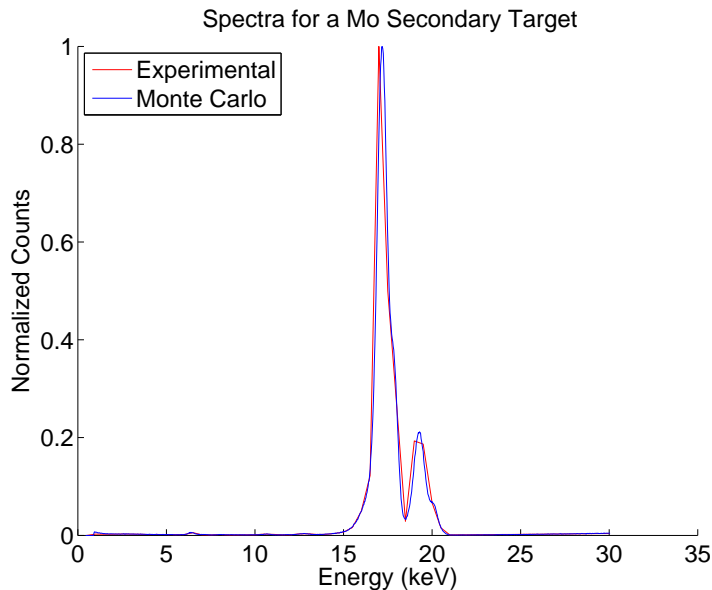


Figure 4.15: A plot of simulated and experimental spectra obtained for an iron phantom from the thinnest Mo secondary target.

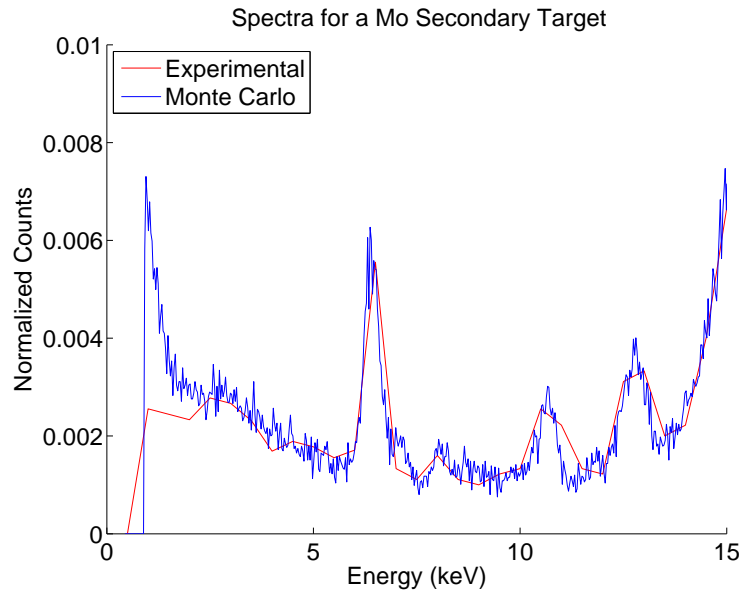


Figure 4.16: A plot of simulated and experimental spectra obtained for an iron phantom from the thinnest Mo secondary target, zoomed in on the 0 – 15keV range.

It can be seen from Figure 4.15 and Figure 4.16 that the simulation results match those obtained experimentally. Comparing other spectra yielded similar results. It should be noted that the differences between the experimental and simulated spectra shown in Figure 4.16 at approximately 2keV are caused by electronic noise, which was not included in the simulation results.

### Secondary Target Thickness

#### Copper Secondary Target Thickness

The sample fluorescence as a function of Cu secondary target thickness is shown in Figure 4.17. The error bars on MC data represent Poisson error, and the error bars for experimental data come from fitting algorithms. It can be seen that as the secondary target thickness increases, the sample fluorescence also increases to a certain point,

then remains unchanged for all other thicknesses. As the thickness increases, initially the number of secondary target fluoresced photons increases, eventually reaching the self-absorption thickness. This thickness for Cu is approximately  $50\mu m$ . At this point, further increases in secondary target thickness only produce more scatter, which can help excite the sample, but is usually further away from the absorption edge, providing minimal benefit. It is easy to tell in Figure 4.17 that once the self-absorption thickness is achieved, the number of sample fluorescence photons stops rapidly increasing, verifying that scattered photons add little to the measured spectrum. At the ‘infinite thickness’ of Cu, no additional secondary target fluorescence or scatter is produced, and the sample fluorescence reaches a maximum value.

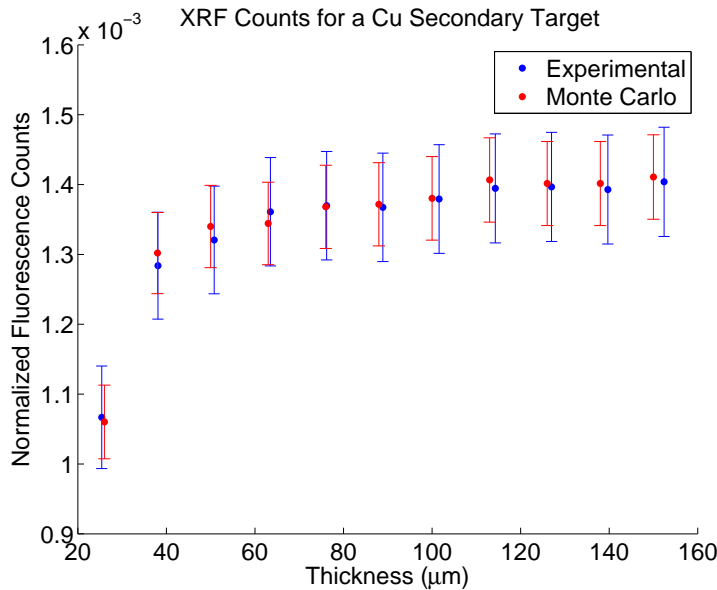


Figure 4.17: A plot of sample XRF counts, normalized to total counts, versus secondary target thickness for a Cu secondary target. The sample fluorescence stops increasing rapidly at approximately  $50\mu m$ , and stops increasing altogether at approximately  $100\mu m$ .

Figure 4.18 shows the background counts surrounding the fluorescence peaks, as a

function of Cu secondary target thickness. Once again, it can be seen that there is a rapid increase in background counts as secondary target thickness begins to increase, but eventually stops due to self-absorption effects. The number of background counts stops changing at approximately  $100\mu m$ , which matches very closely to the ‘infinite thickness’ of a Cu target for a  $30keV$  photon.

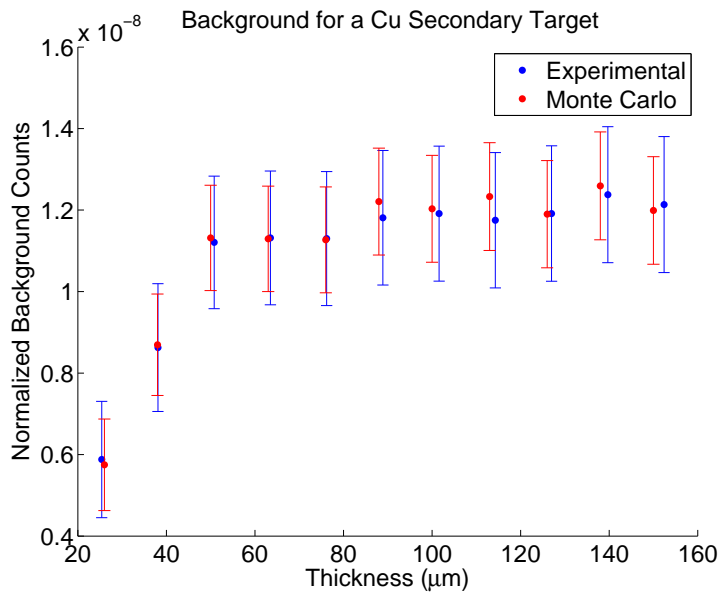


Figure 4.18: A plot of background counts, normalized to total counts, versus secondary target thickness for a Cu secondary target. The number of background counts increases rapidly until approximately  $50\mu m$ , and stops increasing altogether at approximately  $100\mu m$ .

The SNR was calculated for each secondary target thickness using Equation 4.8, shown in Figure 4.19. From this graph, it can be seen that the thinnest Cu secondary targets actually produce the highest SNR, as hypothesized. Once the secondary target has reached its fluorescence self-absorption length, there are drastically decreased amounts of sample fluorescence gained by increasing thickness further. After this thickness, the XRF response stops growing. The secondary target scatter increases

at a much higher rate when compared to the XRF response, until the ‘infinite thickness’ is reached. Combining these two effects, the SNR is maximal with thinner Cu secondary targets. For this specific setup, it was found that a Cu target of  $25\mu\text{m}$  was optimally thick, producing an SNR of  $13.9 \pm 0.5$ , while the ‘infinitely thick’ secondary target had an SNR of  $12.7 \pm 0.4$ . This represents an increase of  $9.4 \pm 0.5\%$ , merely by selecting a secondary target at the optimal thickness.

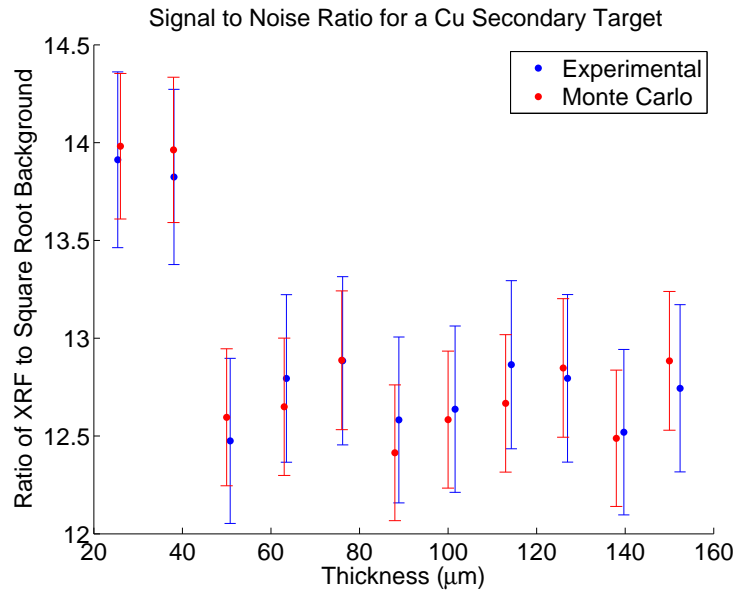


Figure 4.19: A plot of SNR versus secondary target thickness for a Cu secondary target. The optimal thickness is found at  $25\mu\text{m}$ , with SNR dropping rapidly after approximately  $40\mu\text{m}$ .

### Varied Voltage with a Copper Secondary Target

To determine the effect that changing the tube potential has on the overall results, experiments on the Cu secondary targets were run. Figure 4.20 shows the experimental results of running varying secondary target thickness and input voltage has on the SNR. Comparable to Figure 4.19, the results show that the thinnest secondary targets

produce the highest SNR, at all input potentials. The optimal Cu secondary target thickness is also independent of voltage, as it occurs at approximately  $25 - 40\mu\text{m}$  for all three potentials. It is also noted that the SNR is independent of fluence rate, so the effect seen by changing input potential is caused by the change in mean photon energy.

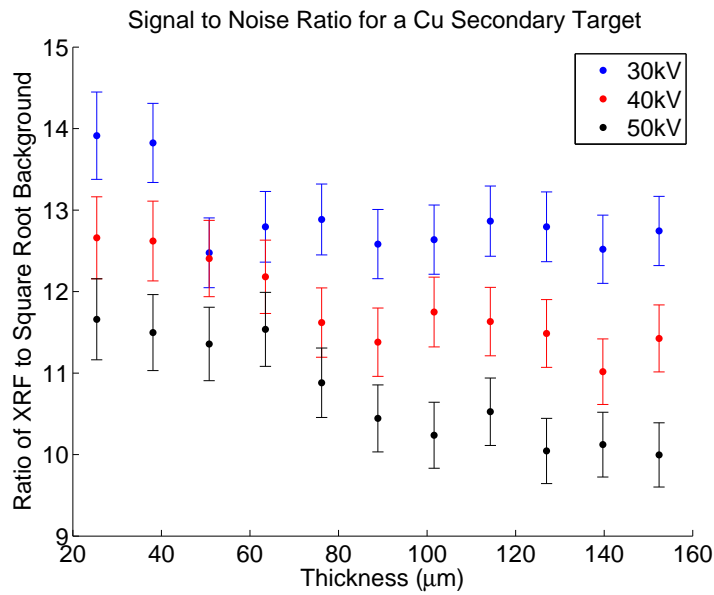


Figure 4.20: A plot of experimentally measured SNRs versus secondary target thickness for a Cu secondary target at various input potentials. The optimal thickness is found at  $25\mu\text{m}$  for all input voltages, and lower potentials provide better SNR on a per photon basis.

The closer the mean photon energy is to the absorption edge of the element(s) of interest, the higher the probability of producing sample fluorescence. The result of this effect is that the number of measured fluorescence photons, normalized to fluence rate, will increase with decreased tube potential, as long as the mean energy remains above the absorption edge. Additionally, as the mean photon energy increases, its penetrating depth in a material also increases. This means that the higher energy

photons are more likely to produce scatter that will be incident on the sample. This should result in an increase in the measured background counts, and an increased ‘infinite thickness’ for the secondary targets. As tube potential is increased, the effects of decreased fluorescence probability and increased background combine to produce the significantly lower SNRs apparent in Figure 4.20. The effect of increased secondary target ‘infinite thickness’ can also be seen in Figure 4.20, as the higher potential SNRs continue to drop at increased thicknesses, until the new ‘infinite thickness’ is reached.

The results of this experiment are summarized in Table 4.3. The optimal SNR was taken at the optimal thickness, the ‘infinitely thick’ SNR was taken at the maximum measured thickness. The percent increase shows the increase in SNR by switching from an ‘infinitely thick’ secondary target to the optimally thick one. One result worth noting is the percent increase rising with tube potential. While it is true that the optimal SNR decreases with increased tube potential, the difference between the max and ‘infinitely thick’ SNR is highest for higher potentials. This is caused by the increased scatter at higher potentials causing the SNR to continue to decrease at larger thicknesses. As a result, when operating further away from the optimal voltage setting, the percent gain from using the optimally thick secondary target is much greater. This trend is expected to continue with increased tube potential.

<b>Tube Potential</b>	<b>Optimal SNR</b>	<b>‘Infinitely Thick’ SNR</b>	<b>Percent Increase</b>
<i>30kV</i>	$13.9 \pm 0.5$	$12.7 \pm 0.4$	$9.4 \pm 0.5\%$
<i>40kV</i>	$12.7 \pm 0.5$	$11.4 \pm 0.4$	$11.4 \pm 0.6\%$
<i>50kV</i>	$11.7 \pm 0.5$	$10.0 \pm 0.4$	$17 \pm 1\%$

Table 4.3: The results of how changing tube potential affects the SNRs in a PEDXRF system.

### Molybdenum Secondary Target Thickness

Figure 4.21 shows the SNR as a function of Mo secondary target thickness. It can be seen that in this case, the optimal thickness occurs at approximately  $50\mu m$ . Since Mo has a higher atomic number than Cu, the secondary target fluorescence will have a higher energy, increasing its penetration depth. As a result, the thickness of the secondary target which the Mo fluorescence can escape is greater than the distance in Cu that Cu fluorescence can escape. Until the Mo secondary target reaches this thickness, both the fluorescence and scatter increase, as does the SNR. Once this thickness is reached, no more secondary target fluorescence is produced, but more scatter is, causing the SNR to subsequently drop, as was the case with the Cu secondary target.

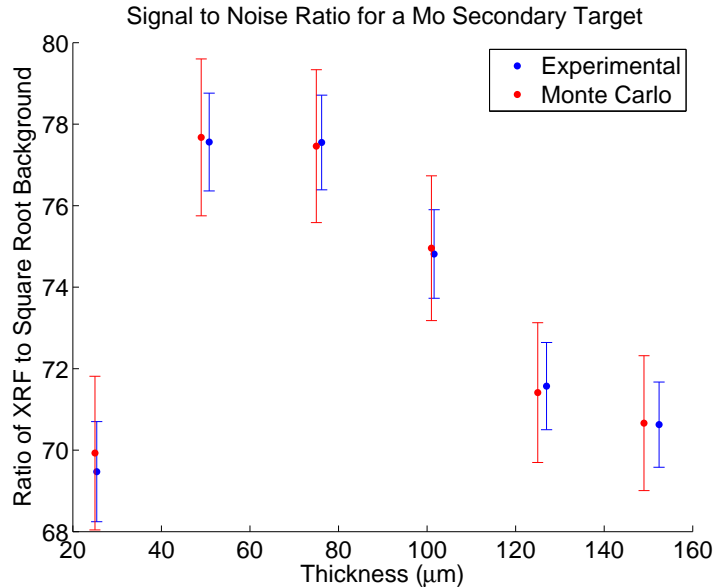


Figure 4.21: A plot of SNR versus secondary target thickness for a Mo secondary target. The optimal thickness is found at approximately  $50\mu m$ , with SNR building up until  $50\mu m$ , and dropping rapidly after approximately  $80\mu m$ .

As seen in Figure 4.21, at optimal thickness the SNR for a Mo secondary target

was found to be  $78 \pm 1$ , while the ‘infinitely thick’ SNR was found to be  $71 \pm 1$ . This leads to an increase of  $8.5 \pm 0.2\%$  by choosing the optimally thick secondary target. The remarkable increase in SNR as compared to the results for the Cu secondary targets is caused mainly by the mean photon energy from the tube output ( $31\text{keV}$ ) being closer to the absorption edge of Mo, greatly increasing the number of fluoresced x-rays from the secondary target. While the Cu fluorescence is much more likely to cause the Fe in the sample to fluoresce, the increased yield of Mo x-rays produced outweighs the benefit of increasing fluorescence probability. This also demonstrates another chance for system optimization; carefully choosing the tube potential and secondary target element to match the trace element(s) to be measured.

### **Tin Secondary Target Thickness**

A Sn secondary target of varying thickness was tested to determine if the trends continue at higher atomic numbers. Figure 4.22 shows the SNR as a function of Sn secondary target thickness. In this case, the optimal thickness is found to be approximately  $90\mu\text{m}$ . As was the case with the Mo secondary target, the trend of increasing atomic number causing an increased optimal thickness is present in Figure 4.22 as well, caused mostly by the increased secondary target fluorescence energy.

Unlike the previous results, the decrease in SNR at thicknesses greater than the optimal thickness is much slower. This is caused by the increased fluorescence energy of Sn x-rays. These x-rays are quite penetrating, making the distance they can travel in Sn very far when compared to the other secondary targets examined. The self-absorption length of Sn x-rays is approximately double the length of Cu x-rays and

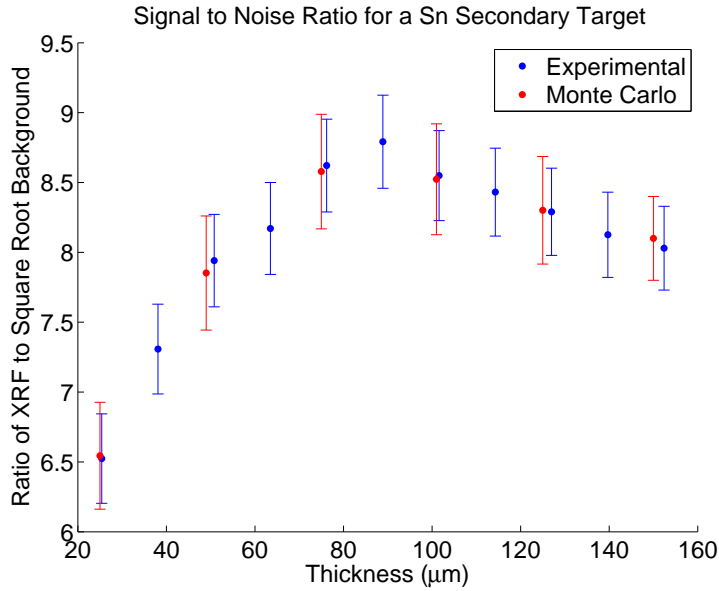


Figure 4.22: A plot of SNR versus secondary target thickness for a Sn secondary target. The optimal thickness is found at approximately  $90\mu m$ , with SNR building up until  $90\mu m$ , and dropping off slowly after  $90\mu m$ .

50% longer than Mo x-rays. In this case, the Sn x-rays can travel almost as far as the scattered x-rays, making the difference between the optimal thickness and the ‘infinite thickness’ much less apparent. For the Sn secondary target, at the optimal thickness the SNR was found to be  $8.8 \pm 0.3$ , and the SNR at ‘infinite thickness’ was found to be  $8.0 \pm 0.3$ , making the percent increase  $6.3 \pm 0.3\%$ . This verifies the fact that the drop off appears more gradual. The decrease in SNR compared to the Cu and Mo secondary targets is caused by the increased secondary target fluorescence energy. Since this energy is much higher than the K absorption edge of Fe, the probability of producing fluorescence is decreased.

## Summary

It is hypothesized that an optimal secondary target thickness exists for all metallic secondary targets, which increases as the atomic number of the secondary target increases. This has been shown to be the case for Cu, Mo, and Sn secondary targets, when looking at an Fe solution sample. This optimal thickness does not vary with tube potential, but the effect of choosing the optimal thickness is more important when not operating at the optimal potential. The optimal thickness found was  $25\mu\text{m}$  for Cu,  $50\mu\text{m}$  for Mo, and  $90\mu\text{m}$  for Sn.

Using the optimal thickness can provide increases to SNR (and therefore decreases to MDLs) of 6–17%, when compared to the ‘infinite thickness’ value. This is a logical value to examine, as the ‘infinite thickness’ for many common secondary targets is below  $200\mu\text{m}$ , making it trivial for a secondary target to act ‘infinitely thick’. The benefit of choosing the optimal thickness is highest when operating at a non-optimal tube potential, and decreases with increased atomic number. On a per-photon basis, the optimal tube potential is found by keeping the mean photon energy as close to the absorption edge of the metallic secondary target, thus increasing the probability of secondary target fluorescence.

## Optimal Collimation

For the optimal collimation experiment, the sample fluorescence and background were also measured, and the SNR calculated to determine the effects of changing setup collimation. For this experiment, the collimator in a single stage was changed, leaving the other two unchanged. The stage 1 and 2 collimators work together to polarize the x-ray beam, and the stage 2 and 3 collimators allow for the rejection of

scatter. By changing only a single collimator, the effect of collimating each single stage could be examined.

Figure 4.23 shows the simulation and experimental results for sample fluorescence as a function of total solid angle. The data points representing changes in stage 1 collimators are shown in black, 2 red, and 3 blue. Experimental data is denoted by points, while simulations results are shown as stars. The data were fitted with lines of best fit, with colours matching the stage colours. The error bars on MC data represent Poisson error, and the error bars for experimental data come from fitting algorithms. To compare with the theoretical model outlined in Section 4.1.3, the data from each stage were fitted with a line. It is worth noting that while the lines fit the data well, the slope for each stage is different ( $106 \pm 3$ ,  $98 \pm 5$ , and  $88 \pm 8$  for stage 1, 2, and 3 respectively). This suggests that changing collimators in different stages will provide different effects on the overall result. From Figure 4.23, it is obvious that the stage 1 collimator has the greatest effect on sample fluorescence, while the stage 3 collimator has the smallest effect.

The background produced with various collimators in each stage was measured. Figure 4.24 shows the simulation and experimental results, with curves of best fit for each stage. According to the theoretical model outlined in Section 4.1.3, the background is expected to increase as  $SA^{4/3}$ . The data was fitted with curves of the form  $slope * SA^\alpha$ , allowing  $\alpha$  to vary between 1 – 2. It was found that within error, the exponents are all equal to  $4/3$ . Once again, the slope of the curve for each stage varies, with stage 3 collimators having the greatest effect on background, and stage 1 collimators having the smallest effect ( $2300 \pm 100$ ,  $2070 \pm 60$ , and  $1850 \pm 80$  for stage 1, 2, and 3 respectively).

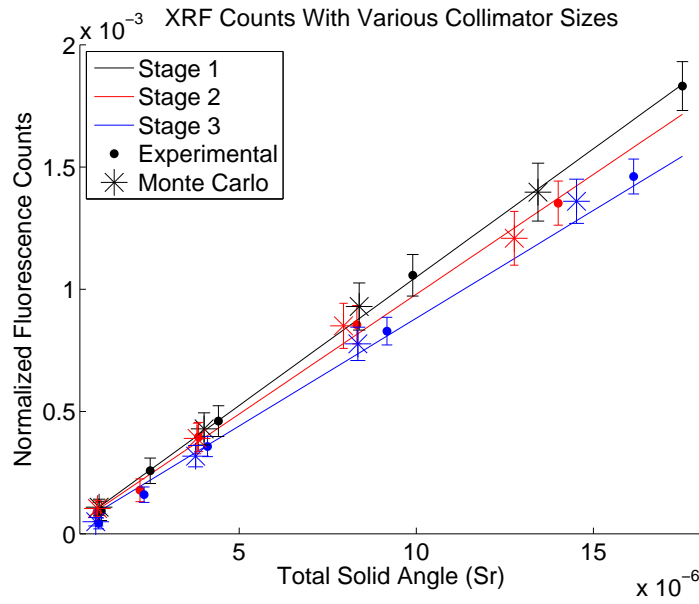


Figure 4.23: The sample fluorescence as a function of total solid angle, changing collimators in one stage at a time.

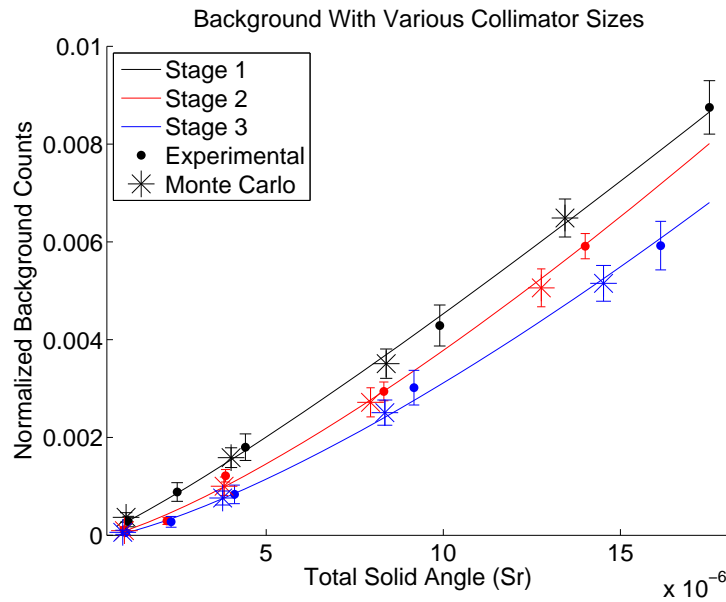


Figure 4.24: The background counts as a function of total solid angle, changing collimators in one stage at a time.

Finally, the SNR was calculated, in order to determine the optimal collimation. Figure 4.25 shows the SNR, once again with curves of best fit, to compare with the theoretical model outlined in Section 4.1.3. The curves were of the form  $slope * SA^\beta$ , allowing  $\beta$  to vary between 0 – 1. The exponents for the stage 1 and 3 collimators were equal to the theory ( $1/3$ ) within error, but the stage 2 collimator had a different exponent ( $0.08 \pm 0.02$ ). Another interesting feature of Figure 4.25 is the fact that varying the stage 2 collimator provides the best SNR at any total solid angle. One possible explanation for this is that the stage 2 collimator acts to both limit the range of polarizations (stage 1 and 2 collimators), as well as limit the range of scatter angles (stage 2 and 3 collimators). Because the stage 2 collimator assists in both parts of the scatter reduction via polarization technique, it's unsurprising that it has the largest effect on the SNR.

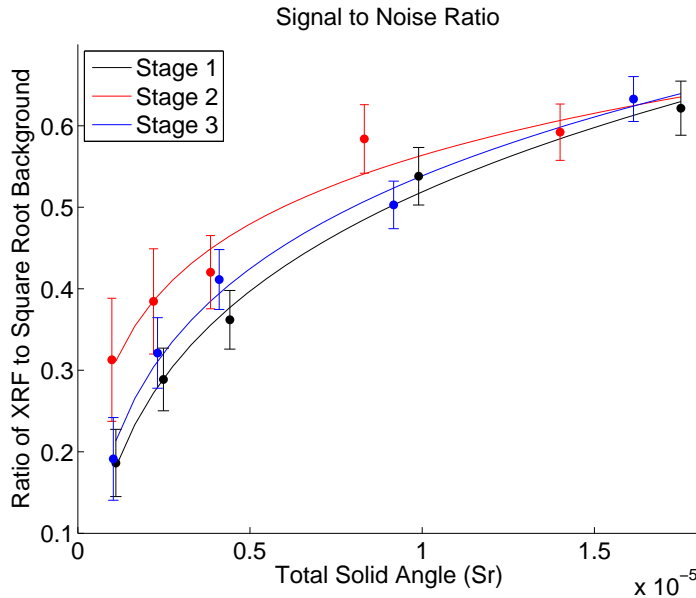


Figure 4.25: The SNR as a function of total solid angle, changing collimators in one stage at a time. Only the experimental data is shown.

Agreeing with the theory, the highest SNR is found when all collimators are as

large as possible. However, this does not mean that using largest collimators is always the best choice. In many EDXRF experiments, the total count rate is limited by detector dead time. In this scenario, reducing the total solid angle will allow for an increased fluence rate on the detector. In situations where the tube current can be increased to match a decrease in total solid angle, using the largest collimators will not provide the best SNR<sup>[18]</sup>.

If the tube current can be increased to make up for solid angle losses, then the SNR should be divided by total solid angle. This new SNR will help decide on optimal collimation in this situation. Figure 4.26 shows the SNR divided by solid angle. It is clear to see that the optimal collimators are as small as possible, and changing the stage 2 collimators provide the greatest increase in SNR. As a result, the optimal collimation is achieved by keeping the stage 1 and 3 collimators are large as possible, then choosing the stage 2 collimator to maximize tube output while maintaining a reasonable dead time.

## Conclusion

In order to fully optimize a PEDXRF system, there are a number of factors to consider. Firstly, the choice of secondary target and tube potential must match the element(s) of interest in the sample, keeping in mind the secondary target thickness. Next, the optimal collimation should be chosen, allowing for maximum tube current.

This work looked at only a single element (Fe) present in the sample, however it is reasonable to conclude that the results could be extended to other analytes, and multi-elemental samples. As long as the fluorescent lines from the secondary target are above the Photoelectric absorption edge of the element(s) to be measured, the work

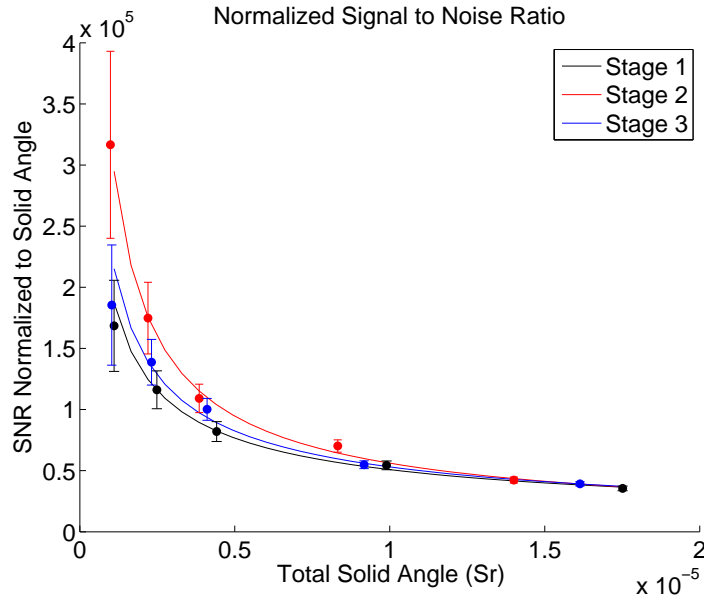


Figure 4.26: The SNR divided by total solid angle, as a function of total solid angle, changing collimators in one stage at a time. Only the experimental data is shown.

shown should be valid. The secondary target thickness only modifies the secondary spectrum, which should behave the same regardless of the element(s) present in the sample, provided it has enough energy to cause fluorescence. However, further work done on a multi-elemental sample would allow for a more concrete conclusion to be drawn.

The optimal secondary target thickness (for a sample containing Fe) was determined to be  $25\mu m$  for Cu,  $50\mu m$  for Mo, and  $90\mu m$  for Sn. When looking at the Cu secondary target, the optimal thickness was found to be independent of the tube potential, but an optimal potential existed. As above, this conclusion is expected to extend to all secondary target materials. The optimal potential for the Cu secondary target had a mean photon energy just above the absorption edge of the secondary target, leading to the maximum probability for secondary target fluorescence.

Choosing the optimal secondary target thickness can provide an increase in SNR

of 6 – 17%, depending on the configuration chosen, when compared to the ‘infinitely thick’ SNR. These increases should directly correlate to decreases in MDLs, according to Equation 4.8.

After secondary target and tube potential considerations, the optimal collimation must be examined. It was found that having the largest possible stage 1 and 3 collimators yield the highest SNR, while the stage 2 collimator should be chosen to allow for maximum tube current. Since the stage 2 collimator is placed between the secondary target and sample, experiments with small sized samples also benefit from having this smaller stage 2 collimator. Altogether, these factors will improve MDLs for a PEDXRF system, allowing for trace elements in lower concentrations to be examined, and data acquisition times to be decreased.

Taking these findings into account, the final PEDXRF design has a stage two collimator that provides a spot size equivalent to the sample size, as shown in Figure 4.27. The stage one and three collimators were made as large as the secondary target and detector window respectively, providing the optimal SNR geometrically. In all measurements, the optimally thick secondary target is used, with the optimal x-ray tube potential, providing the best SNR possible. While this may increase data collection time, it does provide the lowest MDLs. If data acquisition takes too long, then a stronger x-ray tube, or a larger detector can be employed, without sacrificing the benefits gained by using the optimal PEDXRF characteristics.

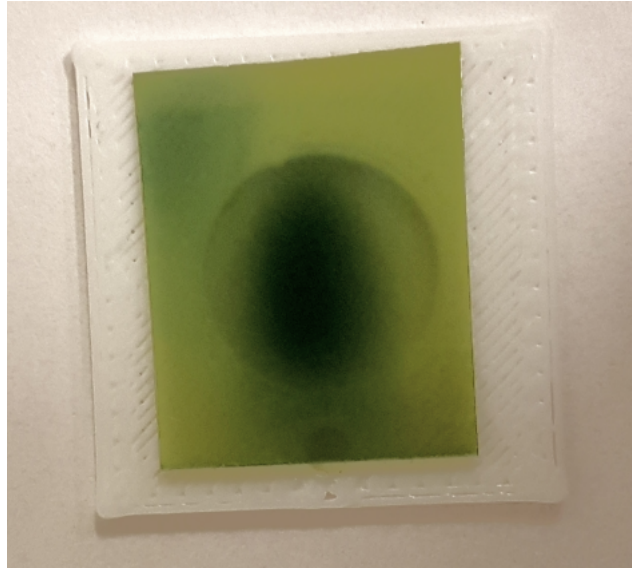


Figure 4.27: A picture of radiochromic x-ray film, showing the x-ray spot size on the sample holder.

## 4.2 EDXRD Optimization

The optimization process for the EDXRD system was much more straightforward than the PEDXRF system. While there may be room for improvement on the current EDXRD design, it has been used successfully in previous works<sup>[28]</sup>. As such, the only optimizations considered were choosing the correct angle and tube voltage configurations for biological samples, as well as the detector choice.

With the addition of the  $2mm$  aluminum filter, which was used to remove low energy bremsstrahlung and tungsten  $L$  lines from the primary spectrum, the effective x-ray energies that can be produced lie between  $15keV$  and  $160keV$ . Removing the fluorescence lines from the primary x-ray beam decreased detector dead time, allowing higher voltage and current settings to be used, as well as allowing for easier data interpretation, due to the lack of fluorescence in the measured spectrum. In order to avoid the same problem with  $K$  lines, the diffraction angle is often chosen

so that the useful data is below the  $K$  fluorescence peaks.

The angles available in the EDXRD angle block are from  $3^\circ - 12^\circ$ . According to Equation 2.16, the possible momentum transfers that could be excited using this system are between  $0.3nm^{-1}$  and  $13.5nm^{-1}$ . Table 4.4 lists the momentum transfers possible for each angle, as well as the momentum transfer of the tungsten  $K_\alpha$  fluorescence. From Table 4.4, it would appear that a  $3^\circ$  diffraction angle would be sufficient for biological sample measurement, however, this places the  $K$  lines from tungsten on top of several tissue diffraction peaks, which can lead to difficulty in extracting information from collected spectra. Instead, a detector was fixed with a  $6^\circ$  diffraction angle, to provide a fluorescence free range of momentum transfers between  $0.63nm^{-1} - 2.53nm^{-1}$ , encompassing most of the useful data range.

Table 4.4: A table showing the possible momentum transfer values available at each angle, as well as the momentum transfer value where the tungsten  $K_\alpha$  line occurs.

Angle	Momentum Transfer Range ( $nm^{-1}$ )	Tungsten $K_\alpha$ Momentum Transfer ( $nm^{-1}$ )
$3^\circ$	0.32 – 3.34	1.27
$4^\circ$	0.42 – 4.50	1.69
$5^\circ$	0.53 – 5.63	2.11
$6^\circ$	0.63 – 6.75	2.53
$7^\circ$	0.74 – 7.87	2.95
$8^\circ$	0.84 – 9.00	3.37
$9^\circ$	0.95 – 10.1	3.79
$10^\circ$	1.05 – 11.2	4.21
$11^\circ$	1.16 – 12.4	4.64
$12^\circ$	1.26 – 13.5	5.05

While a single fixed angle was determined optimal for most biological tissue samples, it could be useful to utilize the other angles available on the EDXRD angle block. It was decided to improve functionality, a second diffraction detector can be added on

the odd angle half of the EDXRD angle block (see Figure 3.13). This detector is not firmly fixed in place, but can be quickly moved from one angle to another, providing access to all odd diffraction angles. The adjustability of this second detector makes it more difficult to ensure proper placement. As such, extra care and consideration must be taken when aligning this detector with the EDXRD angle block. Additionally, for a single experiment, this detector should remain fixed, as slight movements can affect the accuracy of results.

For the EDXRD setup, the detector choice was simple, as HPGe detectors have a high efficiency in this energy range, and have been used extensively as EDXRD detectors. These detectors have a near 100% efficiency in the  $10\text{keV} - 160\text{keV}$  energy range, making them ideal for this experiment. They also have an energy resolution smaller than the diffraction peak widths, meaning they do not appreciably alter peak widths. The diffraction detectors were outfitted with slit collimators with widths twice as large as the EDXRD angle block slit widths. These collimators help to reduce scatter from above and below the EDXRD angle block from entering the detectors,

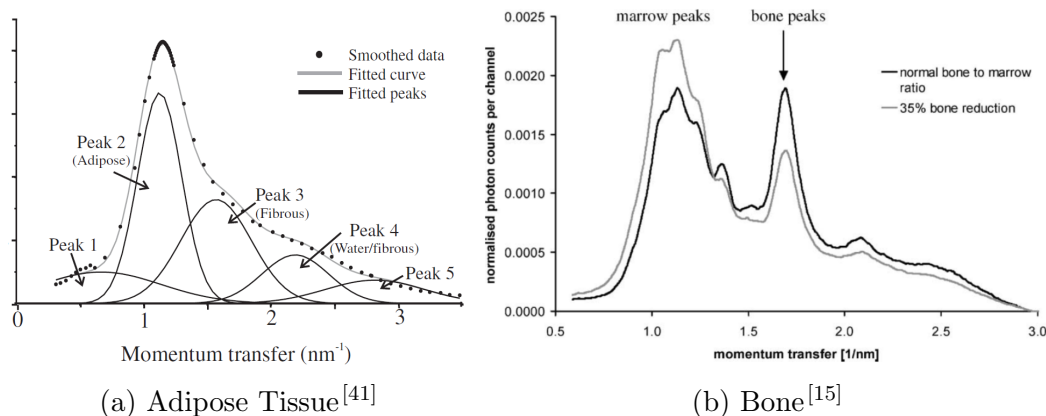


Figure 4.28: The momentum transfer ranges of some common biological samples. It can be seen that most data lies between  $0.5\text{nm}^{-1}$  and  $3\text{nm}^{-1}$ .

thus lowering background levels in measured spectra.

# Chapter 5

## Application Testing

After completing the design and optimization of the combined PEDXRF and EDXRD system, it was necessary to test it, in order to ensure that the system functions as expected. This chapter discusses a series of experiments performed on the final PEDXRF and EDXRD system, as described at the end of Chapter 3, taking into account any optimizations made in Chapter 4, unless otherwise stated. This chapter highlights some key features of the combined spectrometer, illustrates its uses, and proves its effectiveness by comparing it to other spectrometers capable of performing the same measurements.

The purpose of developing this system was to use it to examine and classify various biological tissues, so the experiments performed all relate to classifying biological samples. Thus, this focuses on evaluating the analytical performance of the developed system in contrast to other similar systems. This chapter provides evidence that the construction and optimization of this combined spectrometer was worthwhile, and that it will prove to be a useful tool for future medical physics experiments. All PEDXRF measurements discussed in this chapter were taken using optimally thick

secondary targets ( $25.4\mu m$  for copper and zinc,  $50.8\mu m$  for molybdenum).

## 5.1 Reproducibility

One of the most important aspects of any piece of scientific equipment is the reproducibility of measurements. It is extremely important to determine the precision and accuracy of any new equipment, otherwise researchers will not be confident that reliable measurements can be made.

A simple experiment was designed to determine the precision of the combined spectrometer. A single sample was measured using the same parameters on ten different days, returning all equipment to a resting state between each measurement. This involved removing the sample, placing it in the freezer, and powering off the x-ray tube and detector electronics. The results from each day were then analysed to determine that the system produces the same result reliably.

For the PEDXRF spectrometer, the sample to be measured was a standard reference material LUTS-1<sup>[42]</sup>, purchased from the National Research Council Canada. LUTS-1 is a sample of non-defatted lobster hepatopancreas, containing trace elements in the concentration range expected for biological samples. This standard also has a similar density to soft tissue samples, making it a suitable surrogate for determining measurement reproducibility. Table 5.1 shows the certified concentrations of key elements found in LUTS-1.

The standard reference sample was measured on the PEDXRF system, with the x-ray tube set to  $50kV$  and  $25mA$ , using a molybdenum secondary target, measured for  $10min$ . The measurement was taken on ten different days, removing the sample from a  $-70^{\circ}C$  freezer each day. The secondary target was also removed and re-inserted,

Table 5.1: A table showing the certified values of trace elements found in the LUTS-1 standard reference material<sup>[42]</sup>. Any element not listed will be undetectable with the current PEDXRF setup.

<b>Element</b>	<b>Certified Value (<math>\mu g/g</math>)</b>	<b><math>K_\alpha/K_\beta</math> Energy (<math>keV</math>)</b>
<b>Potassium</b>	$948 \pm 72$	3.3 / 3.6
<b>Calcium</b>	$203 \pm 33$	3.7 / 4.0
<b>Iron</b>	$11.6 \pm 0.9$	6.4 / 7.1
<b>Copper</b>	$15.9 \pm 1.2$	8.1 / 8.9
<b>Zinc</b>	$12.4 \pm 0.8$	8.6 / 9.6

to determine that secondary target placement was repeatable. Figure 5.1, shows a measured spectrum of the standard.

As seen from Figure 5.1, the  $K_\alpha$  peaks of the five elements of interest can be clearly distinguished, as well as the argon  $K_\alpha$  peak at  $3.0keV$ , a titanium  $K_\alpha$  peak at  $4.5keV$ , a nickel  $K_\alpha$  peak at  $7.5keV$ , and a lead  $L$  peak at  $9.2keV$ . The full spectrum also shows the other lead  $L$  peaks, and the coherent and Compton scatter peaks from the molybdenum secondary target. As before, the lead and argon come from shielding and the air respectively. The titanium comes from the colourant in the PLA used to 3D print the PEDXRF block, and is present in all measurements. Similarly, the nickel comes from the head of the SDD detector, and is also present in all measurements, making it impossible to measure any nickel present in biological samples.

The collected spectra were fit using an inverse variance weighted, non-linear least-squares method, determining the area of each peak of interest. These areas were normalized to the argon peak, which accounts for minor variances x-ray tube output. The normalized counts for each element are shown in Figure 5.2 and Figure 5.3.

In order to quantify the reliability of this system, the normalized counts for each

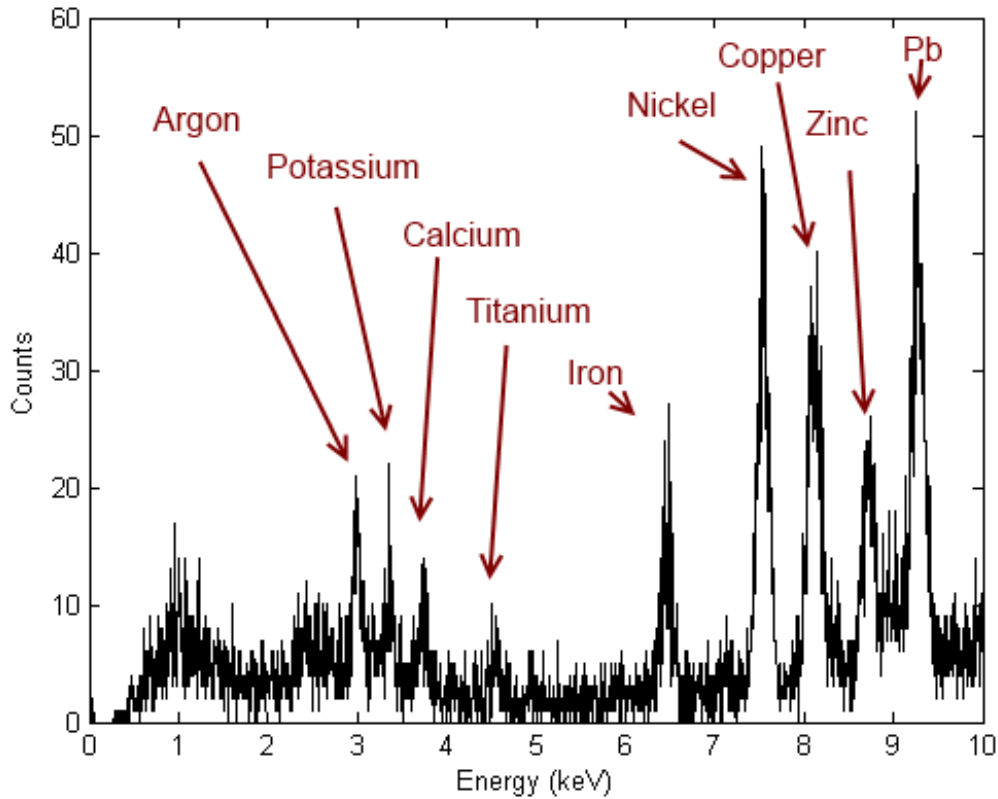


Figure 5.1: A measured spectrum from the LUTS-1 standard reference material. The region between 0 – 10keV contains the elements of interest.

day were averaged, and using the variances due to fitting and Poisson counting statistics, an uncertainty in the mean was calculated using error propagation rules. Additionally, the standard deviation for each element was also calculated. Table 5.2 displays the statistical results for each test. Since the standard deviation for each element falls below the calculated uncertainty, the counting statistics and fitting error dominate any variabilities introduced by changing samples, proving that the PEDXRF system produces reliable results.

Looking to the EDXRD spectrometer, a similar experiment was designed. In this

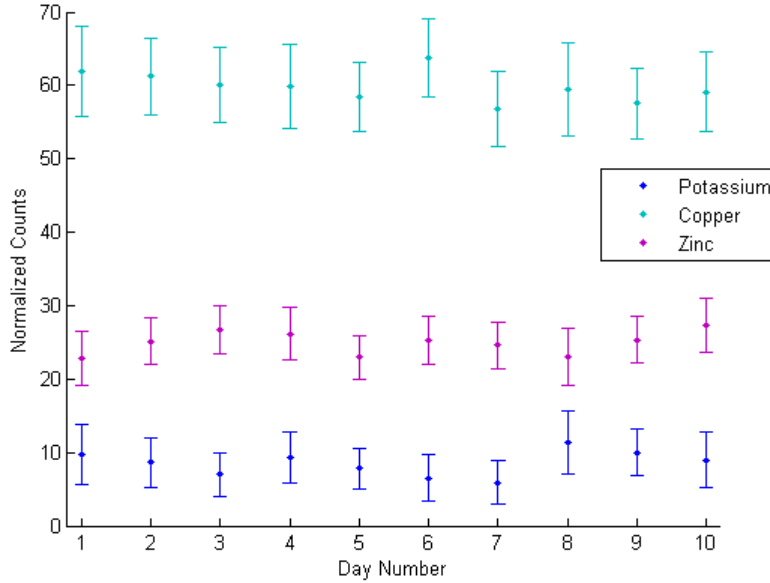


Figure 5.2: A visual representation of the results obtained from the reproducibility study. The x-axis represents which day the sample was measured, with each element having a different color as shown in the legend. This data is split into two graphs to help visualize overlapping elements.

Table 5.2: Statistical results of the PEDXRF reproducibility study.

Element	Average Normalized Counts	Standard Deviation
Potassium	$8 \pm 3$	1.6
Calcium	$7 \pm 3$	1.1
Iron	$15 \pm 3$	1.4
Copper	$60 \pm 5$	2.0
Zinc	$25 \pm 3$	1.5

case, the sample was a breast tissue sample with invasive ductal carcinoma. This sample contains the structures expected from biological samples that will be run on the EDXRD system, making it suitable for the reproducibility measurement. The sample was run with the x-ray tube set to  $80kV$  and  $8mA$ , with a diffraction angle of  $6^\circ$ , for  $30min$ . Once again, the sample was removed from a freezer before the

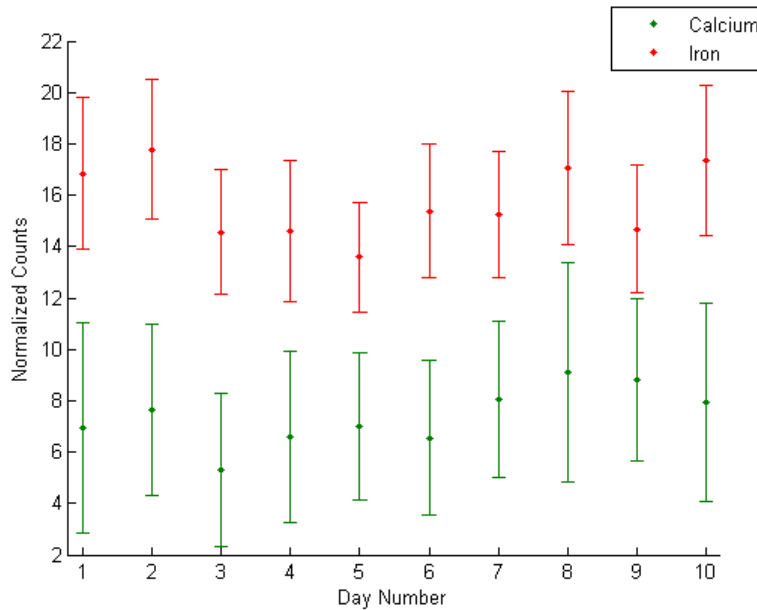


Figure 5.3: A visual representation of the results obtained from the reproducibility study. The x-axis represents which day the sample was measured, with each element having a different color as shown in the legend. This data is split into two graphs to help visualize overlapping elements.

measurement each day, and the equipment was returned to a resting state between each measurement. A sample spectrum is shown in Figure 5.4. The adipose, fibrous, and water peaks are visible, as well as the  $K$  fluorescence peaks from the tungsten tube.

Following the fitting technique shown in Figure 4.28<sup>[41]</sup>, the collected spectra were fitted. The counts in the adipose, fibrous and water peaks were normalized to total counts, which accounts for any variances in x-ray tube output. Again, the parameters of interest (adipose, fibrous, and water peak count) are plotted in Figure 5.5, while Table 5.3 outlines the statistical results for the experiment.

Looking at Figure 5.5 and Table 5.3, it can be seen that the EDXRD results are also very reproducible, having a standard deviation below the uncertainty introduced

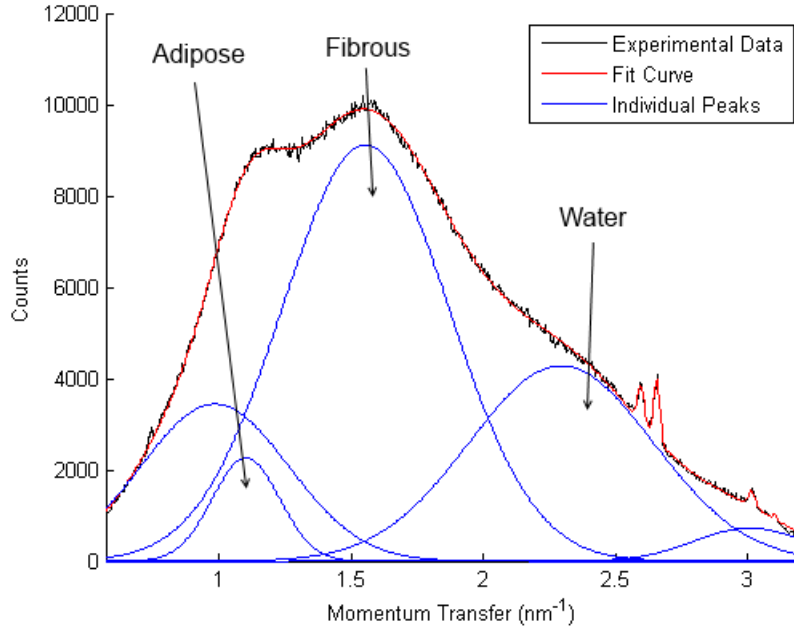


Figure 5.4: A measured spectrum from the invasive ductal carcinoma sample.

Table 5.3: Statistical results of the EDXRD reproducibility study.

Peak	Average Normalized Counts	Standard Deviation
<b>Adipose</b>	$0.033 \pm 0.007$	0.0015
<b>Fibrous</b>	$0.80 \pm 0.03$	0.008
<b>Water</b>	$0.154 \pm 0.011$	0.003

by counting statistics and curve fitting.

## 5.2 Minimum Detection Limits

With reproducibility tests for both the PEDXRF and EDXRD spectrometers completed, the next experiment performed was to determine the MDLs of key elements on the PEDXRF system. Several different techniques exist for determining the MDLs of a PEDXRF system, all of which require a sample with a known concentration of

trace elements. The simplest technique, shown in Equation 5.1, requires only a single data point<sup>[6]</sup>. The background area is calculated as the area under the curve that doesn't belong to the fluorescence peak. Figure 5.6 shows an example peak fit with background.

$$MDL = 3 * Concentration * \frac{\sqrt{Background Area}}{Peak Area} \quad (5.1)$$

Using this technique, the MDL can be determined for any element present in a sample with a known concentration. By measuring the LUTS-1 sample, which has known concentrations shown in Table 5.1, MDLs could be calculated for the 5 measurable elements. The sample was run for 10min, using the molybdenum secondary

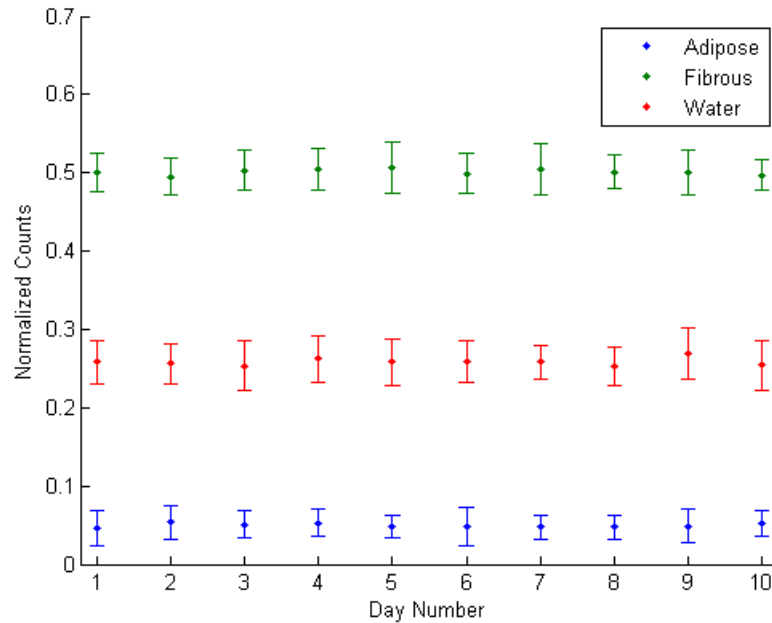


Figure 5.5: The normalized adipose, fibrous, and water peak areas, for the same sample taken on ten separate days. The x-axis represents which day the sample was measured, with each peak having a different color as shown in the legend.

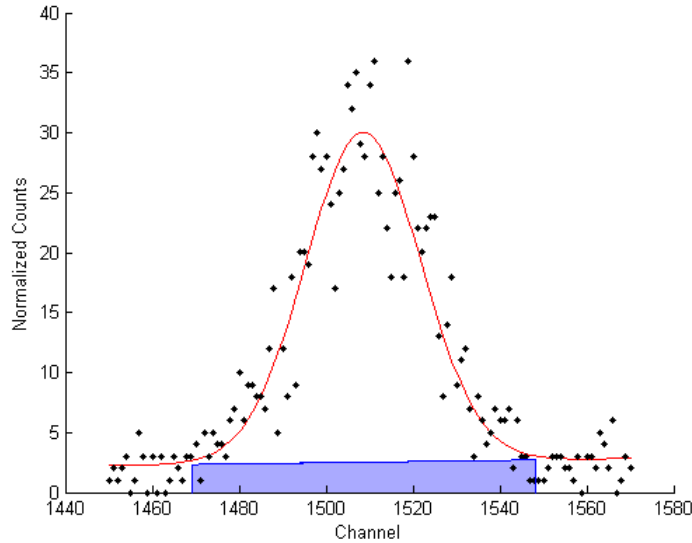


Figure 5.6: A peak fit with a Gaussian and linear background. The area of the Gaussian is taken to be the peak area, and the area shown in blue (linear background within  $\pm 3\sigma$  of the centroid) is taken to be the background

target, and x-ray tube settings  $50kV$  and  $25mA$ . Table 5.4 shows the result of this test, comparing to the results found by several other researchers using PEDXRF systems. It can be seen that the PEDXRF spectrometer operates well, providing MDLs equivalent or below other available systems for the elements measured. It should be noted that the experiments listed used different standard materials and measurement parameters, which may contribute to the large variation of MDLs from other PEDXRF spectrometers.

One limitation of the single measurement MDL calculation is that it doesn't consider any fluorescence counts that may come from a background measurement. In order to address this, another common method of calculating MDLs was employed. This technique requires a series of samples with known concentrations to be measured. Once measured a line of best fit is calculated, relating the peak area to the

Table 5.4: MDLs for the PEDXRF using the single measurement technique. All values are given in  $\mu\text{g/g}$ .

Element	MDL	Kramar <i>et.al.</i> <sup>[6]</sup>	Pessanha <i>et.al.</i> <sup>[8]</sup>	Zhan <i>et.al.</i> <sup>[10]</sup>
<b>Potassium</b>	40	73	47	10
<b>Calcium</b>	31	60	35	11
<b>Iron</b>	1.6	7	2	5.0
<b>Copper</b>	0.9	1.3	1	0.9
<b>Zinc</b>	1.3	1.26	1	1.0

concentration<sup>[43,44]</sup>. If the line of best fit is  $y = mx + b$ , then the calculation of MDL using this technique is shown Equation 5.2.

$$MDL = 2 * \sqrt{\left(\frac{\sigma_y}{m}\right)^2 + \left(\frac{\sigma_m(y-b)}{m^2}\right)^2 + \left(\frac{\sigma_b}{m}\right)^2 + 2\left(\frac{y-b}{m}\right)\left(\frac{\sigma_{mb}}{m}\right)^2} \quad (5.2)$$

Where:

$\sigma_i$  is the standard deviation of coefficient  $i$

$\sigma_{ij}$  is the covariance between coefficients  $i$  and  $j$

It should be noted that the first technique for determining MDLs can be derived from Equation 5.2 by assuming the uncertainties in the concentration and slope are negligible, with the minor difference that Equation 5.1 is generally calculated as  $3 * \sigma$ , while Equation 5.2 generally uses  $2 * \sigma$ . Regardless, the two results are expected to be similar, unless the extra terms present in Equation 5.2 are determined to be non-negligible.

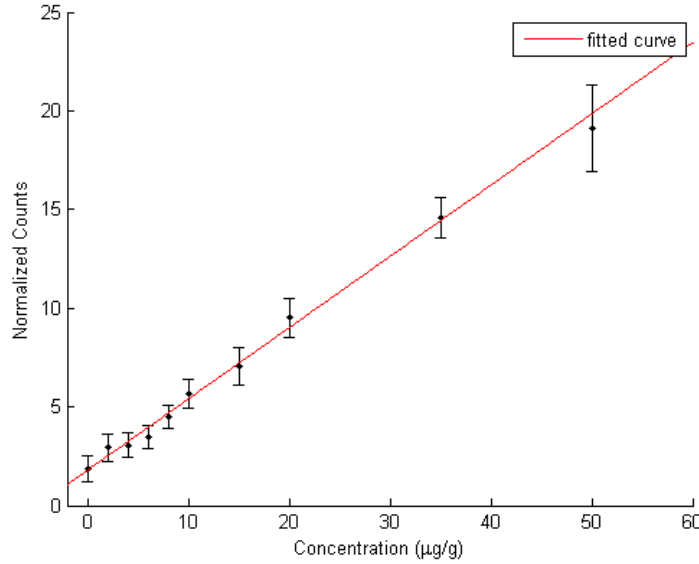
A convenient way to determine the MDL this way is to make a series of calibration phantoms, with known concentrations. These calibration phantoms can then be used to calculate both an MDL, and a calibration line, which can be used to convert peak

areas into concentration values.

It was decided that calibration phantoms would be made for three trace elements of great importance in biological samples, iron, copper, and zinc<sup>[2,3]</sup>. The phantoms were made from distilled water and various amounts of iron, copper, and zinc stock solutions purchased from Ultra Scientific, specifically ULTRAGrade solutions ICP-026, ICP-029, and ICP-030 respectively. The stock solutions contained  $1000\mu\text{g/g}$  of analyte, which was then diluted using a micropipette into solutions containing 0, 2, 4, 6, 8, 10, 15, 20, 35, and  $50\mu\text{g/g}$  respectively. These solutions were then injected into an empty sample holder using a small needle, relying on surface tension to keep the liquid from leaking from the holder. If a leak did occur during measurement, the sample was made again and remeasured.

For the copper and zinc calibration samples, only the molybdenum secondary target was used, but for the iron calibration samples, a molybdenum, zinc, and copper secondary target was used. All measurements were for  $10\text{min}$ , with the x-ray tube set to  $50\text{kV}$  and  $25\text{mA}$ . Figure 5.7 shows the line of best fit for the iron calibration samples, Figure 5.8 for copper, and Figure 5.9 for zinc.

The MDLs calculated from these lines are shown in Table 5.5. When compared to the MDLs found using the single measurement method, it is evident that these MDLs are much larger. This is likely caused by this technique taking into account the value of a zero concentration measurement, which was non-zero in all cases. It is worth noting that changing the secondary target to be closer to the analyte on the periodic table yielded improved MDLs, as expected. This means that when possible, it is best to use a secondary target whose fluoresced x-rays will be just above the absorption edge of the analyte.

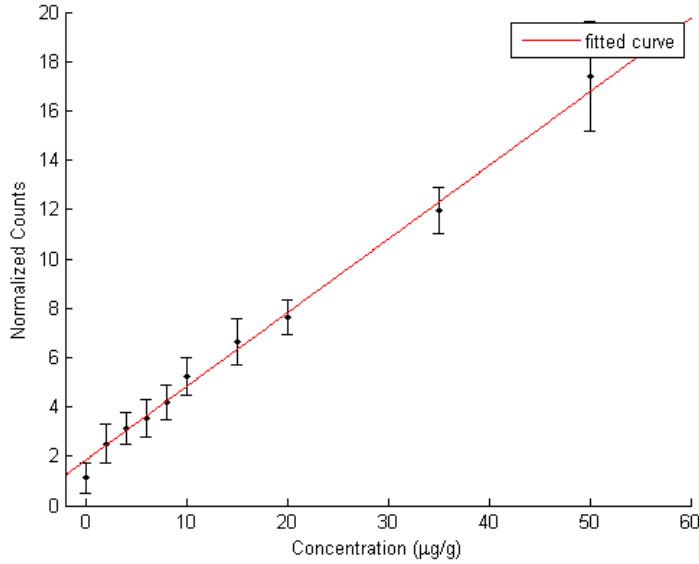


(a) Copper Secondary Target

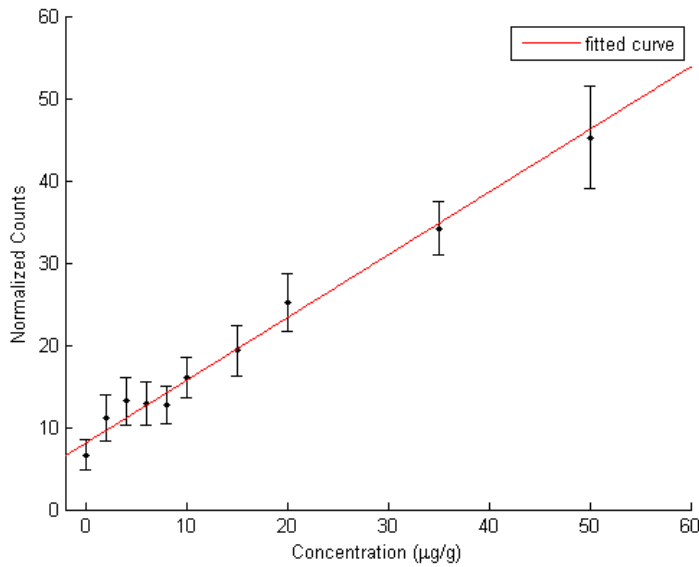
Table 5.5: MDLs for the PEDXRF using the calibration line approach. All values are given in  $\mu g/g$ .

	MDL ( $\mu g/g$ )		
	Iron	Copper	Zinc
<b>Copper Secondary Target</b>	2.8	-	-
<b>Zinc Secondary Target</b>	3.3	-	-
<b>Molybdenum Secondary Target</b>	4.6	4.8	2.3

Now that a calibration line was determined, the accuracy of the PEDXRF system could also be tested, by converting the fluorescence peaks measured from the LUTS-1 standard samples (refer to Figure 5.1) into concentrations, and comparing the measured concentration to the certified value. The average normalized count for iron, copper, and zinc, taken from Table 5.2, was used to calculate the concentration. Table 5.6 summarizes these results. Since all values are equal to the standard reference values within error, it is safe to say that the PEDXRF spectrometer is accurate at measuring iron, copper, and zinc.



(b) Zinc Secondary Target



(c) Molybdenum Secondary Target

Figure 5.7: Lines of best fit made by measuring iron calibration phantoms with various secondary targets.

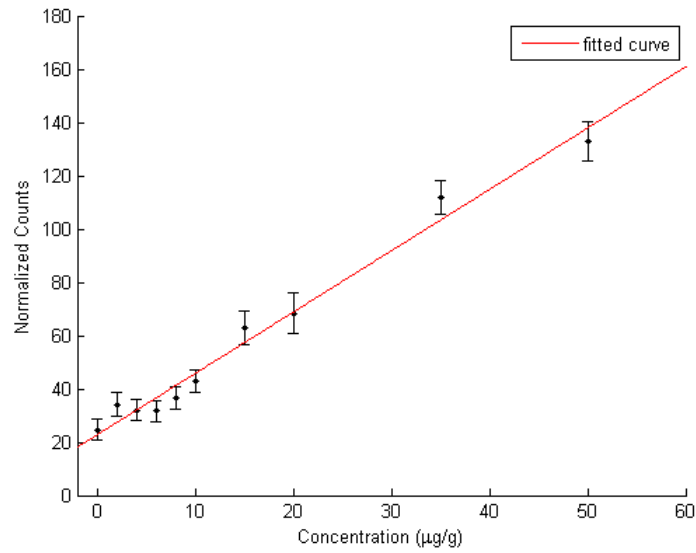


Figure 5.8: A line of best fit made by measuring copper calibration phantoms with a molybdenum secondary target.

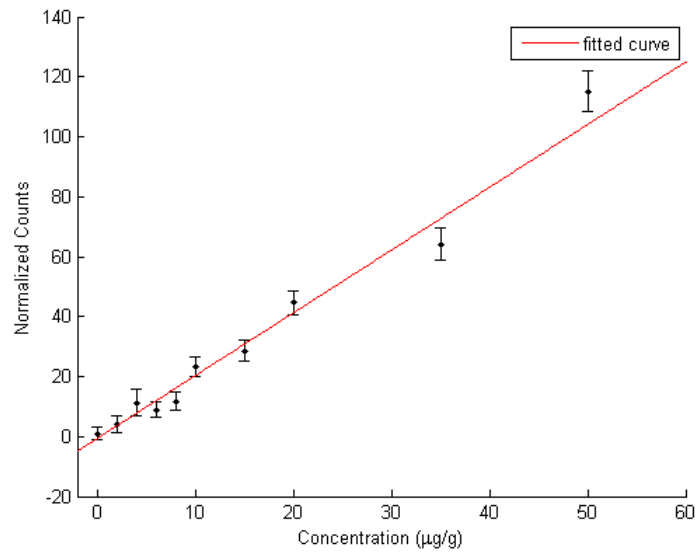


Figure 5.9: A line of best fit made by measuring zinc calibration phantoms with a molybdenum secondary target.

Table 5.6: The concentrations of iron, copper, and zinc in LUTS-1, as measured by the PEDXRF system.

<b>Element</b>	<b>Measured Concentration (<math>\mu g/g</math>)</b>	<b>Certified Value (<math>\mu g/g</math>)</b>
<b>Iron</b>	$10 \pm 3$	$11.6 \pm 0.9$
<b>Copper</b>	$16 \pm 2$	$15.9 \pm 1.2$
<b>Zinc</b>	$12.2 \pm 1.6$	$12.4 \pm 0.8$

### 5.3 Biological Sample Measurements

With knowledge that the combined PEDXRF and EDXRD system is operating as expected, work proceeded with measuring biological samples. Three sets of soft tissues were selected to test different aspects of the system. First, a set of rat organs overloaded with iron was measured to check the effectiveness of measuring a single element by selecting the optimal secondary target and conditions.

The another dataset consisted of cancerous breast tissues. Previous work has shown elemental and structural differences between healthy and cancerous breast tissues<sup>[3,28,41]</sup>. These samples were therefore used to examine one potential use of the of the combined PEDXRF and EDXRD system, as well as highlight its benefits over previous experimental setups.

The last dataset consisted of cancerous lung tissue. Unlike the cancerous breast tissue, previous work did not find any differences between the healthy and cancerous lung tissues<sup>[45]</sup>. Therefore, these samples were selected to determine if the new combined spectrometer could outperform other experimental setups.

### 5.3.1 Rat Organs

The first set of biological tissues measured was a set of rat organs overloaded with iron. The goal was to correlate the iron found in rat skin to the iron stored within critical organs, thus showing that a skin iron measurement may be suitable to act as a surrogate for direct organ measurement in humans. An experiment was designed that overloaded rats with several doses of iron, leading to a wide range of organ iron concentrations. The rats were then sacrificed, the liver, heart, kidney, and skin were harvested and subsequently mounted onto the standard sample holders, ready to be measured.

Since the goal of this experiment was to measure strictly the iron concentration in the organs, only PEDXRF measurements were made. The benefit of looking for only a single element allowed for the measurement parameters to be tailored for exciting that element, showing the usefulness of easily changeable secondary targets. The copper secondary target was the obvious choice, since it provides x-rays close to the iron absorption edge, while being high enough to ensure that the iron peaks don't overlap with the Compton scatter peak. The x-ray tube was set to  $50kV$  and  $25mA$ , which provided a suitable x-ray fluence rate, allowing for results to be collected within  $10min$ . This measurement time was determined experimentally by examining the skin measurements of the control group (which should have the lowest iron concentration), and determining the length of time required to reach 1000 fluorescence counts, leading to a 3% Poisson uncertainty in iron fluorescence peak area.

The rat samples were measured, and the concentration of iron in each organ was found using the calibration lines already produced. Figure 5.10 shows the comparison of liver iron to skin iron, Figure 5.11 for heart, and Figure 5.12 for kidney. The

following figures all contain fitted lines or curves to illustrate the trends found in the study<sup>[46]</sup>, however, it should be noted that these regression results do not include any uncertainties in the skin concentration, and were only included for comparison purposes.

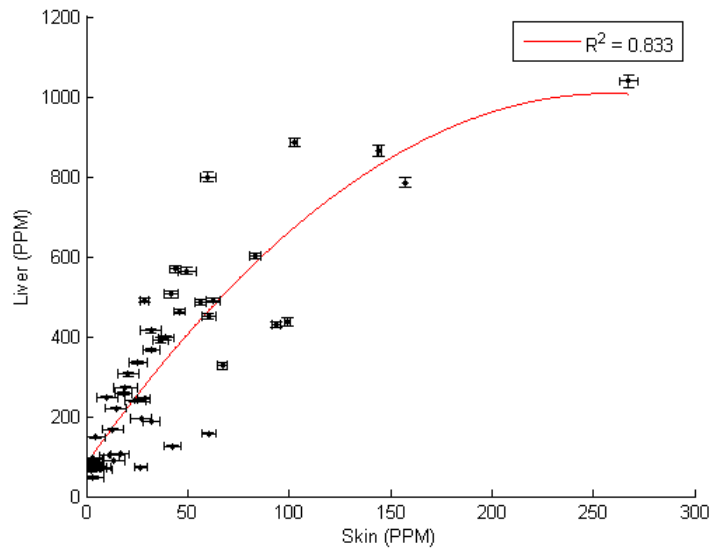


Figure 5.10: A comparison of skin and liver iron concentration in iron overloaded rats. A quadratic curve with  $R^2$  is shown.

Looking at Figure 5.10, it is obvious that the skin iron concentration and liver iron concentration are correlated, following a quadratic trend. Additionally, looking at Figure 5.11 and Figure 5.12, it can be seen that there is a weak correlation between the skin iron concentration and the kidney and heart iron concentration. These results agree with what was found in the study<sup>[46]</sup>; the heart and kidney iron concentrations were weakly correlated with skin iron, and the liver iron concentration was strongly correlated with the skin iron, following a quadratic trend. It was hypothesized that the iron concentration in the liver was saturating due to biological effects at higher dose rates, causing the quadratic trend found in Figure 5.10.

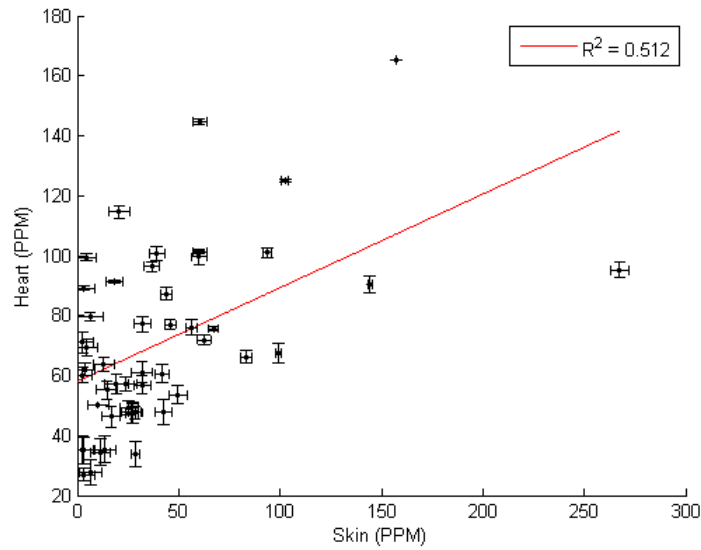


Figure 5.11: A comparison of skin and heart iron concentration in iron overloaded rats. The line of best fit with  $R^2$  is shown.

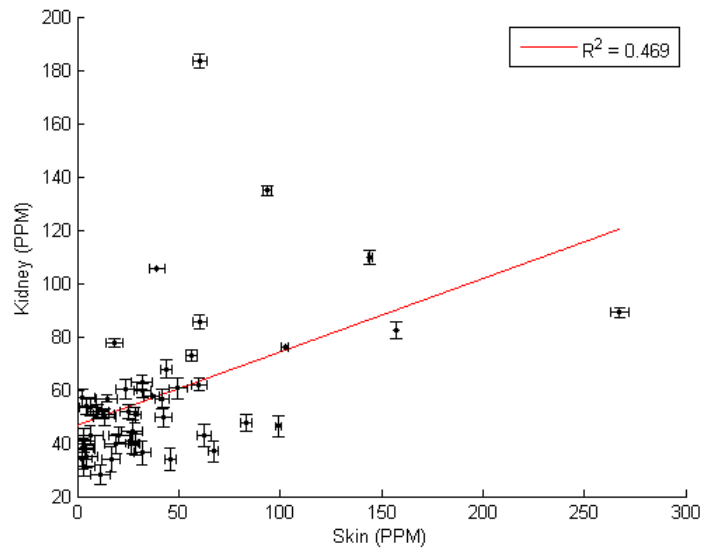


Figure 5.12: A comparison of skin and kidney iron concentration in iron overloaded rats. The line of best fit with  $R^2$  is shown.

Another benefit of measuring the rat organs was that these samples were also measured on two other XRF spectrometers, allowing the results from the PEDXRF system to be compared to two other systems. One of the systems was an XRF spectrometer made by Huber Diffractionstechnik (henceforth referred to as the Huber spectrometer), and has been used in many previous studies<sup>[45,46]</sup>. Figure 5.13 to Figure 5.16 show the comparison of organ iron measurement between the PEDXRF spectrometer, and the Huber spectrometer. While the kidney and heart measurements do not show a strong correlation, the skin and liver measurements show a very good agreement. The differences in measured values may be caused by the spot size difference between the two spectrometers. While the PEDXRF system has an elliptical spot size covering most of the target holder, the Huber system has a small  $2\text{mm} \times 2\text{mm}$  square spot. Fortunately, the skin and liver measurements on both spectrometers agree quite well, suggesting that these samples may have a more uniform iron distribution.

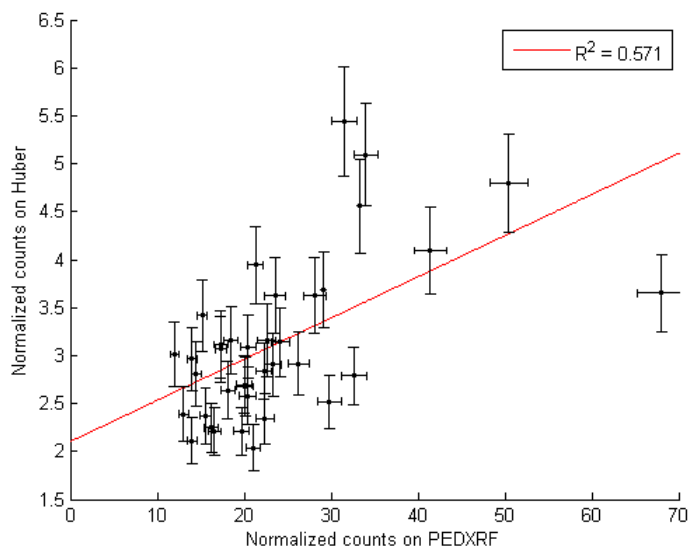


Figure 5.13: A comparison of kidney iron concentration measured with the PEDXRF and Huber spectrometers.

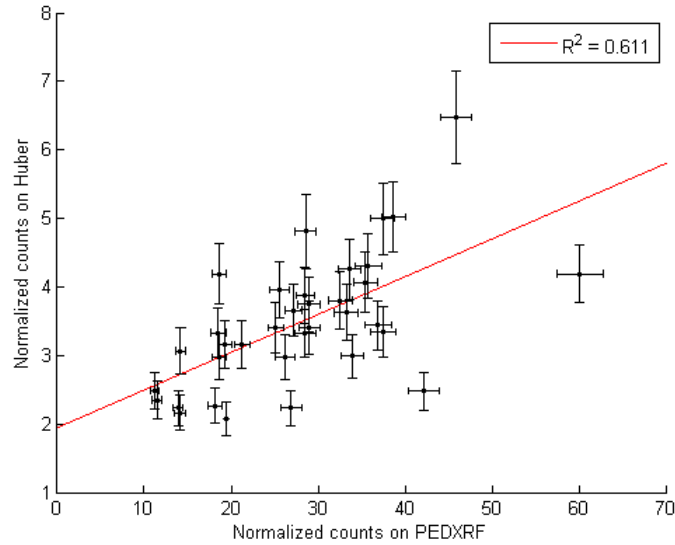


Figure 5.14: A comparison of heart iron concentration measured with the PEDXRF and Huber spectrometers.

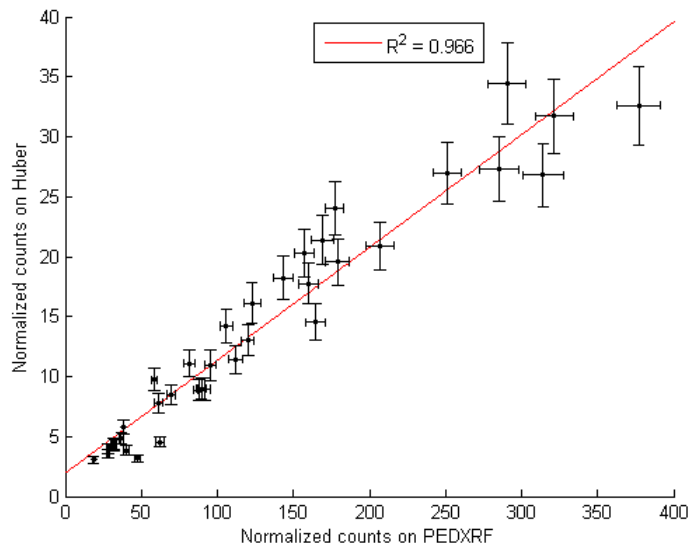


Figure 5.15: A comparison of liver iron concentration measured with the PEDXRF and Huber spectrometers.

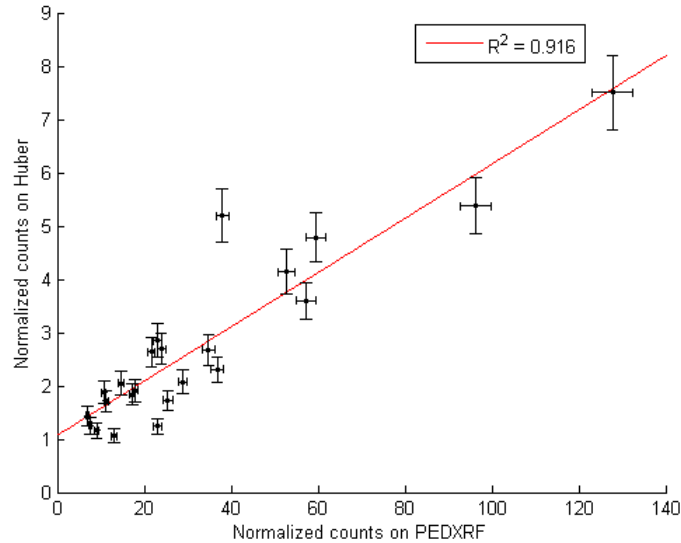


Figure 5.16: A comparison of skin iron concentration measured with the PEDXRF and Huber spectrometers.

Although these figures do show a correlation between samples measured using the PEDXRF and Huber spectrometers, the correlation is being made using counts normalized to the argon fluorescence peak. While this is a valid method to examine whether the two systems give comparable results, it would be interesting to determine whether the two systems provide similar results when comparing concentrations instead of normalized counts. Unfortunately, the detector used in the Huber spectrometer was broken before the rat measurements and calibration lines could be completed, so a direct comparison of concentration values is impossible. However, a cross calibration could be performed, where the calibration and correlation data for one measured dataset is used to calibrate the others. Once the Huber data has been cross calibrated, the correlation measurement can be completed again, and ideally the slope of the line of best fit should be 1.

For the cross calibration, the skin measurement line of best fit was used, since

the skin measurements were quite strongly correlated between the two spectrometers, and the majority of the data fell within the calibrated range. The new calculated slopes were 1.08, 0.80, 1.85, and 1 for heart, kidney, liver, and skin respectively. The skin slope is expected to be 1, verifying the cross calibration was performed correctly. While the heart and kidney calibrations provide slopes close to 1, the liver calibration is almost double the expected value.

There are a few potential explanations for this result, the most likely being differences in the XRF techniques. The Huber spectrometer performs XRF using a monochromated molybdenum target as its source, while the input spectrum from the PEDXRF spectrometer comes from an aluminum filtered tungsten anode tube incident on a copper secondary target. Therefore, it is possible that the two spectrometers may not be calibrated to each other linearly, due to differences in the measurement protocol. It is hypothesized that the results for the heart and kidney provide slopes near 1 because the range of measured values lie close to the range found in the skin, allowing for a linear approximation of the cross calibration to provide acceptable results. When the number of counts far exceeds this range, the cross calibration becomes poor, evident from the slope of 1.85 for the liver measurements.

The other system used to measure the iron overloaded rat samples was a commercial XRF spectrometer, the Innov-X Delta Hand Held XRF DS-4000. Only the skin samples were measured on this spectrometer, and the correlation with the PEDXRF spectrometer is shown in Figure 5.17. Once again, the correlation for the skin measurement is quite strong, proving the effectiveness of the PEDXRF spectrometer. With only a single organ measured on the hand held spectrometer, no cross calibration experiment could be performed.

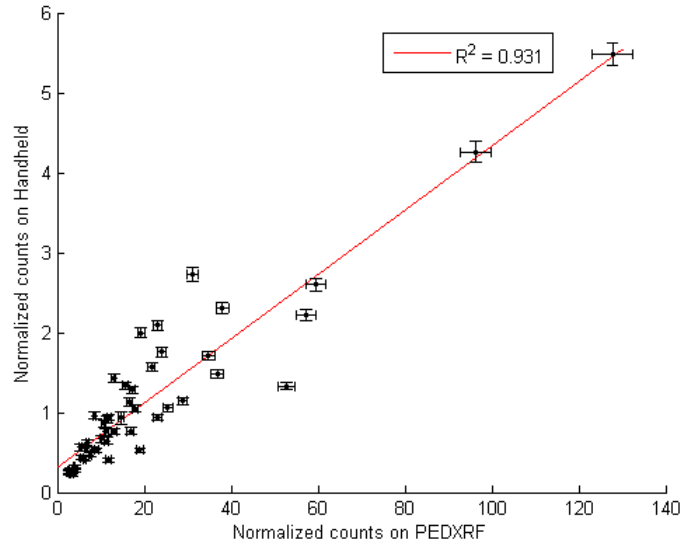


Figure 5.17: A comparison of skin iron concentration measured with the PEDXRF and Innov-X hand held spectrometers.

The agreement between the measured iron concentrations and what was found in the study provides strong evidence that the PEDXRF spectrometer is functioning properly, and yielding useful results. The fact that the results were similar when measured on two other XRF spectrometers ensures that the PEDXRF setup is providing accurate results which are comparable to those obtained on the other two spectrometers. It is worth noting that due to the ability to switch the secondary target, and use a much higher powered x-ray tube, the data acquisition time on the PEDXRF, providing a similar quality of results, was much lower than that of the Huber spectrometer, and similar to that of the commercial hand held device. This fact helps prove that the PEDXRF spectrometer will be a useful tool in future research experiments involving biological tissues.

### 5.3.2 Breast Tissue

The next sets of tissue measured were two different sets of tumourous breast tissue. The first dataset measured consisted of 57 matched pairs of invasive ductal carcinoma. These samples were taken directly after being surgically removed, and no chemical processing was performed on them, apart from being put into a  $-70^{\circ}\text{C}$  freezer. From other previous works<sup>[3,28,41]</sup>, it was determined that the freezing and thawing process does not alter XRF or XRD results, however, if the samples are not given time to thaw, the XRD results will show an ice peak.

This sample set was measured using the final EDXRD setup, and the fourth PEDXRF setup, which was the most recent iteration at the time. The most significant difference between the final PEDXRF setup and the fourth setup was the detector used. While both setups used an SDD detector, the fourth setup used a Bruker AXS XFlash 4010, with a  $7\text{mm}^2$  active area, whereas the final PEDXRF setup used a Ketek AXAS-M1-H150, a newer SDD with an active area of  $150\text{mm}^2$ . As a result, the data collection time on the fourth PEDXRF setup was much longer than that of the final PEDXRF setup.

The goal of these measurements was to mimic previous studies that found significant elemental and structural differences between the cancerous and healthy tissues<sup>[3,28,41]</sup>. The final goal of the experiment was to perform Principal Component Analysis (PCA) on the measured data, allowing a classification model to be made. After the measurements were completed, the samples were sent for histology, which determined some samples thought to be healthy tissue contained cancer, and *vice versa*. After properly classifying each sample, and removing necrotic samples, the dataset was reduced to 52 healthy tissue samples, and 48 cancerous samples.

It was decided that a  $30\text{min}$  data collection time would be used for this experiment, for both the PEDXRF and EDXRD systems. This collection time yielded results for the PEDXRF that had at least 1000 counts in the fluorescence peak, resulting in a 3% error due to Poisson statistics. This measurement time was also used for the EDXRD system, although it ended up being unnecessarily long, as the peak areas were well over  $10^5$  counts. For the PEDXRF measurements, a molybdenum secondary target was employed, with x-ray tube settings of  $50\text{kV}$  and  $25\text{mA}$ . For the EDXRD measurements, the tube settings were  $80\text{kV}$  and  $8\text{mA}$ , with a diffraction angle of  $6^\circ$ .

After both the XRF and XRD measurements were performed on all the samples, the areas of elemental and structural peaks were examined for differences between the healthy and cancerous tissue groups. Figure 5.18 shows the spectra for a normal tissue and its matched tumour pair, showing differences in the potassium, iron and zinc fluorescence peaks.

On a sample to sample basis, the differences can vary greatly. Rather than base a model off of individual samples, it was decided to examine the distributions of the entire normal and tumorous groups. Figure 5.19 and Figure 5.20 show the measured distributions for copper and zinc respectively in the cancerous and healthy tissues.

In order to produce a model to classify unknown breast tissue samples as normal or cancerous, expected distributions of several factors can be used. This approach is therefore interested in looking at how the population distribution varies in order to produce a predictive model. To determine which measured values are of importance, it is required to determine whether there is a statistical significance between the population distributions for the normal and cancerous tissues. This is accomplished by first using a Kolmogorov-Smirnov test, which determines whether or not the group

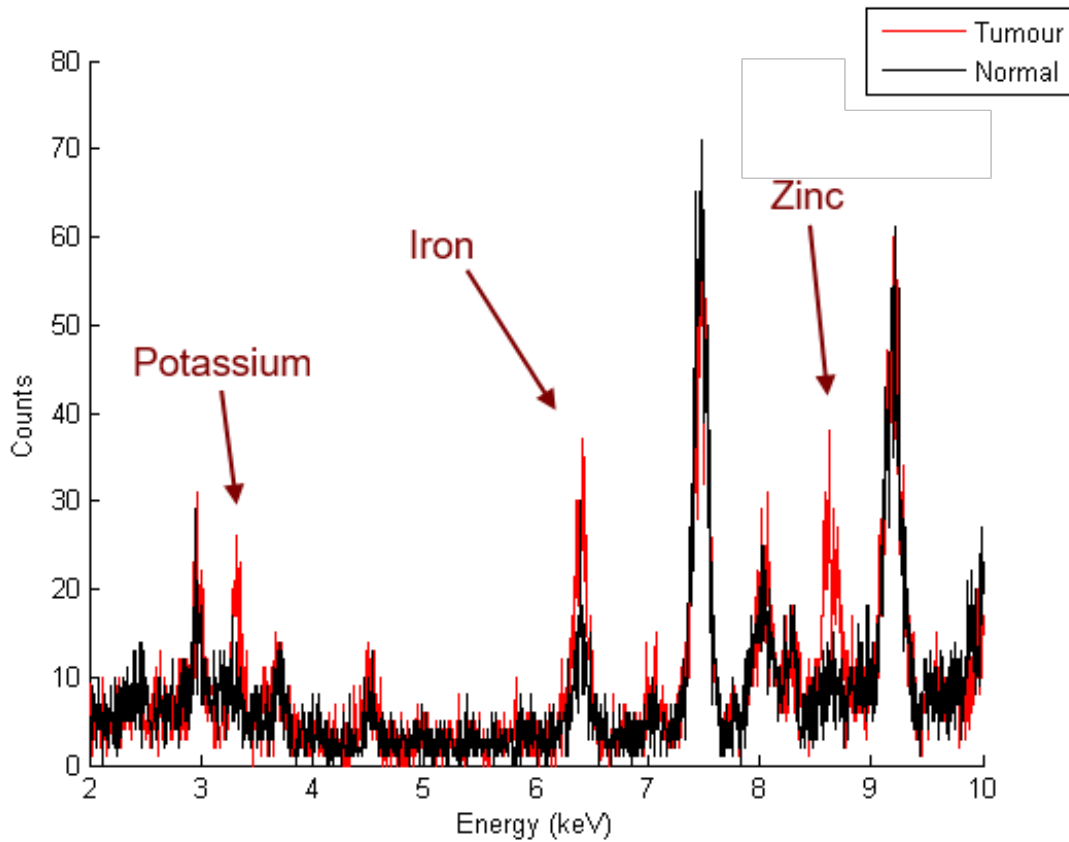


Figure 5.18: The measured spectra of a normal tissue and its matched tumour tissue, showing notable differences in the potassium, iron and zinc fluorescence peaks. Labels for the other fluorescence peaks can be found in Figure 5.1.

is normally distributed. Then, if both distributions are determined to be normal, a two sample t-test can be used to determine if the two distributions differ statistically. However, if one or both of the groups are not normally distributed, then a Wilcoxon ranksum test is employed to determine if two groups are statistically different. Both the two sample t-test and Wilcoxon ranksum test can be used to determine a p-value, which can be used to determine whether the groups are similar (like the copper distribution seen in Figure 5.19), or statistically different (as seen in the zinc distribution shown in Figure 5.20).

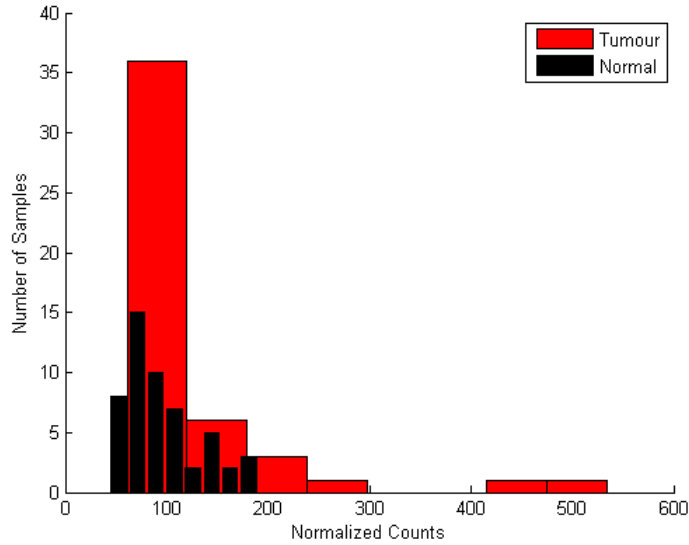


Figure 5.19: A histogram showing the distribution of copper in normal and cancerous breast samples. It can be seen that most of the data overlaps.

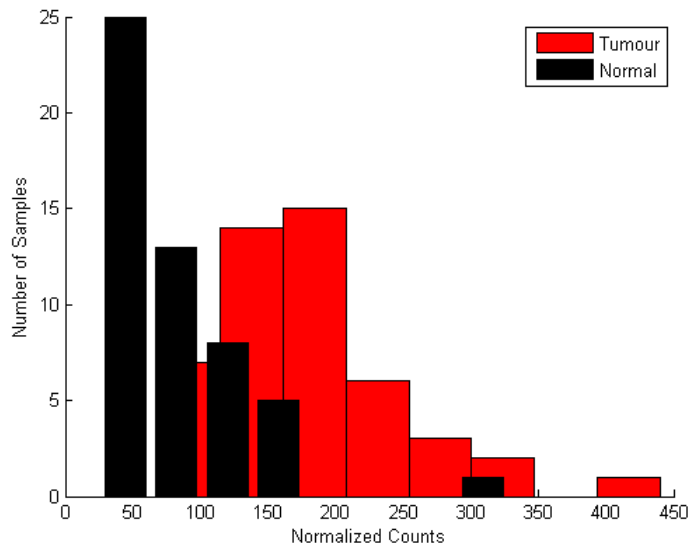


Figure 5.20: A histogram showing the distribution of zinc in normal and cancerous breast samples. It can be seen that only a small portion of the data overlaps.

After the completion of this analysis, it was found that there are several elemental and structural components that differ between the two groups. Many of the results agreed with previous work done by M. J. Farquharson *et. al.*<sup>[3]</sup>, however two elements (calcium and rubidium) showed significant differences in their distributions, which was not discovered previously, warranting further investigation. Additionally, the copper distributions were determined to be statistically similar, which disagrees with what was found. However, the previous study<sup>[3]</sup> found that the difference was very small, on the order of a single  $\mu\text{g}/\text{g}$ , which falls below the MDL for copper for the PEDXRF system. All the EDXRD results agreed with the literature. Table 5.7 summarizes the results found.

Table 5.7: An exhaustive list of all measured elemental and structural components of the healthy and cancerous breast tissues, and whether or not the two population distributions were similar.

<b>Component</b>	<b>Similarity</b>	<b>P-Value</b>
<b>Phosphorus</b>	Same	—
<b>Sulphur</b>	Same	—
<b>Chlorine</b>	Same	—
<b>Potassium</b>	Different	$2 * 10^{-6}$
<b>Calcium</b>	Different	$1 * 10^{-4}$
<b>Iron</b>	Different	$1 * 10^{-2}$
<b>Copper</b>	Same	—
<b>Zinc</b>	Different	$7 * 10^{-6}$
<b>Bromine</b>	Same	—
<b>Rubidium</b>	Different	$2 * 10^{-6}$
<b>Adipose Content</b>	Different	$3 * 10^{-12}$
<b>Fibrous Content</b>	Different	$4 * 10^{-9}$
<b>Water Content</b>	Same	—

Although the population distributions may be statistically different, in general they tend to have overlapping values, which makes using a single variable a bad choice

when trying to determine whether an unknown tissue sample is healthy or cancerous. Instead, PCA is employed to determine the mixture of variables that provide the largest distinction between the two groups. Note that the discussion that follows is not a complete PCA study, where the number of input parameters is varied until the model is fully optimized, a predictive model is made, and samples are classified using the predictive model to test its accuracy. Instead, it is a rather brief discussion on the technique to illustrate the usefulness of the combined PEDXRF and EDXRD measurements.

PCA is a technique that takes a collection of observations for several variables and attempts to find the linear combination of variables that provides largest variance amongst the data<sup>[47,48]</sup>. The result of PCA is therefore the set of linear combinations of the supplied variables that yield the highest variance amongst the data, usually returned in order of variance. Thus, the first principal component leads to the largest separation of data points, while each subsequent component has a smaller effect on the overall distribution. For visualization purposes, usually only the first two components are plotted.

PCA was performed on the PEDXRF and EDXRD data separately. Figure 5.21 shows the XRF data plotted against its first two principal components, while Figure 5.22 shows the same for the XRD data. It is obvious from the figures that performing PCA allows for some distinction between the healthy and cancerous tissues, but there is still some overlap between the two. This overlap means that any predictive models made will have trouble distinguishing between the two groups if the measurements fall within this region, which can yield an incorrect classification.

In order to improve these results, PCA was performed on the combined dataset,

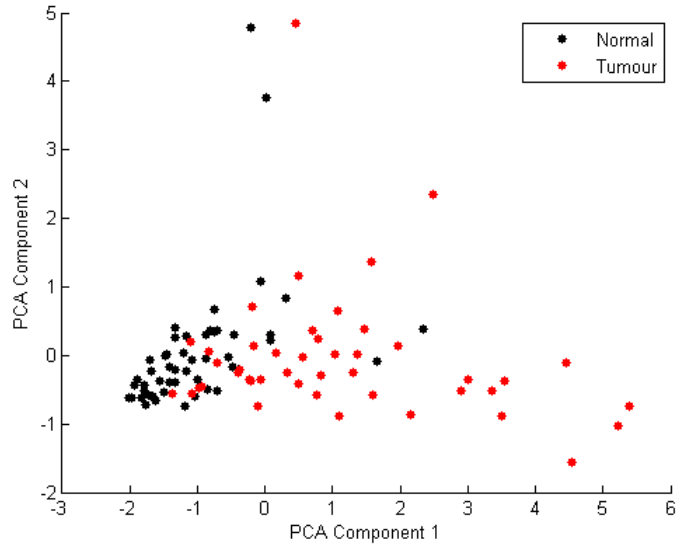


Figure 5.21: A plot showing the results of performing PCA on the XRF breast data.

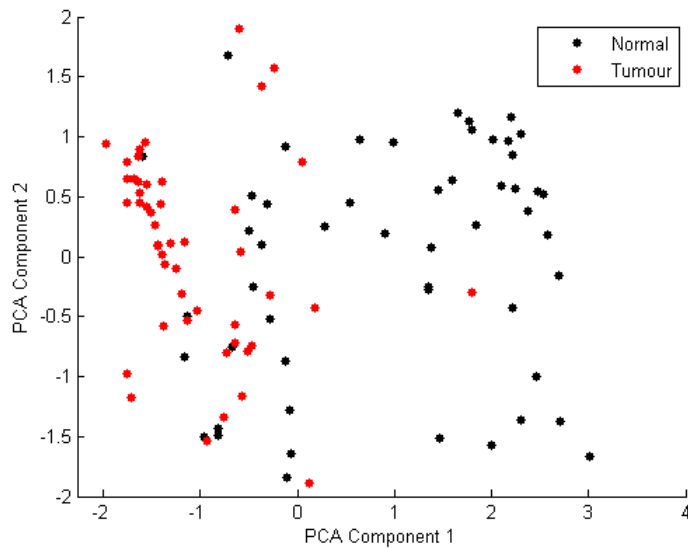


Figure 5.22: A plot showing the results of performing PCA on the XRD breast data.

the results of which are shown in Figure 5.23. In this case, the combination of the XRF and XRD data results in less overlap between the two groups, which would yield a significantly improved classification model.

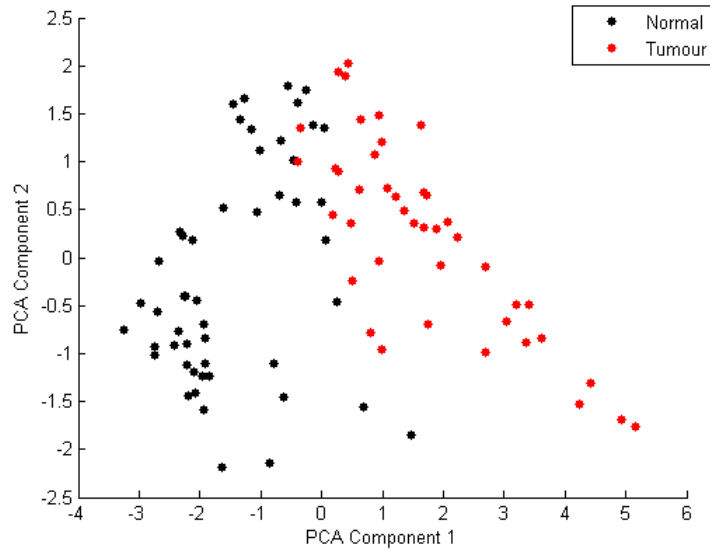


Figure 5.23: A plot showing the results of performing PCA on the combined XRF and XRD breast data.

It is evident from Figure 5.23 that using the combination of XRF and XRD data, a model for classifying an unknown breast tissue sample as cancerous or healthy, while only using a single technique results in significant overlap of the two groups. This experiment highlights some of the strengths of the combined PEDXRF and EDXRD spectrometry system, which can perform both experiments in quick succession.

While these results were promising, there were still improvements made to the PEDXRF system, which resulted in the final setup discussed in Chapter 3. Once this was completed, the breast tissue experiment was repeated again. Unfortunately, when the samples are sent for histology, they can no longer be returned for use in experiments, so a new sample set had to be used.

The last breast dataset measured contained 19 samples with invasive ductal carcinoma, with healthy tissue samples taken from the same patients, purchased from a tissue bank. For the PEDXRF measurements, the molybdenum secondary target was

used, since it is expected that zinc and rubidium concentrations will be significantly higher in the cancerous tissue. The tube settings were  $50kV$  and  $25mA$ . Since the new SDD with a much larger active area was used for this study, the measurement time was lowered to  $10min$ .

Figure 5.24 shows the zinc distribution within the dataset. When compared to Figure 5.20, the separation between the two groups is much larger than before. Following the same procedure, the measured population distributions were examined to see which elements had statistically different distributions between the normal and cancerous tissues. Matching with what was found previously, potassium, calcium, iron, zinc, and rubidium were the only elements that had statistically different distributions between the cancerous and healthy tissues. While this doesn't provide any additional information from the previous study, it did provide the same results in 10 minutes rather than 30 minutes.

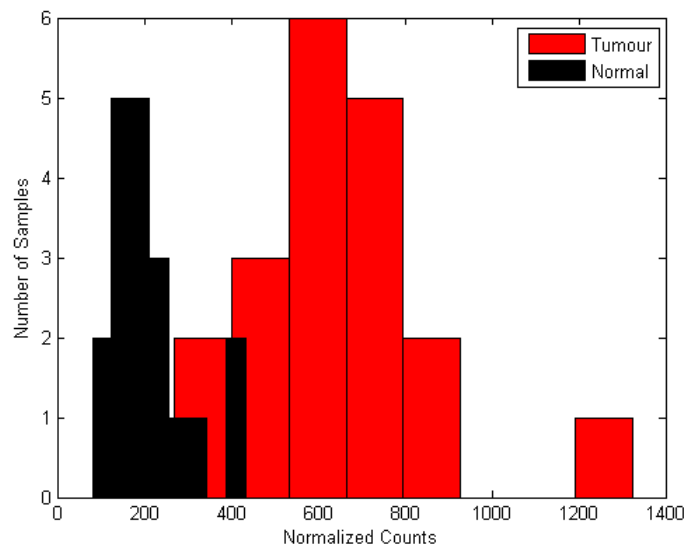


Figure 5.24: A plot showing the measured zinc in 19 normal and cancerous breast samples, using the final PEDXRF system.

Since the major change between these measurements and the previous breast sample set was the improved detector, it would be interesting to determine the optimal measurement time. While a 10 minute count corresponded to fluorescence peaks with at least 1000 counts, this does not necessarily correspond to better or worse results when performing the PCA study to separate the groups. As such, the samples were re-measured using the PEDXRF system for *5min*, *2.5min*, *1min*, and *30s*. Table 5.8 summarizes the results found from varying the measurement time.

Table 5.8: A table showing the statistical difference between the healthy and cancerous breast tissue distributions for different measurement times. The numerical values are p-values representing the likelihood that the two distributions are the same.

	600s	300s	150s	60s	30s
<b>Potassium</b>	$4 * 10^{-7}$	$3 * 10^{-7}$	$7 * 10^{-6}$	Same	Same
<b>Calcium</b>	$4 * 10^{-4}$	$2 * 10^{-3}$	$4 * 10^{-3}$	Same	Same
<b>Iron</b>	$2 * 10^{-5}$	$8 * 10^{-4}$	$9 * 10^{-4}$	$4 * 10^{-3}$	Same
<b>Zinc</b>	$4 * 10^{-7}$	$9 * 10^{-6}$	$2 * 10^{-6}$	$8 * 10^{-5}$	$6 * 10^{-5}$
<b>Rubidium</b>	$4 * 10^{-6}$	$9 * 10^{-4}$	$1 * 10^{-4}$	Same	Same

Looking at the results in Table 5.8, it is clear that the final PEDXRF system is capable of determining differences between healthy and cancerous tissues, even at measurement times as low as *30s*. However, it is not enough to have measurable differences, but rather determine how the PCA results look at various measurement times. Figure 5.25 to Figure 5.29 show the PCA results at the various counting times.

Looking at the figures, it is evident that the longer measurement times provide better results, with the 10 minute measurement resulting in complete separation between the two groups (see Figure 5.25). Even at a 2.5 minute measurement time, the PCA results are quite good, showing very little overlapping of the two groups. This test helps to prove that the combination of the high powered x-ray tube, large

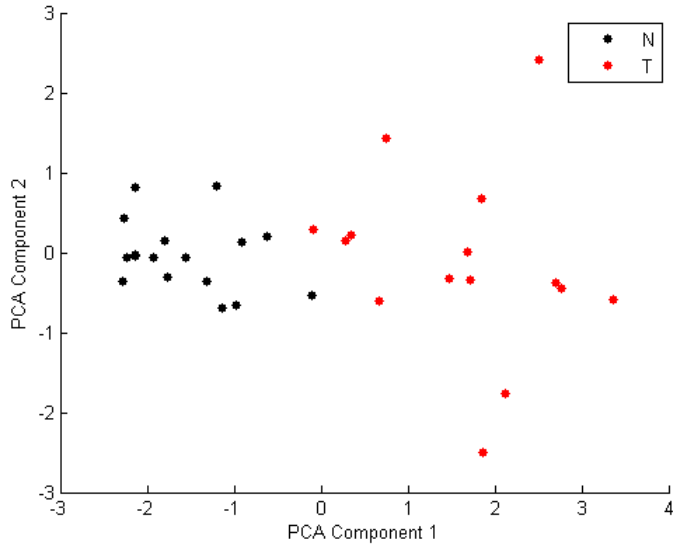


Figure 5.25: A plot showing the results of performing PCA on the final PEDXRF breast data when measured for 600s.

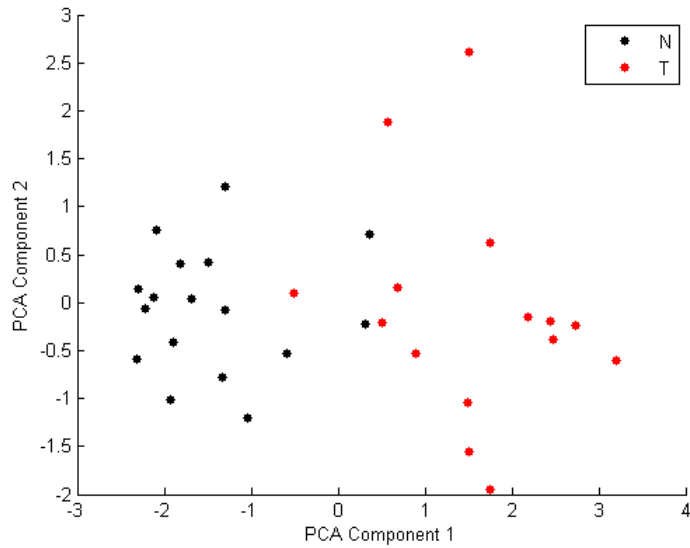


Figure 5.26: A plot showing the results of performing PCA on the final PEDXRF breast data when measured for 300s.

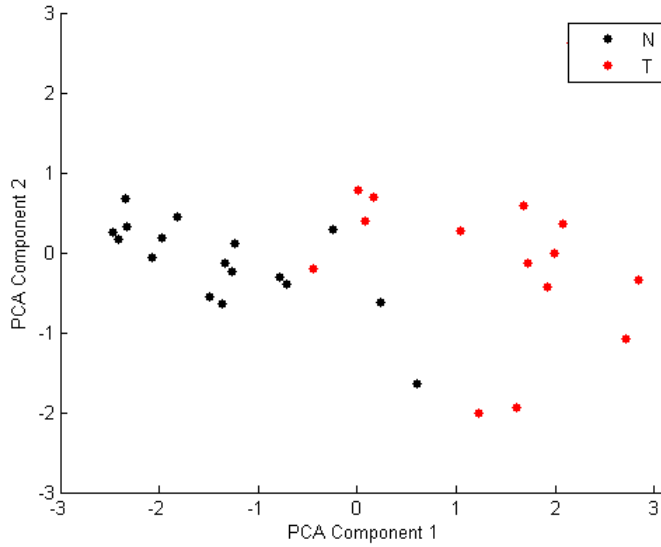


Figure 5.27: A plot showing the results of performing PCA on the final PEDXRF breast data when measured for 150s.

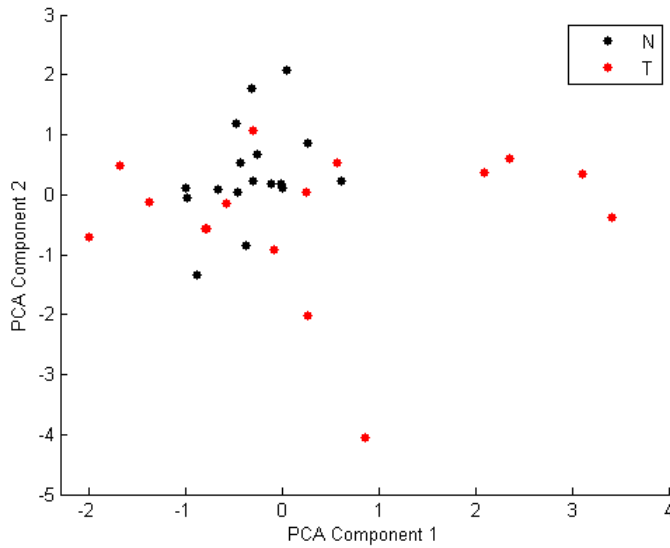


Figure 5.28: A plot showing the results of performing PCA on the final PEDXRF breast data when measured for 60s.

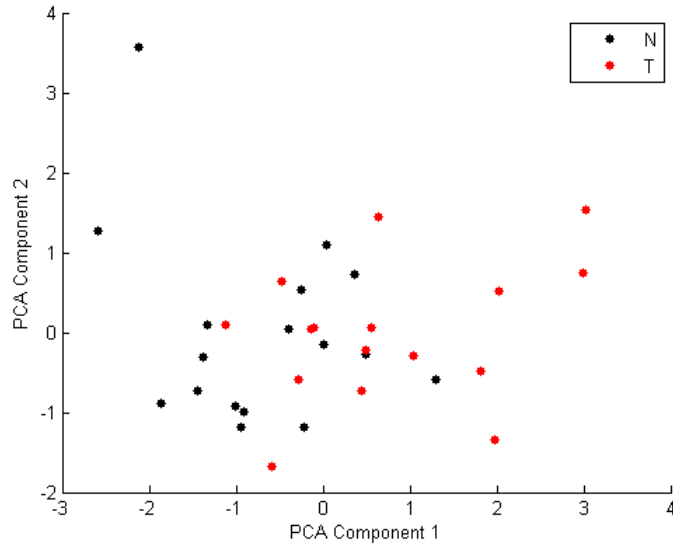


Figure 5.29: A plot showing the results of performing PCA on the final PEDXRF breast data when measured for 30s.

detector area, and PEDXRF technique can vastly decrease data acquisition times.

Ideally, a similar experiment would be performed on the EDXRD system, finding an optimal measurement time, especially when the results of both spectrometers are combined into the PCA model. However, when the PEDXRF measurements had finished, the HPGe detector required for the EDXRD measurements lost vacuum, leaving it unusable. Therefore, the EDXRD portion of this experiment must wait until that detector has been repaired.

### 5.3.3 Lung Tissue

The last dataset measured consisted of 23 matched pairs of tumorous lung tissue. This dataset consisted of 10 samples with squamous cell carcinoma of the lung, and 13 samples with adenocarcinoma of the lung, with healthy tissue samples taken from

the same patients. When previously examined using XRF and XRD, no discernible differences were found between the cancerous tissues (either separate or combined) and the healthy tissue<sup>[45]</sup>. Therefore, the purpose of measuring this dataset with the new combined PEDXRF and EDXRD spectrometer was to determine if the new system was capable of detecting differences between the two groups.

For the PEDXRF measurements, the molybdenum foil was chosen, as it would be able to excite the largest range of elements, with the x-ray tube was set to  $50kV$  and  $25mA$ . A 10 minute measurement time was chosen, as this configuration was easily capable of noticing differences in the breast tissue. Once again, the EDXRD measurement had to be postponed due to the broken HPGe detector.

Following the same procedure discussed with the cancerous breast tissues, the lung tissues were measured and the fluorescence peak areas were determined. The population distributions were examined for differences between the healthy and cancerous tissue groups. For the squamous cell carcinoma of the lung tissues, there were no elements with statistically different population distributions from the healthy tissues, matching what was found previously<sup>[45]</sup>. However, for the adenocarcinoma of the lung, there were three elements that showed significantly different distributions, calcium, copper, and rubidium. Again, a PCA was performed to determine whether a combination of these variables would allow for the normal and cancerous tissue groups to be separated. The result is shown in Figure 5.30.

Evident from Figure 5.30, there is no complete separation of the two groups. However, these results are still promising, as previous work found no differences at all between the two groups, illustrating the improvement of the PEDXRF spectrometer results over previously used equipment. These results warrant further investigation

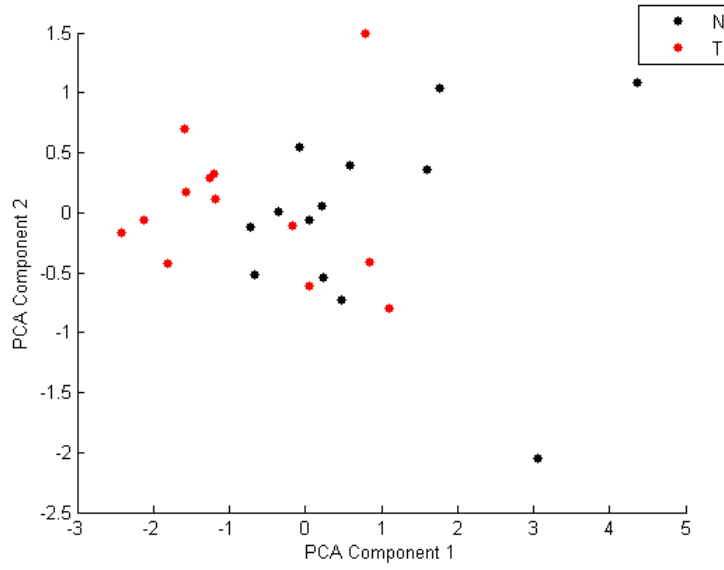


Figure 5.30: A plot showing the results of performing PCA on the adenocarcinoma of the lung samples.

of these lung tissues, using the new combined spectrometer.

# Chapter 6

## Conclusion

### 6.1 Conclusion & Discussion

Examining biological tissues and their underlying structure has yielded a significant improvement in our understanding of tissue function<sup>[1]</sup>. Whether it be healthy or diseased biological samples, investigating their elemental make-up and the structures they form can further our knowledge in the fields of biology, biochemistry, and medicine. With increased comprehension comes novel ways to further examine biological tissues, as well as model, track, and treat diseases.

A combined PEDXRF and EDXRD system was designed in order to examine and classify biological samples. This combined system is capable of determining the elemental composition and key structures of tissue samples, which can then be used to classify and differentiate between groups of samples<sup>[1-3,28,41]</sup>. While not being able to perform both measurements simultaneously, the common sample holder and simple design allows for samples to have both experiments performed on them within minutes. The use of two energy dispersive techniques allows for full use of a high powered

x-ray tube, reducing data collection time. When combined with the optimizations discussed in Chapter 4, this system is ideal for obtaining accurate elemental and structural information from biological samples in a short time.

The PEDXRF spectrometer has been optimized to measure trace transition metals, which often play an important role in biological and disease function<sup>[1-3]</sup>. Through extensive theoretical, MC simulation, and experimental work, the metallic secondary targets and geometry used by PEDXRF systems have been optimized<sup>[27]</sup>. It was found that for metallic secondary targets, the use of a thin target can significantly improve the SNR and MDLs of a PEDXRF measurement.

The setup uses optimally thick metallic secondary targets and an optimized geometry to provide MDLs for transition metals similar to or better than most contemporary systems<sup>[6,8,10]</sup>, in the same or less measurement time. Similarly, the EDXRD setup has the optimal angle, x-ray tube anode, and filtering for interrogating many biological samples. With its adjustable diffraction angle and the option to add a second diffraction detector at another angle, this setup is also capable of providing information equivalent to other systems, in the same or less data acquisition time<sup>[3,28,41]</sup>.

In order to determine whether the system is appropriate for measuring biological samples, three sets of soft tissue samples were measured, and had analysis performed. In the first experiment, a series of rat organs overloaded with iron was measured using the PEDXRF setup, using the optimal secondary target for measuring iron. This experiment illustrated one of the most critical aspects of the PEDXRF spectrometer, customizability. Since the secondary target can be swapped easily, the system can be tailored to measure specific elements, or ranges of elements. When considering many biological samples, the transition metals often play important roles in function,

which led to the choice of the molybdenum secondary target. However, if a different elemental range (or specific element) is of interest, then the secondary target can be swapped for something more likely to induce fluorescence.

This customizability, combined with the reduced scatter caused by the polarized x-rays, results in impressive MDLs across all atomic number ranges. Specifically, very low atomic number elements are notoriously hard to measure using XRF techniques, due to their decreased Photoelectric effect and fluorescence probabilities. However, with metallic secondary targets closer to their absorption edge, or more commonly Bragg polarizers, even the elements between sodium to chlorine are often detected in concentrations around  $10\mu\text{g}/\text{g}$ <sup>[10]</sup>. Since the MDLs found using the PEDXRF spectrometer match closely the MDLs of other groups, it is expected that when using appropriate secondary targets, these elements will be easily measured. These elements are commonly found in biological samples, in either trace or minor amounts<sup>[1]</sup>, and therefore are likely to be of interest in future experiments.

Additionally, examining heavy metals and higher atomic number elements is another common research topic<sup>[1,13,43,44]</sup>. These heavy elements are often poisonous and found in biological samples due to accidental or work exposure. Many of these elements can also be measured using the PEDXRF spectrometer, through proper choice of secondary target. One limitation when measuring heavy elements is the SDD, which will not be very useful in measuring high energy x-rays. However, due to this high sensitivity of the system, it is much simpler to measure the  $L$  fluorescence of higher atomic number elements<sup>[13,49]</sup>.

The next biological samples measured were two different sets of cancerous breast

tissues, with healthy breast tissue samples taken from the same patient. This experiment exemplifies the full capabilities of the combined spectrometry system. With the addition of XRD information to the XRF data, performing a PCA study on the data allows for easy differentiation between the normal and cancerous tissue. There were a few interesting results from this experiment, one of them being the statistically significant differences in the calcium and rubidium distributions in healthy and cancerous tissues. Previous studies did not find significant differences in these two elements, suggesting that the PEDXRF may have an increased sensitivity over a larger range of elements than other techniques used, although these findings warrant further research<sup>[3]</sup>.

As expected, performing PCA allowed for a much larger separation between the normal and cancerous tissues than any single measurement. Even so, except for the 10 minute measurement taken on the final PEDXRF setup, the PCA of just the XRF or XRD was not sufficient to fully separate the two groups. Fortunately, the combination of the two datasets into the PCA model provided much better results, than the single modality results. Although the EDXRD data could not be taken on the samples measured with the final PEDXRF system, due to a broken detector, it is a fair assumption that the addition of that dataset would provide even better PCA results. Additionally, the PCA results shown were done on the entire dataset, to illustrate the usefulness of the analysis technique, but a more thorough PCA treatment would likely yield improved results.

The study involving measuring the breast samples for increasingly shorter times also yielded promising results. While the longer counting times provided the best PCA results, there may exist a reasonable trade-off between the measurement time

and tissue classification accuracy. With decreased measurement times, it is possible to increase the size of the dataset, which may be another way to improve the results of a tissue classification model. Another approach may be to create a very strong model by using longer counting times, then measuring unknown samples for a shorter time, potentially yielding similar results. Either way, the fact that even 2.5 minute measurements provided fairly impressive PCA results provides strong evidence to the usefulness of this combined system when classifying biological tissues.

The last biological samples measured were two different lung tumours, adenocarcinoma of the lung, and squamous cell carcinoma of the lung. While previous studies failed to find any statistical differences between the healthy and cancerous tissues, PEDXRF results on the adenocarcinoma of the lung tissues showed differences in three elements. These results show the improvement of the XRF results over other experimental setups.

While only soft tissue samples were measured on the PEDXRF and EDXRD setup, it is fairly certain that the combined spectrometry system will still perform on other biological samples. The EDXRD was optimized to work on both soft tissues and bone samples, but the other angle options provided by the EDXRD block should provide a large range of measurable momentum transfers. Similarly, the PEDXRF spectrometer should be capable of measuring any type of sample, however, its effectiveness may depend on the type of sample. Since the deionized water phantoms and standard reference materials serve as suitable surrogates for soft tissues, no matrix corrections needed to be performed. Regardless of any additional work required, PEDXRF systems have been used to measure geological samples<sup>[6,10,11]</sup>, aerosols<sup>[12]</sup>, paintings<sup>[8]</sup>, and many other objects with great success<sup>[9,49]</sup>. This evidence suggests that both the

PEDXRF and EDXRD systems should be able to effectively analyze many types of biological samples, with little to no modifications.

When considering the future impact of the combined PEDXRF and EDXRD spectrometer, ideally it will become a common tool for classifying biological samples. With continued improvements and a larger variety of samples measured using the system, it may be possible to realize a clinically relevant version of the device. If predictive models based off measurements made on the system can be made for certain types of tissues, and these models can be shown to provide reliable, quick results, then a clinical version of the spectrometer may be able to provide healthcare professionals with information regarding unknown samples. As a concrete example, if it can be shown that the system can accurately determine invasive ductal carcinoma samples from healthy breast tissue, then an implementation of the spectrometer present in an operating suite may be able to provide a quick determination of clean surgical margins.

Evidently, a significant amount of work is still needed to realize such an implementation of the combined spectrometer. However, the work presented here outlines a basis for improving current predictive models by improving detection limits and reducing data acquisition time.

## 6.2 Future Work

Confident that the system is working well, there is a significant amount of work that can be done with the completed system. The future work for this project can be divided into three categories: improvements to the PEDXRF spectrometer, improvements to the EDXRD spectrometer, and future measurements to be performed using

the system.

### 6.2.1 PEDXRF Improvements

There are a few improvements that could be made to the PEDXRF that would improve its functionality and versatility. The first improvement would be attempting to remove the iron, nickel, and copper peaks present in background measurements. While the nickel response comes from the neck of the detector, it is hypothesized that the iron and copper signals arise from contaminants in the materials used to construct the PEDXRF system.

For the nickel, a *2mm* thick aluminum cap with a hole for x-ray transmission, placed over the detector head should be sufficient to remove the fluorescence, however, careful consideration must be taken to protect the beryllium window when placing the filter. The hole in the aluminum cap must be small enough to shield the nickel from incoming x-rays, while still being as large as possible to allow for maximum detection area.

Reducing or removing the iron and copper peaks is a more difficult procedure. These photons are already entering from the front of the detector, so a simple filter would not be able to stop them; the source of iron and copper x-rays would have to be removed instead. Since the current hypothesis is that the iron and copper are actually found as trace elements in the materials used to construct the PEDXRF system, this would correspond to re-manufacturing the setup using materials with a higher purity.

Another improvement that could be made would be replacing the lead collimators with a different material. While the lead *L* fluorescence doesn't overlap with any of

the measured elements, it may interfere with future measurements. Another suitable candidate for the collimator material is tin, which has been used in other PEDXRF setups, and is relatively easy to machine<sup>[33]</sup>. This would allow for the elements from gallium to zirconium, as well as lead, to be examined using the system, while only interfering with the low energy x-rays from potassium, calcium, and scandium.

The next area that could be improved is the secondary target choices. Currently, only molybdenum, copper, and zinc secondary targets are used in the PEDXRF system. However, various other metallic secondary targets could be useful for measuring elements in different ranges. Obtaining a Bragg polarizer could also help to improve excitation of low atomic number elements, being the optimal choice for elements between sodium and chlorine<sup>[6]</sup>. This also leads to another area of potential optimization, as the optimal placement, size, material, and exposure parameters for a Bragg polarizer could be determined.

Lastly, an adjustable stage 2 collimator would prove very useful for the PEDXRF system. Since the optimal choice stage 2 collimator matches the sample size, having a variable stage 2 collimator (or several different interchangeable sizes) would allow for samples of various sizes to be measured. This would also allow for comparing small spot size measurements to bulk sample measurements, which could help in understanding the distribution of elements within a sample.

### **6.2.2 EDXRD Improvements**

The EDXRD spectrometer also has a few areas that could be improved. The biggest drawback with the current design is re-aligning a detector for a new diffraction angle. It would greatly decrease setup time and improve measurement precision if a

system to lock the diffraction detectors in place existed. Currently, the design forces the user to manually align the detector, then lock it in place by affixing aluminum strapping on the optics table. Instead, a platform that the detector could sit on could be pinned to the central diffraction point, allowing for only rotational motion about that point. The detectors could then be fixed to that platform, and a system to accurately set the detection angle could be devised.

Another potential improvement would be to shorten the EDXRD block. While this would make the angle slits closer together, requiring improved alignment of the detector, the gain to fluence rate on the detector would make it a worthwhile project. This would allow the EDXRD to take up less space and have shorter data acquisition times. If the increase in fluence rate causes detector dead time issues, then the primary slit collimator width could be decreased, or ideally, the slits in the angle block could be decreased. While it is unlikely that biological tissues already measured have features that would require a thinner slit width, the shorter EDXRD block would allow for thinner angle slits without any detriment to the spectrometer functionality.

### **6.2.3 Future Measurements**

There are several other measurements that could be done now that the design of the combined PEDXRF and EDXRD spectrometer is completed. The first measurement to make would be other calibration lines for the PEDXRF system, in order to determine MDLs and provide numerical results for the other elements measured.

Secondly, the invasive ductal carcinoma samples that were run on the final PEDXRF system should be measured using the EDXRD system, once the detector has been repaired. This would allow for a proper PCA study to be performed on that dataset,

realizing the full potential of the combined system. During this study, the data acquisition time for the EDXRD should also be varied, so that the effect of increased data uncertainty has on the diffraction data. Once completed, a series of PCA models could be made to determine the optimal measurement times for both the PEDXRF and EDXRD system, for breast tissues with invasive ductal carcinoma.

Another experiment that should be performed is the continuation of the lung tissue measurements. Although there were no found differences between the squamous cell carcinoma of the lung and healthy lung tissue, this could be due to small sample size or short data acquisition times. A more thorough examination is required to determine that there are no measurable differences between these two groups with the PEDXRF spectrometer. Similarly for the adenocarcinoma of the lung, further measurements with longer acquisition times and more samples would allow for much better differentiation between the healthy and tumourous tissues. Additionally, if most of the differences are found in elements below zinc, measurements with a zinc secondary target would likely yield improved results. Lastly, the EDXRD measurements should be performed on these samples.

After this measurement, it is recommended to measure all manner of different biological samples using the system. As a larger variety of samples are measured using the equipment, more information regarding the effectiveness of the spectrometer and its ability to classify biological samples will be gained. Eventually, if the goal was to develop a clinical system, the wider range of samples measured will provide information regarding further improvements that could be made to the system, as well as its limitations in clinical settings.

# Appendix A

## GEANT4 Code

Here is the Geant4 code used for most of the simulations. Pieces have been changed over time, but this is the most current, which runs the entire tri-axial measurement.

The macro files are shown below.

```
// *****
//
//This is the main run program for tri-axial MC code
//Written by: Eric Johnston, Latest Update 2017-04-28
//
// *****
// * License and Disclaimer *
// * *
// * The Geant4 software is copyright of the Copyright Holders of *
// * the Geant4 Collaboration. It is provided under the terms and *
// * conditions of the Geant4 Software License, included in the file *
// * LICENSE and available at http://cern.ch/geant4/license . These *
// * include a list of copyright holders. *
// * *
// * Neither the authors of this software system, nor their employing *
// * institutes,nor the agencies providing financial support for this *
// * work make any representation or warranty, express or implied, *
// * regarding this software system or assume any liability for its *
// * use. Please see the license in the file LICENSE and URL above *
// * for the full disclaimer and the limitation of liability. *
// * *
// * This code implementation is the result of the scientific and *
```

```
// * technical work of the GEANT4 collaboration. *
// * By using, copying, modifying or distributing the software (or *
// * any work based on the software) you agree to acknowledge its *
// * use in resulting scientific publications, and indicate your *
// * acceptance of all terms of the Geant4 Software license. *
// *****

//Include user added code that will be required to run managers
#include "DetectorConstruction.hh"
#include "ActionInitialization.hh"
#include "DetectorMessenger.hh"
#include "PhysicsList.hh"

//Required for any build
#include "G4RunManager.hh"
#include "G4UImanager.hh"

#ifdef G4VIS_USE
    #include "G4VisExecutive.hh"
#endif

#ifdef G4UI_USE
    #include "G4UIExecutive.hh"
#endif

#include "Randomize.hh"
#include "G4SystemOfUnits.hh"
#include "G4GeometrySampler.hh"
#include "G4ImportanceBiasing.hh"

//This is the first method run by the program, can take arguments
int main(int argc, char** argv)
{
    // Choose the Random engine
    G4Random::setTheEngine(new CLHEP::RanecuEngine);

    // Construct the default run manager
    G4RunManager* runManager = new G4RunManager;

    // Set mandatory initialization classes
    // Detector construction
    DetectorConstruction* thisDetectorConstruction =
        new DetectorConstruction();
    runManager->SetUserInitialization(thisDetectorConstruction);
}
```

```
// Physics list
G4VModularPhysicsList* physicsList = new PhysicsList();
physicsList->SetVerboseLevel(0);

runManager->SetUserInitialization(physicsList);

// User action initialization
runManager->SetUserInitialization(new ActionInitialization());

// Initialize G4 kernel
runManager->Initialize();

#ifdef G4VIS_USE
    // Initialize visualization
    G4VisManager* visManager = new G4VisExecutive;
    visManager->Initialize();
#endif

// Get the pointer to the User Interface manager
G4UImanager* UImanager = G4UImanager::GetUIpointer();

if (argc!=1)
{
    // batch mode
    G4String command = "/control/execute ";
    G4String fileName = argv[1];
    UImanager->ApplyCommand(command+fileName);
}
else
{
    // interactive mode : define UI session
#ifdef G4UI_USE
        G4UIExecutive* ui = new G4UIExecutive(argc, argv, "csh");
#ifdef G4VIS_USE
            UImanager->ApplyCommand("/control/execute init.mac");
#else
            UImanager->ApplyCommand("/control/execute init.mac");
#endif
        #endif
        ui->SessionStart();
        delete ui;
    #endif
}

// Job termination

#ifdef G4VIS_USE
```

```

        delete visManager;
    #endif

    delete runManager;

    return 0;
}
// *****
//This is the action initialization header file, used for user
//specified action initialization. It is used to set the the other user
//based actions

#ifndef ActionInitialization_h
#define ActionInitialization_h 1

#include "G4VUserActionInitialization.hh"

//Action initialization class
class ActionInitialization : public G4VUserActionInitialization
{
    public:
        ActionInitialization();
        virtual ~ActionInitialization();

        virtual void BuildForMaster() const;
        virtual void Build() const;
};

#endif
// *****
//This is the action initialization class file, used for user
//specified action initialization. It is used to set the the other user
//based actions

//Add header files for user specified actions
#include "ActionInitialization.hh"

#include "PrimaryGeneratorAction.hh"
#include "RunAction.hh"
#include "EventAction.hh"
#include "SteppingAction.hh"

//Constructor, extends G4VUserActionInitialization
ActionInitialization::ActionInitialization()
: G4VUserActionInitialization()
{}

```

```

//Deconstructor
ActionInitialization::~ActionInitialization()
{}

//Set user classes here for master, used for multithread
void ActionInitialization::BuildForMaster() const
{
    SetUserAction(new RunAction);
}

//Set user classes here for slaves
void ActionInitialization::Build() const
{
    SetUserAction(new PrimaryGeneratorAction);
    SetUserAction(new RunAction);

    //This must be a pointer so it can be passed through
    EventAction* eventAction = new EventAction;
    SetUserAction(eventAction);

    SetUserAction(new SteppingAction(eventAction));
}
// *****
//This is the detector construction header file, this method sets up
//the geometry for the runs

#ifndef DetectorConstruction_h
#define DetectorConstruction_h 1

#include "G4VUserDetectorConstruction.hh"

#include "G4ThreeVector.hh"
#include "G4Material.hh"
#include "G4Tubs.hh"
#include "G4Box.hh"

class G4LogicalVolume;
class G4VPhysicalVolume;
class DetectorMessenger;
class G4MultiFunctionalDetector;

//Detector construction class
class DetectorConstruction : public G4VUserDetectorConstruction
{
public:

```

```

DetectorConstruction();
virtual ~DetectorConstruction();

virtual G4VPhysicalVolume* Construct();

void SetNewCollimators (G4ThreeVector newCollimatorRadius);
void SetNewTraceElement (G4String newElement, G4double newPPM);
void SetNewSecondaryTarget (G4String newElement,
    G4double newThickness);

G4LogicalVolume* GetWorldVolume() const
    {return thisWorldVolume;}
G4LogicalVolume* GetSecondaryTargetVolume() const
    {return thisSecondaryTargetVolume; }
G4LogicalVolume* GetSampleVolume() const
    {return thisSampleVolume; }
G4LogicalVolume* GetPolDetectorVolume() const
    {return thisPolDetectorVolume; }
G4LogicalVolume* GetAntiPolDetectorVolume() const
    {return thisAntiPolDetectorVolume; }
G4VPhysicalVolume* GetWorldPhysicalVolume() const
    {return thisWorldPhysicalVolume; }

protected:
G4VPhysicalVolume* thisWorldPhysicalVolume;
G4VPhysicalVolume* secondaryTargetPhysical;
G4LogicalVolume* thisWorldVolume;
G4LogicalVolume* thisSecondaryTargetVolume;
G4LogicalVolume* thisSampleVolume;
G4LogicalVolume* thisPolDetectorVolume;
G4LogicalVolume* thisAntiPolDetectorVolume;
G4LogicalVolume* sampleLogical;
G4LogicalVolume* secondaryTargetLogical;
DetectorMessenger* thisDetectorMessenger;
G4double thisCollimator1Radius;
G4double thisCollimator2Radius;
G4double thisCollimator3Radius;
G4Tubs* collimator1Inside;
G4Tubs* collimator2Inside;
G4Tubs* collimator3Inside;
G4Box* secondaryTargetSolid;
G4double thisTraceElementPPM;
G4double thisSecondaryTargetThickness;
G4Material* thisSecondaryTargetMaterial;
G4Material* thisTraceElement;
G4Material* sampleBaseMaterial;

```

```

        G4Material* sampleMaterial;
        G4MultiFunctionalDetector* polScorer;
        G4MultiFunctionalDetector* antiPolScorer;
};

#endif
// *****
//This is the detector construction class file, this method sets up the
//geometry for the runs

//For tri-axial, we want to put everything as close together, and have
//both a polarized and anti-polarized detector, to collect more data

//Add header files
#include "DetectorConstruction.hh"

#include "DetectorMessenger.hh"
#include "SampleBiasing.hh"

#include "G4NistManager.hh"
#include "G4Material.hh"
#include "G4Box.hh"
#include "G4Tubs.hh"
#include "G4SubtractionSolid.hh"
#include "G4LogicalVolume.hh"
#include "G4PVPlacement.hh"
#include "G4RotationMatrix.hh"
#include "G4Transform3D.hh"
#include "G4SystemOfUnits.hh"

#include "G4MultiFunctionalDetector.hh"
#include "G4VPrimitiveScorer.hh"
#include "G4PSEnergyDeposit.hh"
#include "G4SDManager.hh"

//Constructor, extends G4VUserDetectorConstruction
DetectorConstruction::DetectorConstruction()
    : G4VUserDetectorConstruction(),
      thisWorldVolume(0),thisSecondaryTargetVolume(0),
      thisSampleVolume(0),thisPolDetectorVolume(0),
      thisAntiPolDetectorVolume(0),thisCollimator1Radius(0.5*cm),
      thisCollimator2Radius(0.5*cm),thisCollimator3Radius(0.5*cm),
      thisTraceElementPPM(0),thisSecondaryTargetThickness(50.*um),
      thisWorldPhysicalVolume(0)
{
    //Create the detector messenger

```

```
thisDetectorMessenger = new DetectorMessenger (this);

//Set a default material for the trace element, even though it has
//0ppm by default
G4NistManager* nist = G4NistManager::Instance();
thisTraceElement = nist->FindOrBuildMaterial("G4_Fe");
thisSecondaryTargetMaterial = nist->FindOrBuildMaterial("G4_Cu");
}

//Destructor
DetectorConstruction::~DetectorConstruction()
{
    delete thisWorldVolume;
    delete thisSecondaryTargetVolume;
    delete thisSampleVolume;
    delete thisPolDetectorVolume;
    delete thisAntiPolDetectorVolume;
    delete thisDetectorMessenger;
}

//Called at the beginning of a simulation to setup the geometry
G4VPhysicalVolume* DetectorConstruction::Construct()
{
    //Get the nist manager, for looking up materials
    G4NistManager* nist = G4NistManager::Instance();

    //Check for overlapping volumes
    G4bool checkOverlaps = true;

    //The source itself will be placed at (-1cm,-1cm,-1cm), with radius
    //1cm, travelling in the positive z dir. It will travel to the ST at
    //(-1cm,-1cm,1cm), and scatter in the positive y dir. Then the beam
    //will travel to the sample at (-1cm,1cm,1cm), and scatter towards
    //the detector. The pol detector is placed at (1cm,1cm,1cm), while
    //the antipol detector is placed at (-1cm,1cm,-1cm) roughly, with
    //the actual detector placed right at the collimator face, to
    //reduce scatter. Around the detector will be a layer of lead,
    //protecting it from scatter

    //Define other variables to be used here
    //World Variables
    G4double worldSize = 5.*cm;
    G4Material* worldMaterial = nist->FindOrBuildMaterial("G4_AIR");

    G4Box* worldSolid;
    G4LogicalVolume* worldLogical;
```

```

G4VPhysicalVolume* worldPhysical;

//Collimator Variables
G4double collimatorThickness = 0.2*cm;
G4double collimatorWidth = 1.6*cm;
G4Material* collimatorMaterial1 =
    nist->FindOrBuildMaterial("G4_Pb");
G4Material* collimatorMaterial2 =
    nist->FindOrBuildMaterial("G4_Al");

G4ThreeVector collimator1Position1 =
    G4ThreeVector(-1.*cm,-1.*cm,0.*cm-collimatorThickness/2);
G4ThreeVector collimator1Position2 =
    G4ThreeVector(-1.*cm,-1.*cm,0.*cm+collimatorThickness/2);
G4ThreeVector collimator2Position1 =
    G4ThreeVector(-1.*cm,0.*cm-collimatorThickness/2,1.*cm);
G4ThreeVector collimator2Position2 =
    G4ThreeVector(-1.*cm,0.*cm+collimatorThickness/2,1.*cm);
G4ThreeVector collimator3Position1 =
    G4ThreeVector(0.*cm-collimatorThickness/2,1.*cm,1.*cm);
G4ThreeVector collimator3Position2 =
    G4ThreeVector(0.*cm+collimatorThickness/2,1.*cm,1.*cm);
G4ThreeVector collimator4Position1 =
    G4ThreeVector(-1.*cm,1.*cm,0.*cm+collimatorThickness/2);
G4ThreeVector collimator4Position2 =
    G4ThreeVector(-1.*cm,1.*cm,0.*cm-collimatorThickness/2);

G4RotationMatrix collimator2RotationMatrix1 = G4RotationMatrix();
G4RotationMatrix collimator2RotationMatrix2 = G4RotationMatrix();
G4RotationMatrix collimator3RotationMatrix1 = G4RotationMatrix();
G4RotationMatrix collimator3RotationMatrix2 = G4RotationMatrix();

collimator2RotationMatrix1.rotateX(90*deg);
collimator2RotationMatrix2.rotateX(90*deg);
collimator3RotationMatrix1.rotateY(90*deg);
collimator3RotationMatrix2.rotateY(90*deg);

G4Transform3D collimator2Transform1 =
    G4Transform3D(collimator2RotationMatrix1,collimator2Position1);
G4Transform3D collimator2Transform2 =
    G4Transform3D(collimator2RotationMatrix2,collimator2Position2);
G4Transform3D collimator3Transform1 =
    G4Transform3D(collimator3RotationMatrix1,collimator3Position1);
G4Transform3D collimator3Transform2 =
    G4Transform3D(collimator3RotationMatrix2,collimator3Position2);

```

```
G4Box* collimatorOutside;
G4SubtractionSolid* collimator1Solid;
G4SubtractionSolid* collimator2Solid;
G4SubtractionSolid* collimator3Solid;
G4LogicalVolume* collimator1Logical1;
G4LogicalVolume* collimator1Logical2;
G4LogicalVolume* collimator2Logical1;
G4LogicalVolume* collimator2Logical2;
G4LogicalVolume* collimator3Logical1;
G4LogicalVolume* collimator3Logical2;
G4LogicalVolume* collimator4Logical1;
G4LogicalVolume* collimator4Logical2;
G4VPhysicalVolume* collimator1Physical1;
G4VPhysicalVolume* collimator1Physical2;
G4VPhysicalVolume* collimator2Physical1;
G4VPhysicalVolume* collimator2Physical2;
G4VPhysicalVolume* collimator3Physical1;
G4VPhysicalVolume* collimator3Physical2;
G4VPhysicalVolume* collimator4Physical1;
G4VPhysicalVolume* collimator4Physical2;

//Secondary Target Variables
G4double secondaryTargetWidth = 1.5*cm;

G4ThreeVector secondaryTargetPosition = G4ThreeVector(-1.*cm,-1.*cm
,1.*cm+thisSecondaryTargetThickness/std::sqrt(2.));
G4RotationMatrix secondaryTargetRotationMatrix =G4RotationMatrix();
secondaryTargetRotationMatrix.rotateX(45.*deg);
G4Transform3D secondaryTargetTransform =
    G4Transform3D(secondaryTargetRotationMatrix,
    secondaryTargetPosition);

//Sample Variables
G4double sampleThickness = 500.*um;
G4double sampleRadius = 0.95*cm;
sampleBaseMaterial = nist->FindOrBuildMaterial("G4_WATER");

G4ThreeVector samplePosition = G4ThreeVector(-1.*cm,1.*cm,1.*cm);
G4RotationMatrix sampleRotationMatrix = G4RotationMatrix();
sampleRotationMatrix.rotateY(-45.*deg);
sampleRotationMatrix.rotateX(-45.*deg);
G4Transform3D sampleTransform =
    G4Transform3D(sampleRotationMatrix,samplePosition);

G4Tubs* sampleSolid;
G4VPhysicalVolume* samplePhysical;
```

```
//Detector Variables
G4double detectorRadius = 0.5*cm;
G4double detectorWindowThickness = 0.05*mm;
G4double detectorFilterThickness = 0.02*um;
G4double detectorDeadLayerThickness = 0.1*um;
G4double detectorThickness = 1.*cm;
G4Material* detectorWindowMaterial =
    nist->FindOrBuildMaterial("G4_Be");
G4Material* detectorFilterMaterial =
    nist->FindOrBuildMaterial("G4_Au");
G4Material* detectorMaterial = nist->FindOrBuildMaterial("G4_Si");

G4ThreeVector polDetectorWindowPosition = collimator3Position2 +
    G4ThreeVector(0.5*(collimatorThickness +
    detectorWindowThickness),0,0);
G4ThreeVector polDetectorFilterPosition = polDetectorWindowPosition
    + G4ThreeVector(0.5*(detectorWindowThickness +
    detectorFilterThickness),0,0);
G4ThreeVector polDetectorDeadLayerPosition =
    polDetectorFilterPosition + G4ThreeVector(0.5 *
    (detectorFilterThickness + detectorDeadLayerThickness),0,0);
G4ThreeVector polDetectorPosition = polDetectorDeadLayerPosition +
    G4ThreeVector(0.5*(detectorDeadLayerThickness +
    detectorThickness),0,0);

G4ThreeVector antiPolDetectorWindowPosition = collimator4Position2
    -G4ThreeVector(0,0,0.5*(collimatorThickness+
    detectorWindowThickness));
G4ThreeVector antiPolDetectorFilterPosition =
    antiPolDetectorWindowPosition - G4ThreeVector(0,0,0.5*
    (detectorWindowThickness+detectorFilterThickness));
G4ThreeVector antiPolDetectorDeadLayerPosition =
    antiPolDetectorFilterPosition - G4ThreeVector(0,0,0.5*
    (detectorFilterThickness+detectorDeadLayerThickness));
G4ThreeVector antiPolDetectorPosition =
    antiPolDetectorDeadLayerPosition - G4ThreeVector(0,0,0.5*
    (detectorDeadLayerThickness+detectorThickness));

G4RotationMatrix polDetectorRotation = G4RotationMatrix();
polDetectorRotation.rotateY(90.*deg);
G4Transform3D polDetectorTransform = G4Transform3D
    (polDetectorRotation,polDetectorPosition);
G4Transform3D polDetectorDeadLayerTransform = G4Transform3D
    (polDetectorRotation,polDetectorDeadLayerPosition);
G4Transform3D polDetectorFilterTransform = G4Transform3D
```

```

        (polDetectorRotation,polDetectorFilterPosition);
G4Transform3D polDetectorWindowTransform = G4Transform3D
        (polDetectorRotation,polDetectorWindowPosition);

G4Tubs* detectorSolid;
G4Tubs* detectorDeadLayerSolid;
G4Tubs* detectorFilterSolid;
G4Tubs* detectorWindowSolid;
G4LogicalVolume* polDetectorLogical;
G4LogicalVolume* polDetectorDeadLayerLogical;
G4LogicalVolume* polDetectorFilterLogical;
G4LogicalVolume* polDetectorWindowLogical;
G4LogicalVolume* antiPolDetectorLogical;
G4LogicalVolume* antiPolDetectorDeadLayerLogical;
G4LogicalVolume* antiPolDetectorFilterLogical;
G4LogicalVolume* antiPolDetectorWindowLogical;
G4VPhysicalVolume* polDetectorPhysical;
G4VPhysicalVolume* polDetectorDeadLayerPhysical;
G4VPhysicalVolume* polDetectorFilterPhysical;
G4VPhysicalVolume* polDetectorWindowPhysical;
G4VPhysicalVolume* antiPolDetectorPhysical;
G4VPhysicalVolume* antiPolDetectorDeadLayerPhysical;
G4VPhysicalVolume* antiPolDetectorFilterPhysical;
G4VPhysicalVolume* antiPolDetectorWindowPhysical;

//Detector shield variables
G4double detectorShieldThickness = detectorThickness +
        detectorDeadLayerThickness +detectorFilterThickness +
        detectorWindowThickness;
G4Material* detectorShieldMaterial =
        nist->FindOrBuildMaterial("G4_Pb");

G4ThreeVector polDetectorShieldPosition = collimator3Position2 +
        G4ThreeVector(0.5*(collimatorThickness+detectorShieldThickness)
        ,0,0);
G4ThreeVector antiPolDetectorShieldPosition = collimator4Position2
        -G4ThreeVector(0,0,0.5*(collimatorThickness+
        detectorShieldThickness));

G4Transform3D polDetectorShieldTransform = G4Transform3D
        (polDetectorRotation,polDetectorShieldPosition);

G4Box* detectorShieldOutside;
G4Tubs* detectorShieldInside;
G4SubtractionSolid* detectorShieldSolid;
G4LogicalVolume* polDetectorShieldLogical;

```

```

G4LogicalVolume* antiPolDetectorShieldLogical;
G4VPhysicalVolume* polDetectorShieldPhysical;
G4VPhysicalVolume* antiPolDetectorShieldPhysical;

//Create the world

//Create the solid, noting that the dimension is the half-length,
//not total
worldSolid = new G4Box
    ("World",0.5*worldSize,0.5*worldSize,0.5*worldSize);

//Create the logical volume
worldLogical = new
    G4LogicalVolume(worldSolid,worldMaterial,"World");

//Create the physical volume to hold it, centred at 0,0,0
worldPhysical = new G4PVPlacement(0,G4ThreeVector(),worldLogical,
    "World",0,false,0,checkOverlaps);

//Create the secondary target

//Create the solid, again it's a box with with half-lengths
secondaryTargetSolid = new G4Box("Secondary Target",
    0.5*secondaryTargetWidth,0.5*secondaryTargetWidth,
    0.5*thisSecondaryTargetThickness);

//Create the logical volume
secondaryTargetLogical = new G4LogicalVolume
    (secondaryTargetSolid,thisSecondaryTargetMaterial,
    "Secondary Target");

//Create the physical volume, centre it at (-1,-1,1)
//rotated 45degrees about y
secondaryTargetPhysical = new G4PVPlacement
    (secondaryTargetTransform,secondaryTargetLogical,
    "Secondary Target",worldLogical,false,0,checkOverlaps);

//Create the sample

//Create the material, a mixture of base material and trace element
//Use just the base material density, assume the trace is small
sampleMaterial = new G4Material
    ("Sample",sampleBaseMaterial->GetDensity(),2);
sampleMaterial->AddMaterial
    (sampleBaseMaterial,1-thisTraceElementPPM/(10^6));
sampleMaterial->AddMaterial

```

```
(thisTraceElement,thisTraceElementPPM/(10^6));

//Print the materials to the screen
G4cout << *(G4Material::GetMaterialTable());

//Create the solid, another box
sampleSolid = new G4Tubs("Sample",0,sampleRadius,
    0.5*sampleThickness,0,360.*deg);

//Create the logical volume
sampleLogical = new G4LogicalVolume(sampleSolid,
    sampleMaterial,"Sample");

//Create the physical volume, rotated about y and x, to get it on
//two angles
samplePhysical = new G4PVPlacement(sampleTransform,sampleLogical,
    "Sample",worldLogical,false,0,checkOverlaps);

//Create the collimators

//Create the solids
collimatorOutside = new G4Box ("Collimator Outside",
    0.5*collimatorWidth,0.5*collimatorWidth,
    0.5*collimatorThickness);

collimator1Inside = new G4Tubs("Collimator 1 Inside",
    0,thisCollimator1Radius,
    0.6*collimatorThickness,0,360.*deg);

collimator2Inside = new G4Tubs("Collimator 2 Inside",
    0,thisCollimator2Radius,
    0.6*collimatorThickness,0,360.*deg);

collimator3Inside = new G4Tubs("Collimator 3 Inside",
    0,thisCollimator3Radius,
    0.6*collimatorThickness,0,360.*deg);

collimator1Solid = new G4SubtractionSolid("Collimator 1",
    collimatorOutside,collimator1Inside);

collimator2Solid = new G4SubtractionSolid("Collimator 1",
    collimatorOutside,collimator2Inside);

collimator3Solid = new G4SubtractionSolid("Collimator 1",
    collimatorOutside,collimator3Inside);
```

```
//Create the logical volumes
collimator1Logical1 = new G4LogicalVolume (collimator1Solid,
    collimatorMaterial1,"Collimator 1 Pb");

collimator1Logical2 = new G4LogicalVolume (collimator1Solid,
    collimatorMaterial2,"Collimator 1 Al");

collimator2Logical1 = new G4LogicalVolume (collimator2Solid,
    collimatorMaterial1,"Collimator 2 Pb");

collimator2Logical2 = new G4LogicalVolume (collimator2Solid,
    collimatorMaterial2,"Collimator 2 Al");

collimator3Logical1 = new G4LogicalVolume (collimator3Solid,
    collimatorMaterial1,"Collimator 3 Pb");

collimator3Logical2 = new G4LogicalVolume (collimator3Solid,
    collimatorMaterial2,"Collimator 3 Al");

collimator4Logical1 = new G4LogicalVolume (collimator3Solid,
    collimatorMaterial1,"Collimator 4 Pb");

collimator4Logical2 = new G4LogicalVolume (collimator3Solid,
    collimatorMaterial2,"Collimator 4 Al");

//Create the physical volumes
collimator1Physical1 = new G4PVPlacement(0,collimator1Position1,
    collimator1Logical1,"Collimator 1 Pb",worldLogical,false,0,
    checkOverlaps);

collimator1Physical2 = new G4PVPlacement(0,collimator1Position2,
    collimator1Logical2,"Collimator 1 Al",worldLogical,false,0,
    checkOverlaps);

collimator2Physical1 = new G4PVPlacement(collimator2Transform1,
    collimator2Logical1,"Collimator 2 Pb",worldLogical,false,0,
    checkOverlaps);

collimator2Physical2 = new G4PVPlacement(collimator2Transform2,
    collimator2Logical2,"Collimator 2 Al",worldLogical,false,0,
    checkOverlaps);

collimator3Physical1 = new G4PVPlacement(collimator3Transform1,
    collimator3Logical1,"Collimator 3 Pb",worldLogical,false,0,
    checkOverlaps);
```

```
collimator3Physical2 = new G4PVPlacement(collimator3Transform2,
    collimator3Logical2,"Collimator 3 Al",worldLogical,false,0,
    checkOverlaps);

collimator4Physical1 = new G4PVPlacement(0,collimator4Position1,
    collimator4Logical1,"Collimator 4 Pb",worldLogical,false,0,
    checkOverlaps);

collimator4Physical2 = new G4PVPlacement(0,collimator4Position2,
    collimator4Logical2,"Collimator 4 Al",worldLogical,false,0,
    checkOverlaps);

//Create the polarization detector

//Create the solids
detectorSolid = new G4Tubs("Detector",0,detectorRadius,
    0.5*detectorThickness,0,360.*deg);

detectorDeadLayerSolid = new G4Tubs("Detector Dead Layer",0,
    detectorRadius,
    0.5*detectorDeadLayerThickness,0,360.*deg);

detectorFilterSolid = new G4Tubs("Detector Filter",0,detectorRadius
    ,0.5*detectorFilterThickness,0,360.*deg);

detectorWindowSolid = new G4Tubs("Detector Window",0,detectorRadius
    ,0.5*detectorWindowThickness,0,360.*deg);

//Create the logical volumes
polDetectorLogical = new G4LogicalVolume(detectorSolid,
    detectorMaterial,"Polarized Detector");

polDetectorDeadLayerLogical = new G4LogicalVolume
    (detectorDeadLayerSolid,detectorMaterial,
    "Polarized Detector Dead Layer");

polDetectorFilterLogical = new G4LogicalVolume(detectorFilterSolid,
    detectorFilterMaterial,"Polarized Detector Filter");

polDetectorWindowLogical = new G4LogicalVolume(detectorWindowSolid,
    detectorWindowMaterial,"Polarized Detector Window");

//Create the physical volumes
polDetectorPhysical = new G4PVPlacement(polDetectorTransform,
    polDetectorLogical,"Polarized Detector",worldLogical,false,0,
    checkOverlaps);
```

```
polDetectorDeadLayerPhysical = new G4PVPlacement
    (polDetectorDeadLayerTransform,polDetectorDeadLayerLogical,
     "Polarized Detector Dead Layer",worldLogical,false,0,
     checkOverlaps);

polDetectorFilterPhysical = new G4PVPlacement
    (polDetectorFilterTransform,
     polDetectorFilterLogical,"Polarized Detector Filter",
     worldLogical,false,0,checkOverlaps);

polDetectorWindowPhysical = new G4PVPlacement
    (polDetectorWindowTransform,polDetectorWindowLogical,
     "Polarized Detector Window",worldLogical,false,0,
     checkOverlaps);

//Create the anti-polarization detector
//Solids created above
//Create the logical volumes
antiPolDetectorLogical = new G4LogicalVolume(detectorSolid,
    detectorMaterial,"Anti-Polarized Detector");

antiPolDetectorDeadLayerLogical = new G4LogicalVolume
    (detectorDeadLayerSolid,detectorMaterial,
     "Anti-Polarized Detector Dead Layer");

antiPolDetectorFilterLogical = new G4LogicalVolume
    (detectorFilterSolid,detectorFilterMaterial,
     "Anti-Polarized Detector Filter");

antiPolDetectorWindowLogical = new G4LogicalVolume
    (detectorWindowSolid,detectorWindowMaterial,
     "Anti-Polarized Detector Window");

//Create the physical volumes
antiPolDetectorPhysical = new G4PVPlacement
    (0,antiPolDetectorPosition,antiPolDetectorLogical,
     "Anti-Polarized Detector",worldLogical,false,0,checkOverlaps);

antiPolDetectorDeadLayerPhysical = new G4PVPlacement
    (0,antiPolDetectorDeadLayerPosition,
     antiPolDetectorDeadLayerLogical,
     "Anti-Polarized Detector Dead Layer",worldLogical,false,0,
     checkOverlaps);

antiPolDetectorFilterPhysical = new G4PVPlacement(0,
```

```
    antiPolDetectorFilterPosition,antiPolDetectorFilterLogical,
    "Anti-Polarized Detector Filter",worldLogical,false,0,
    checkOverlaps);

antiPolDetectorWindowPhysical = new G4PVPlacement(0,
    antiPolDetectorWindowPosition,antiPolDetectorWindowLogical,
    "Anti-Polarized Detector Window",worldLogical,false,0,
    checkOverlaps);

//Create the detector shields

//Create the solids
detectorShieldOutside = new G4Box("Detector Shield Outside",
    0.5*collimatorWidth,0.5*collimatorWidth,
    0.5*detectorShieldThickness);
detectorShieldInside = new G4Tubs("Detector Shield Inside",
    0,detectorRadius,0.6*detectorShieldThickness,0,360.*deg);
detectorShieldSolid = new G4SubtractionSolid("Detector Shield",
    detectorShieldOutside,detectorShieldInside);

//Create the logical volumes
polDetectorShieldLogical = new G4LogicalVolume(detectorShieldSolid,
    detectorShieldMaterial,"Polarized Detector Shield");

antiPolDetectorShieldLogical = new G4LogicalVolume
    (detectorShieldSolid,detectorShieldMaterial,
    "Anti-Polarized Detector Shield");

//Create the physical volumes
polDetectorShieldPhysical = new G4PVPlacement
    (polDetectorShieldTransform,polDetectorShieldLogical,
    "Polarized Detector Shield",worldLogical,false,0,
    checkOverlaps);

antiPolDetectorShieldPhysical = new G4PVPlacement(0,
    antiPolDetectorShieldPosition,antiPolDetectorShieldLogical,
    "Anti-Polarized Detector Shield",worldLogical,false,
    0,checkOverlaps);

//Set the logical volumes for detection purposes
thisWorldVolume = worldLogical;
thisSecondaryTargetVolume = secondaryTargetLogical;
thisSampleVolume = sampleLogical;
thisPolDetectorVolume = polDetectorLogical;
thisAntiPolDetectorVolume = antiPolDetectorLogical;
```

```

thisWorldPhysicalVolume = worldPhysical;

//Set up the detectors
polScorer = new G4MultiFunctionalDetector("Pol");
G4SDManager::GetSDMpointer()->AddNewDetector(polScorer);
G4SDManager::GetSDMpointer()->SetVerboseLevel(0);
polDetectorLogical->SetSensitiveDetector(polScorer);

G4PSEnergyDeposit* polEDep = new G4PSEnergyDeposit("eDep");
polScorer->RegisterPrimitive(polEDep);

antiPolScorer = new G4MultiFunctionalDetector("AntiPol");
G4SDManager::GetSDMpointer()->AddNewDetector(antiPolScorer);
G4SDManager::GetSDMpointer()->SetVerboseLevel(0);
antiPolDetectorLogical->SetSensitiveDetector(antiPolScorer);

G4PSEnergyDeposit* antiPolEDep = new G4PSEnergyDeposit("eDep");
antiPolScorer->RegisterPrimitive(antiPolEDep);

//Return the physical world at the end of the method
return worldPhysical;
}

//Method run to change the collimator sizes from the messenger
void DetectorConstruction::SetNewCollimators
(G4ThreeVector newCollimatorRadius)
{
    thisCollimator1Radius = newCollimatorRadius.getX()*cm;
    thisCollimator2Radius = newCollimatorRadius.getY()*cm;
    thisCollimator3Radius = newCollimatorRadius.getZ()*cm;

    collimator1Inside->SetOuterRadius(thisCollimator1Radius);
    collimator2Inside->SetOuterRadius(thisCollimator2Radius);
    collimator3Inside->SetOuterRadius(thisCollimator3Radius);
}

//Method run to modify the trace element or its ppm
void DetectorConstruction::SetNewTraceElement
(G4String newElement, G4double newPPM)
{
    //Get the nist manager, for looking up materials
    G4NistManager* nist = G4NistManager::Instance();

    thisTraceElement = nist->FindOrBuildMaterial(newElement);
    thisTraceElementPPM = newPPM;
}

```

```

G4double density = sampleBaseMaterial->GetDensity()*
    (1-thisTraceElementPPM/1.e6) +
    thisTraceElement->GetDensity()*thisTraceElementPPM/1.e6;

sampleMaterial = new G4Material
    ("Sample",sampleBaseMaterial->GetDensity(),2);
sampleMaterial->AddMaterial
    (sampleBaseMaterial,1-thisTraceElementPPM/1.e6);
sampleMaterial->AddMaterial
    (thisTraceElement,thisTraceElementPPM/1.e6);

sampleLogical->SetMaterial(sampleMaterial);
}

//Method run to modify the secondary target or its thickness
void DetectorConstruction::SetNewSecondaryTarget
    (G4String newElement, G4double newThickness)
{
    //Get the nist manager, for looking up materials
    G4NistManager* nist = G4NistManager::Instance();

    thisSecondaryTargetThickness = newThickness*um;
    thisSecondaryTargetMaterial =
        nist->FindOrBuildMaterial(newElement);

    secondaryTargetSolid->SetZHalfLength
        (0.5*thisSecondaryTargetThickness);
    secondaryTargetLogical->SetMaterial(thisSecondaryTargetMaterial);
    secondaryTargetPhysical->SetTranslation(G4ThreeVector(-1.*cm,
        (-1.*cm-thisSecondaryTargetThickness/2./std::sqrt(2.)),
        (1.*cm+thisSecondaryTargetThickness/2./std::sqrt(2.))));
    G4cout << secondaryTargetPhysical->GetTranslation();
}
// *****
//This is the detector messenger header file, this method allows
//modification of the the geometry of the detector setup

#ifndef DetectorMessenger_h
#define DetectorMessenger_h 1

#include "G4UI messenger.hh"

class DetectorConstruction;
class G4UIcmdWithoutParameter;
class G4UIcmdWithADouble;
class G4UIcmdWith3Vector;

```

```

class G4UIcmdWithAString;
class G4UIDirectory;

//Detector messenger class
class DetectorMessenger: public G4UImessenger
{
    public:
        DetectorMessenger(DetectorConstruction*);
        ~DetectorMessenger();

        void SetNewValue (G4UIcommand*, G4String newValues);

    private:
        DetectorConstruction* thisDetectorConstruction;
        G4UIDirectory* thisDetectorDirectory;
        G4UIcmdWith3Vector* thisCollimatorChangeCmd;
        G4UIcmdWithoutParameter* thisGeometryChangeCmd;
        G4UIcmdWithADouble* thisPPMChangeCmd;
        G4UIcmdWithADouble* thisSecondaryTargetThicknessChangeCmd;
        G4UIcmdWithAString* thisTraceElementChangeCmd;
        G4UIcmdWithAString* thisSecondaryTargetChangeCmd;
        G4ThreeVector thisCollimatorRadius;
        G4double thisTraceElementPPM;
        G4double thisSecondaryTargetThickness;
        G4String thisTraceElement;
        G4String thisSecondaryTarget;
};

#endif
// *****
//This is the detector messenger class file, this method allows
//modification of the the geometry of the detector setup

//This is used to change the collimator sizes, and change the ppm of
//trace element in the sample. Trace element choice is defined in
//detector construction, which implements this messenger

//Add header files
#include "DetectorMessenger.hh"

#include "DetectorConstruction.hh"
#include "PrimaryGeneratorAction.hh"

#include "G4UIcmdWithoutParameter.hh"
#include "G4UIcmdWithADouble.hh"
#include "G4UIcmdWith3Vector.hh"

```

```

#include "G4UIcmdWithAString.hh"
#include "G4UIDirectory.hh"
#include "G4SystemOfUnits.hh"
#include "G4RunManager.hh"
#include "g4root.hh"
#include "G4IStore.hh"

#include <sstream>

//Constructor, extends G4UImessenger
DetectorMessenger::DetectorMessenger(DetectorConstruction* det)
  : G4UImessenger(),
  thisDetectorConstruction(det),thisCollimatorRadius
  (G4ThreeVector(1.*cm,1.*cm,1.*cm)),thisTraceElementPPM(0),
  thisTraceElement("G4_Fe"),thisSecondaryTargetThickness(50.*um),
  thisSecondaryTarget("G4_Mo")
{
  //Set the command directory, use detector instead of geometry
  //because geometry is already taken
  thisDetectorDirectory = new G4UIDirectory ("/detector/");

  //This is used to rebuild the geometry, required
  thisGeometryChangeCmd = new G4UIcmdWithoutParameter
    ("/detector/rebuild",this);

  //Define the collimator change command
  //The collimator sizes 1,2,3 are read off of x,y,z respectively
  //To be safe, the sizes are restricted to mm right now, set in
  //detector construction
  thisCollimatorChangeCmd = new G4UIcmdWith3Vector
    ("/detector/collimator",this);

  //Define the ppm change command
  thisPPMChangeCmd = new G4UIcmdWithADouble("/detector/ppm",this);

  //Define the trace element command and allowable choices
  thisTraceElementChangeCmd = new G4UIcmdWithAString
    ("/detector/element",this);
  thisTraceElementChangeCmd->SetCandidates
    ("G4_Fe G4_K G4_Ca G4_Mn G4_Cu G4_Zn");

  //Define the secondary target thickness change command
  thisSecondaryTargetThicknessChangeCmd = new G4UIcmdWithADouble
    ("/detector/thickness",
    this);

```

```

//Define the secondary target command and allowable choices
thisSecondaryTargetChangeCmd = new G4UIcmdWithAString
    ("/detector/st",this);
thisSecondaryTargetChangeCmd->SetCandidates
    ("G4_Co G4_Cu G4_Zn G4_Mo G4_Sn");
}

//Destructor
DetectorMessenger::~DetectorMessenger()
{
    delete thisDetectorDirectory;
    delete thisCollimatorChangeCmd;
    delete thisGeometryChangeCmd;
    delete thisPPMChangeCmd;
    delete thisTraceElementChangeCmd;
    delete thisSecondaryTargetThicknessChangeCmd;
    delete thisSecondaryTargetChangeCmd;
}

//Called when the commands are passed to the messenger
void DetectorMessenger::SetNewValue
    (G4UIcommand* command, G4String newValues)
{
    //This command must be run for the geometry to be updated
    if (command == thisGeometryChangeCmd)
    {
        //First, set the new values, then update the geometry
        thisDetectorConstruction->SetNewCollimators
            (thisCollimatorRadius);
        thisDetectorConstruction->SetNewTraceElement
            (thisTraceElement,thisTraceElementPPM);
        thisDetectorConstruction->SetNewSecondaryTarget
            (thisSecondaryTarget,thisSecondaryTargetThickness);

        //Get the analysis manager, this will be used for setting the
        //filename
        G4AnalysisManager* analysisManager =
            G4AnalysisManager::Instance();

        //Filename must have no decimal places, or else the ascii file
        //won't save
        std::ostringstream filename;
        filename << "Collimators " << thisCollimatorRadius.getX()*10
            << "," << thisCollimatorRadius.getY()*10 << ","
            << thisCollimatorRadius.getZ()*10 << "mm, ST "
            << thisSecondaryTarget.substr(3,5) << " "

```

```

        << thisSecondaryTargetThickness << "um Trace "
        << thisTraceElement.substr(3,5) << " "
        << thisTraceElementPPM <<"ppm";

analysisManager->SetFileName(filename.str());

G4RunManager::GetRunManager()->GeometryHasBeenModified();
}
//These are just the other commands, set the new values to be
//stored in this class but don't update them until the geometry
//change command is run
else if (command == thisCollimatorChangeCmd)
{
    thisCollimatorRadius = thisCollimatorChangeCmd->
        GetNew3VectorValue(newValues);
}
else if (command == thisPPMChangeCmd)
{
    thisTraceElementPPM = thisPPMChangeCmd->
        GetNewDoubleValue(newValues);
}
else if (command == thisTraceElementChangeCmd)
{
    thisTraceElement = newValues;
}
else if (command == thisSecondaryTargetThicknessChangeCmd)
{
    thisSecondaryTargetThickness =
        thisSecondaryTargetThicknessChangeCmd->
        GetNewDoubleValue(newValues);
}
else if (command == thisSecondaryTargetChangeCmd)
{
    thisSecondaryTarget = newValues;
}
}
// *****
//This is the event action header file, used for performing tasks before
//or after an event. An event is any interaction, particle generation, etc.

#ifndef EventAction_h
#define EventAction_h 1

#include "G4UserEventAction.hh"
#include "globals.hh"
#include "G4THitsMap.hh"

```

```
class G4event;

//Event action class
class EventAction : public G4UserEventAction
{
    public:
        EventAction();
        virtual ~EventAction();

        virtual void BeginOfEventAction(const G4Event* event);
        virtual void EndOfEventAction(const G4Event* event);

    protected:
        G4int poleDepID;
        G4int antiPoleDepID;
        G4THitsMap<G4double>* eventPoleDep;
        G4THitsMap<G4double>* eventAntiPoleDep;
};

#endif
// *****
//This is the event action class file, used for performing tasks before
//or after an event. An event is any interaction, particle generation,
//etc. It is used to calculate the energy deposited in the detectors

//Add header files for events
#include "EventAction.hh"
#include "G4Event.hh"
#include "G4SDManager.hh"
#include "G4HCoofThisEvent.hh"
#include "G4THitsMap.hh"
#include "G4RunManager.hh"
#include "g4root.hh"

//Constructor, extends G4UserEventAction
EventAction::EventAction()
: G4UserEventAction()
{}

//Destructor
EventAction::~EventAction()
{}

//Method accessed before each event happens
void EventAction::BeginOfEventAction(const G4Event* evt)
```

```

{
    //Initialize the sensitive detector
    G4int evtNb = evt->GetEventID();

    if (evtNb == 0)
    {
        G4SDManager* SDMan = G4SDManager::GetSDMpointer();

        polEDepID = SDMan->GetCollectionID("Pol/eDep");
        antiPolEDepID = SDMan->GetCollectionID("AntiPol/eDep");
    }
}

//Method accessed after each event happens
void EventAction::EndOfEventAction(const G4Event* evt)
{
    //Hits collections
    G4HCofThisEvent* HCE = evt->GetHCofThisEvent();
    if(!HCE) return;

    // Get the HitMaps for this event
    eventPolEDep = (G4THitsMap<G4double>*)(HCE->GetHC(polEDepID));
    eventAntiPolEDep = (G4THitsMap<G4double>*)(HCE->
        GetHC(antiPolEDepID));

    // Zero out the variables
    G4double polEDep = 0.;
    G4double antiPolEDep = 0.;

    std::map<G4int,G4double>::iterator itr;
    G4AnalysisManager* analysisManager = G4AnalysisManager::Instance();

    // Get the total energy deposited in this event
    if (eventPolEDep->GetSize()>0)
    {
        for (itr = eventPolEDep->GetMap()->begin(); itr != eventPolEDep
            ->GetMap()->end(); itr++)
        {
            polEDep = *(itr->second);
        }
        analysisManager->FillH1(37,polEDep);
    }

    // Get the total energy deposited in this event in the ACD
    if(eventAntiPolEDep->GetSize()>0)
    {

```

```

    for (itr = eventAntiPolEDep->GetMap()->begin(); itr !=
        eventAntiPolEDep->GetMap()->end(); itr++)
    {
        antiPolEDep = *(itr->second);
    }
    analysisManager->FillH1(38,antiPolEDep);
}
}
// *****
//This is the physics list header file, which sets up the physics list

#ifndef PhysicsList_h
#define PhysicsList_h 1

#include "G4VModularPhysicsList.hh"

class G4VPhysicsConstructor;

//Physics list class
class PhysicsList: public G4VModularPhysicsList
{
public:
    PhysicsList();
    ~PhysicsList();

    virtual void ConstructParticle();
    virtual void ConstructProcess();

    virtual void SetCuts();
    void SetCutForGamma(G4double);
    void SetCutForElectron(G4double);

private:
    G4String thisPhysicsListName;
    G4VPhysicsConstructor* thisPhysicsList;
    G4double thisCutForGamma;
    G4double thisCutForElectron;
};

#endif
// *****
//This is the physics list file, which sets up the physics list
//Currently, the polarized EM livermore files are used

#include "PhysicsList.hh"

```

```
#include "G4EmLivermorePolarizedPhysics.hh"
#include "G4LossTableManager.hh"
#include "G4UnitsTable.hh"
#include "G4SystemOfUnits.hh"
#include "G4ProcessManager.hh"
#include "G4ParticleTable.hh"

//Constructor, extends G4ModularPhysicsList
PhysicsList::PhysicsList() : G4VModularPhysicsList(),
    thisPhysicsList(0)
{
    //Setup the loss table manager
    G4LossTableManager::Instance();

    //Pick the low energy livermore polarized physics package
    thisPhysicsListName = G4String("Low Energy EM Physics");
    thisPhysicsList = new G4EmLivermorePolarizedPhysics();

    //Set the default cut values
    G4double defaultCutValue = 500.*nm;
    thisCutForGamma = defaultCutValue;
    thisCutForElectron = defaultCutValue;

    //Set the list to be quiet
    SetVerboseLevel(0);
}

//Destructor
PhysicsList::~PhysicsList()
{
    delete thisPhysicsList;
}

//Define the particles

// Bosons
#include "G4ChargedGeantino.hh"
#include "G4Geantino.hh"
#include "G4Gamma.hh"

// leptons
#include "G4Electron.hh"
#include "G4Positron.hh"

#include "G4MuonPlus.hh"
#include "G4MuonMinus.hh"
```

```
// Mesons
#include "G4PionPlus.hh"
#include "G4PionMinus.hh"

#include "G4KaonPlus.hh"
#include "G4KaonMinus.hh"

// Baryons
#include "G4Proton.hh"
#include "G4AntiProton.hh"
#include "G4Neutron.hh"
#include "G4AntiNeutron.hh"

// Nuclei
#include "G4Deuteron.hh"
#include "G4Triton.hh"
#include "G4Alpha.hh"
#include "G4GenericIon.hh"

//Methodcalled to construct the particles
void PhysicsList::ConstructParticle()
{
    //Pseudo-particles
    G4Geantino::GeantinoDefinition();
    G4ChargedGeantino::ChargedGeantinoDefinition();

    //Gamma
    G4Gamma::GammaDefinition();

    //Leptons
    G4Electron::ElectronDefinition();
    G4Positron::PositronDefinition();
    G4MuonPlus::MuonPlusDefinition();
    G4MuonMinus::MuonMinusDefinition();

    //Mesons
    G4PionPlus::PionPlusDefinition();
    G4PionMinus::PionMinusDefinition();
    G4KaonPlus::KaonPlusDefinition();
    G4KaonMinus::KaonMinusDefinition();

    //Baryons
    G4Proton::ProtonDefinition();
    G4AntiProton::AntiProtonDefinition();
    G4Neutron::NeutronDefinition();
}
```

```
G4AntiNeutron::AntiNeutronDefinition();

//Ions
G4Deuteron::DeuteronDefinition();
G4Triton::TritonDefinition();
G4Alpha::AlphaDefinition();
G4GenericIon::GenericIonDefinition();
}

//Include the EM process options
#include "G4EmProcessOptions.hh"

//Construct the processes
void PhysicsList::ConstructProcess()
{

    //Get the EM options, so we can add fluorescence
    G4EmProcessOptions emOptions;

    //Set high and low energy points
    emOptions.SetMinEnergy(100*eV);
    emOptions.SetMaxEnergy(10*TeV);
    emOptions.SetDEDXBinning(12*20);
    emOptions.SetLambdaBinning(12*20);

    //Build CSDA range
    emOptions.SetBuildCSDARange(true);
    emOptions.SetMaxEnergyForCSDARange(10*TeV);
    emOptions.SetDEDXBinningForCSDARange(12*20);

    //Add fluorescence
    emOptions.SetDeexcitationActiveRegion("World",true,true,true);
    emOptions.SetFluo(true);
    emOptions.SetAuger(true);
    emOptions.SetPIXE(true);

    //Allow cutoffs
    emOptions.SetSubCutoff(true);

    //Add transportation and construct the list
    AddTransportation();
    thisPhysicsList->ConstructProcess();
}

//Method for setting cuts for the list
void PhysicsList::SetCuts()
```

```

{
    //Set cut values for gamma and e-/e+
    SetCutValue(thisCutForGamma, "gamma");
    SetCutValue(thisCutForElectron, "e-");
    SetCutValue(thisCutForElectron, "e+");
}

//Method for setting cuts for gammas
void PhysicsList::SetCutForGamma(G4double cut)
{
    thisCutForGamma = cut;
    SetParticleCuts(thisCutForGamma, G4Gamma::Gamma());
}

//Method for setting cuts for electrons and positrons
void PhysicsList::SetCutForElectron(G4double cut)
{
    thisCutForElectron = cut;
    SetParticleCuts(thisCutForElectron, G4Electron::Electron());
    SetParticleCuts(thisCutForElectron, G4Positron::Positron());
}
// *****
//This is the primary generator action header file, this method
//controls the generation of particles

#ifdef PrimaryGeneratorAction_h
#define PrimaryGeneratorAction_h 1

#include "G4VUserPrimaryGeneratorAction.hh"

class G4GeneralParticleSource;
class G4Event;

//Primary generator action class
class PrimaryGeneratorAction : public G4VUserPrimaryGeneratorAction
{
public:
    PrimaryGeneratorAction();
    virtual ~PrimaryGeneratorAction();

    virtual void GeneratePrimaries(G4Event*);

protected:
    G4GeneralParticleSource* thisParticleGun;
};

```

```
#endif
// *****
//This is the primary generator action class file, this method controls
//the generation of particles

//This class is mostly not used anymore, set things via macro files

//Add header files
#include "PrimaryGeneratorAction.hh"

#include "EventAction.hh"

#include "G4RunManager.hh"
#include "G4GeneralParticleSource.hh"
#include "G4ParticleTable.hh"
#include "G4ParticleDefinition.hh"
#include "Randomize.hh"
#include "g4root.hh"
#include "G4SystemOfUnits.hh"
#include "G4PhysicalConstants.hh"

//Constructor, extends G4VUserPrimaryGeneratorAction
PrimaryGeneratorAction::PrimaryGeneratorAction()
    : G4VUserPrimaryGeneratorAction(),
      thisParticleGun(0)
{
    //Define the particle gun, for our purposes use a generic particle
    //source
    thisParticleGun = new G4GeneralParticleSource();

    //Define the gamma, which is what we will use as the main particle
    G4ParticleTable* particleTable =
        G4ParticleTable::GetParticleTable();
    G4String particleName;
    G4ParticleDefinition* particle =
        particleTable->FindParticle(particleName="gamma");
    thisParticleGun->SetParticleDefinition(particle);
}

//Destructor
PrimaryGeneratorAction::~PrimaryGeneratorAction()
{
    delete thisParticleGun;
}

//Method required to generate the particles
```

```

void PrimaryGeneratorAction::GeneratePrimaries(G4Event* anEvent)
{
    //Generate the particle
    thisParticleGun->GeneratePrimaryVertex(anEvent);
}
// *****
//This is the run header file, this method controls the runs as they
//are produced

#ifdef Run_h
#define Run_h 1

#include "G4Run.hh"

//Run class
class Run : public G4Run
{
public:
    Run();
    virtual ~Run();
};

#endif
// *****
//This is the run class file, this method controls the runs as they are
//produced

//Currently this code does nothing, but could be used to modify runs

//Add header files for runs
#include "Run.hh"

//Constructor, extends G4Run
Run::Run()
: G4Run()
{}

//Destructor
Run::~~Run()
{}
// *****
//This is the run action header file, this method controls what happens
//at the beginning and ends of runs

#ifdef RunAction_h

```

```
#define RunAction_h 1

#include "G4UserRunAction.hh"
#include "G4String.hh"

class G4Run;

//Run action class
class RunAction : public G4UserRunAction
{
public:
    RunAction();
    virtual ~RunAction();

    virtual G4Run* GenerateRun();
    virtual void BeginOfRunAction(const G4Run*);
    virtual void EndOfRunAction(const G4Run*);

private:
    G4String fileName;
};

#endif
// *****
//This is the run action class file, this method controls what happens
//at the beginning and ends of runs

//This class currently controls the histograms and file writing

//Add header files
#include "RunAction.hh"
#include "Run.hh"

#include "G4RunManager.hh"
#include "G4UnitsTable.hh"
#include "G4SystemOfUnits.hh"
#include "g4root.hh"

#include <sstream>

//Constructor, extends G4UserRunAction
RunAction::RunAction()
    : G4UserRunAction()
{
    //Set printing event number every 100000 events, to check if it is
    //still running
}
```

```
G4RunManager::GetRunManager()->SetPrintProgress(100000);

//Create analysis manager
G4AnalysisManager* analysisManager = G4AnalysisManager::Instance();

//Create directories
analysisManager->SetVerboseLevel(2);
analysisManager->SetFirstHistoId(1);

// Creating histograms
analysisManager->CreateH1("1","Energy of the particles Produced",
    300, 0., 150*keV);
analysisManager->SetH1Ascii(1, true);

analysisManager->CreateH1
    ("2","Energy of the ST XRF particles in Polarized Detector",
    300, 0., 150*keV);
analysisManager->SetH1Ascii(2, true);

analysisManager->CreateH1("3",
    "Energy of the ST XRF particles in Anti-Polarized Detector",
    300, 0., 150*keV);
analysisManager->SetH1Ascii(3, true);

analysisManager->CreateH1("4",
    "Energy of the Sample XRF particles in Polarized Detector",
    300, 0., 150*keV);
analysisManager->SetH1Ascii(4, true);

analysisManager->CreateH1("5",
    "Energy of the Sample XRF particles in Anti-Polarized Detector"
    ,300, 0., 150*keV);
analysisManager->SetH1Ascii(5, true);

analysisManager->CreateH1("6",
    "Energy of the scattered particles in Polarized Detector",
    300, 0., 150*keV);
analysisManager->SetH1Ascii(6, true);

analysisManager->CreateH1("7",
    "Energy of the scattered particles in Anti-Polarized Detector",
    300, 0., 150*keV);
analysisManager->SetH1Ascii(7, true);

analysisManager->CreateH1("8",
    "Energy of the extra particles in Polarized Detector",
```

```
    300, 0., 150*keV);
analysisManager->SetH1Ascii(8, true);

analysisManager->CreateH1("9",
    "Energy of the extra particles in Anti-Polarized Detector",
    300, 0., 150*keV);
analysisManager->SetH1Ascii(9, true);

analysisManager->CreateH1("10", "Produced Polarization X",
    100, -1., 1.);
analysisManager->SetH1Ascii(10, true);

analysisManager->CreateH1("11", "Produced Polarization Y",
    100, -1., 1.);
analysisManager->SetH1Ascii(11, true);

analysisManager->CreateH1("12", "Produced Polarization Z",
    100, -1., 1.);
analysisManager->SetH1Ascii(12, true);

analysisManager->CreateH1("13", "ST XRF Polarization X in Sample",
    100, -1., 1.);
analysisManager->SetH1Ascii(13, true);

analysisManager->CreateH1("14", "ST XRF Polarization Y in Sample",
    100, -1., 1.);
analysisManager->SetH1Ascii(14, true);

analysisManager->CreateH1("15", "ST XRF Polarization Z in Sample",
    100, -1., 1.);
analysisManager->SetH1Ascii(15, true);

analysisManager->CreateH1("16", "Scatter Polarization X in Sample",
    100, -1., 1.);
analysisManager->SetH1Ascii(16, true);

analysisManager->CreateH1("17", "Scatter Polarization Y in Sample",
    100, -1., 1.);
analysisManager->SetH1Ascii(17, true);

analysisManager->CreateH1("18", "Scatter Polarization Z in Sample",
    100, -1., 1.);
analysisManager->SetH1Ascii(18, true);

analysisManager->CreateH1("19",
    "ST XRF Polarization X in Polarized Detector", 100, -1., 1.);
```

```
analysisManager->SetH1Ascii(19, true);

analysisManager->CreateH1("20",
    "ST XRF Polarization Y in Polarized Detector", 100, -1., 1.);
analysisManager->SetH1Ascii(20, true);

analysisManager->CreateH1("21",
    "ST XRF Polarization Z in Polarized Detector", 100, -1., 1.);
analysisManager->SetH1Ascii(21, true);

analysisManager->CreateH1("22",
    "ST XRF Polarization X in Anti-Polarized Detector",
    100, -1., 1.);
analysisManager->SetH1Ascii(22, true);

analysisManager->CreateH1("23",
    "ST XRF Polarization Y in Anti-Polarized Detector",
    100, -1., 1.);
analysisManager->SetH1Ascii(23, true);

analysisManager->CreateH1("24",
    "ST XRF Polarization Z in Anti-Polarized Detector",
    100, -1., 1.);
analysisManager->SetH1Ascii(24, true);

analysisManager->CreateH1("25",
    "Sample XRF Polarization X in Polarized Detector",
    100, -1., 1.);
analysisManager->SetH1Ascii(25, true);

analysisManager->CreateH1("26",
    "Sample XRF Polarization Y in Polarized Detector",
    100, -1., 1.);
analysisManager->SetH1Ascii(26, true);

analysisManager->CreateH1("27",
    "Sample XRF Polarization Z in Polarized Detector",
    100, -1., 1.);
analysisManager->SetH1Ascii(27, true);

analysisManager->CreateH1("28",
    "Sample XRF Polarization X in Anti-Polarized Detector",
    100, -1., 1.);
analysisManager->SetH1Ascii(28, true);

analysisManager->CreateH1("29",
```

```
        "Sample XRF Polarization Y in Anti-Polarized Detector",
        100, -1., 1.);
analysisManager->SetH1Ascii(29, true);

analysisManager->CreateH1("30",
        "Sample XRF Polarization Z in Anti-Polarized Detector",
        100, -1., 1.);
analysisManager->SetH1Ascii(30, true);

analysisManager->CreateH1("31",
        "Scatter Polarization X in Polarized Detector", 100, -1., 1.);
analysisManager->SetH1Ascii(31, true);

analysisManager->CreateH1("32",
        "Scatter Polarization Y in Polarized Detector", 100, -1., 1.);
analysisManager->SetH1Ascii(32, true);

analysisManager->CreateH1("33",
        "Scatter Polarization Z in Polarized Detector", 100, -1., 1.);
analysisManager->SetH1Ascii(33, true);

analysisManager->CreateH1("34",
        "Scatter Polarization X in Anti-Polarized Detector",
        100, -1., 1.);
analysisManager->SetH1Ascii(34, true);

analysisManager->CreateH1("35",
        "Scatter Polarization Y in Anti-Polarized Detector",
        100, -1., 1.);
analysisManager->SetH1Ascii(35, true);

analysisManager->CreateH1("36",
        "Scatter Polarization Z in Anti-Polarized Detector",
        100, -1., 1.);
analysisManager->SetH1Ascii(36, true);

analysisManager->CreateH1("37", "Polarized Detector eDep",
        300, 0., 150*keV);
analysisManager->SetH1Ascii(37, true);

analysisManager->CreateH1("38", "Antipolarized Detector eDep",
        300, 0., 150*keV);
analysisManager->SetH1Ascii(38, true);
}

//Deconstructor
```

```

RunAction::~RunAction()
{
    delete G4AnalysisManager::Instance();
}

//Returns a run when called
G4Run* RunAction::GenerateRun()
{
    return new Run;
}

//Called at the beginning of a run
void RunAction::BeginOfRunAction(const G4Run* run)
{
    long seeds[2];
    time_t systime = time(NULL);
    seeds[0] = (long) systime;
    seeds[1] = (long) (systime*G4UniformRand());
    CLHEP::HepRandom::setTheSeeds(seeds);

    // Get analysis manager
    G4AnalysisManager* analysisManager = G4AnalysisManager::Instance();

    // Open an output file, the filename is set in detector messenger
    fileName = analysisManager->GetFileName();

    std::ostringstream newFileName;
    newFileName << fileName.substr(0,47) << " - " << run->GetRunID()
        << ".root";
    analysisManager->OpenFile(newFileName.str());

    //Don't save the random seed
    G4RunManager::GetRunManager()->SetRandomNumberStore(false);
}

//Called at the end of a run
void RunAction::EndOfRunAction(const G4Run* run)
{
    //Safety check to make sure the run happened
    G4int nofEvents = run->GetNumberOfEvent();
    if (nofEvents == 0) return;

    //Save histograms
    G4AnalysisManager* analysisManager = G4AnalysisManager::Instance();
    analysisManager->Write();
    analysisManager->CloseFile();
}

```

```

}
// *****
//This is the stepping action header file, this method controls what
//happens at the beginning and ends of each step

#ifdef SteppingAction_h
#define SteppingAction_h 1

#include "G4UserSteppingAction.hh"

class EventAction;
class G4LogicalVolume;

//Stepping action class
class SteppingAction : public G4UserSteppingAction
{
public:
    SteppingAction(EventAction* eventAction);
    virtual ~SteppingAction();

    virtual void UserSteppingAction(const G4Step*);

private:
    int hitFlag;
    G4LogicalVolume* thisWorldVolume;
    G4LogicalVolume* thisSecondaryTargetVolume;
    G4LogicalVolume* thisSampleVolume;
    G4LogicalVolume* thisPolDetectorVolume;
    G4LogicalVolume* thisAntiPolDetectorVolume;
};

#endif
// *****
//This is the stepping action class file, this method controls what
//happens at the beginning and ends of each step

//This class is used for filling the histograms, when x-rays pass
//certain points. The proper energy deposited is done in event action

//Add header files
#include "SteppingAction.hh"
#include "EventAction.hh"
#include "DetectorConstruction.hh"

#include "G4Step.hh"

```

```
#include "G4Event.hh"
#include "G4RunManager.hh"
#include "G4LogicalVolume.hh"
#include "g4root.hh"

#include "G4VSolid.hh"

//Constructor, extends G4UserSteppingAction
SteppingAction::SteppingAction(EventAction* eventAction)
    : G4UserSteppingAction(),
      thisWorldVolume(0),thisSecondaryTargetVolume(0),thisSampleVolume(0)
      ,thisPolDetectorVolume(0),thisAntiPolDetectorVolume(0),hitFlag(0)
{}

//Destructor
SteppingAction::~SteppingAction()
{}

//This method is called after a step has been completed, allowing you
//to collect the information from the x-ray as it passes through
//certain logical volumes
void SteppingAction::UserSteppingAction(const G4Step* step)
{
    //Check to see if the volumes have been initialized, if not, then
    //initialize them
    if (!thisWorldVolume)
    {
        const DetectorConstruction* thisDetectorConstruction
            = static_cast<const DetectorConstruction*>
              (G4RunManager::GetRunManager()->
               GetUserDetectorConstruction());

        thisWorldVolume = thisDetectorConstruction->GetWorldVolume();
        thisSecondaryTargetVolume = thisDetectorConstruction->
            GetSecondaryTargetVolume();
        thisSampleVolume = thisDetectorConstruction->GetSampleVolume();
        thisPolDetectorVolume = thisDetectorConstruction->
            GetPolDetectorVolume();
        thisAntiPolDetectorVolume = thisDetectorConstruction->
            GetAntiPolDetectorVolume();
    }

    //Get the volume that the current step is in
    G4LogicalVolume* volume
        = step->GetPreStepPoint()->GetTouchableHandle()->GetVolume()->
        GetLogicalVolume();
}
```

```
//Check to see that it is still an x-ray, we don't want to record
//electrons
if(step->GetPostStepPoint()->GetCharge() != 0) return;

//Get the energy of the x-ray and its polarization
G4double energy = step->GetPreStepPoint()->GetKineticEnergy();
G4ThreeVector pol = step->GetPreStepPoint()->GetPolarization();

//Get the analysis manager, to put values into histograms
G4AnalysisManager* analysisManager = G4AnalysisManager::Instance();

//Get the volume the particle originated in
const G4LogicalVolume* origVol = step->GetTrack()->
    GetLogicalVolumeAtVertex();

//Flag choices
//0 for new photon in worldVolume
//1 for hit ST
//2 for hit Sample
if(step->GetPreStepPoint()->GetGlobalTime() == 0 && origVol ==
    thisWorldVolume)
{
    hitFlag = 0;
}

//If we are in the sample, then plug in the values for the
//secondary target else if we are in the polarized detector,
//plug in the values for the sample else if we are in the
//antipolarized detector, grab those values too else ignore
//completely
if (volume == thisSecondaryTargetVolume && hitFlag == 0)
{
    analysisManager->FillH1(1,step->GetTrack()->
        GetVertexKineticEnergy());
    analysisManager->FillH1(10,pol.getX());
    analysisManager->FillH1(11,pol.getY());
    analysisManager->FillH1(12,pol.getZ());
    hitFlag = 1;
}
else if (volume == thisSampleVolume && hitFlag == 1)
{
    hitFlag = 2;
    //If it was from the secondary target, it's ST XRF
    if (origVol == thisSecondaryTargetVolume)
    {
```

```
        analysisManager->FillH1(13,pol.getX());
        analysisManager->FillH1(14,pol.getY());
        analysisManager->FillH1(15,pol.getZ());
    }
    //If it was from the world, it is an original photon
    else if (origVol == thisWorldVolume)
    {
        //Removes argon Peaks from fluorescence of air
        if (pol.isNear(G4ThreeVector(0,0,0)))
        {
            analysisManager->FillH1(13,pol.getX());
            analysisManager->FillH1(14,pol.getY());
            analysisManager->FillH1(15,pol.getZ());
        }
        //Otherwise, it is a scattered photon
        else
        {
            analysisManager->FillH1(16,pol.getX());
            analysisManager->FillH1(17,pol.getY());
            analysisManager->FillH1(18,pol.getZ());
        }
    }
}
//We're in the polarized detector, save the energies and sample
//polarizations
else if (volume == thisPolDetectorVolume && hitFlag == 2)
{
    hitFlag = 0;
    //ST XRF
    if (origVol == thisSecondaryTargetVolume)
    {
        analysisManager->FillH1(2,energy);
        analysisManager->FillH1(19,pol.getX());
        analysisManager->FillH1(20,pol.getY());
        analysisManager->FillH1(21,pol.getZ());
    }
    //Sample XRF
    else if (origVol == thisSampleVolume)
    {
        analysisManager->FillH1(4,energy);
        analysisManager->FillH1(25,pol.getX());
        analysisManager->FillH1(26,pol.getY());
        analysisManager->FillH1(27,pol.getZ());
    }
}
//World volume is from source
else if (origVol == thisWorldVolume)
```

```
{
    analysisManager->FillH1(6,energy);
    analysisManager->FillH1(31,pol.getX());
    analysisManager->FillH1(32,pol.getY());
    analysisManager->FillH1(33,pol.getZ());
}
//Catches extra particles, used for error detection
else
{
    analysisManager->FillH1(8,energy);
}
}
//We're in the anti polarized detector, save the energies and
//sample polarizations
else if (volume == thisAntiPolDetectorVolume && hitFlag == 2)
{
    hitFlag = 0;
    //ST XRF
    if (origVol == thisSecondaryTargetVolume)
    {
        analysisManager->FillH1(3,energy);
        analysisManager->FillH1(22,pol.getX());
        analysisManager->FillH1(23,pol.getY());
        analysisManager->FillH1(24,pol.getZ());
    }
    //Sample XRF
    else if (origVol == thisSampleVolume)
    {
        analysisManager->FillH1(5,energy);
        analysisManager->FillH1(28,pol.getX());
        analysisManager->FillH1(29,pol.getY());
        analysisManager->FillH1(30,pol.getZ());
    }
    //World volume is from source
    else if (origVol == thisWorldVolume)
    {
        analysisManager->FillH1(7,energy);
        analysisManager->FillH1(34,pol.getX());
        analysisManager->FillH1(35,pol.getY());
        analysisManager->FillH1(36,pol.getZ());
    }
    //Catches extra particles, used for error detection
    else
    {
        analysisManager->FillH1(9,energy);
    }
}
```

```

    }
}
// *****

```

Here is the list of macro files that go with the Geant4 code.

```

#####
#init.mac
#Written by: Eric Johnston
#Latest Update 2017-04-28
#Here are the macro files for the tri-axial code
/control/verbose 2
/control/saveHistory
#Uncomment for visualization, makes it very slow
#/control/execute vis.mac
/control/execute gps.mac
#####
#
# Use these open statements to open selected visualization
/vis/open OGL 800x800-0+0
/vis/viewer/set/autoRefresh false
/vis/verbose errors

# Draw geometry
/vis/drawVolume

# Specify view angle
/vis/viewer/set/viewpointVector -1 0 0
/vis/viewer/set/lightsVector -1 0 0

# Specify style (surface, wireframe, auxiliary edges,...)
/vis/viewer/set/style wireframe
/vis/viewer/set/auxiliaryEdge true
/vis/viewer/set/lineSegmentsPerCircle 100

# Draw smooth trajectories at end of event, showing trajectory points
# as markers 2 pixels wide
/vis/scene/add/trajectories smooth

# To superimpose all of the events from a given run:
/vis/scene/endOfEventAction accumulate
/vis/set/textColour

# Axes, scale, etc.
/vis/scene/add/axes
/vis/scene/add/eventID

```

```
/vis/scene/add/date

# Frame
/vis/set/colour red
/vis/set/lineWidth 2
/vis/scene/add/frame
/vis/set/colour
/vis/set/lineWidth

# To get nice view
/vis/geometry/set/visibility World 0 false
/vis/viewer/set/style surface
/vis/viewer/set/hiddenMarker true
/vis/viewer/set/viewpointThetaPhi 70 180

# Re-establish auto refreshing and verbosity:
/vis/viewer/set/autoRefresh true
/vis/verbose warnings
#####
#gps.mac
#This macro runs the specified voltage
/control/execute G4Spectra\30.mac
/control/execute geometry.mac
#####
#30.mac
#Example input histogram
/control/execute G4Spectra\setup.mac
/gps/hist/point 0 0
/gps/hist/point 0.0005 0
/gps/hist/point 0.001 0
/gps/hist/point 0.0015 0
/gps/hist/point 0.002 0
/gps/hist/point 0.0025 0
/gps/hist/point 0.003 0
/gps/hist/point 0.0035 0.0028435
/gps/hist/point 0.004 0.0069529
/gps/hist/point 0.0045 0.012392
/gps/hist/point 0.005 0.018237
/gps/hist/point 0.0055 0.023622
/gps/hist/point 0.006 0.027864
/gps/hist/point 0.0065 0.030825
/gps/hist/point 0.007 0.032511
/gps/hist/point 0.0075 0.033144
/gps/hist/point 0.008 0.033017
/gps/hist/point 0.0085 0.2177
/gps/hist/point 0.009 0.031165
```

```
/gps/hist/point 0.0095 0.11051
/gps/hist/point 0.01 0.093775
/gps/hist/point 0.0105 0.019047
/gps/hist/point 0.011 0.018652
/gps/hist/point 0.0115 0.034798
/gps/hist/point 0.012 0.014843
/gps/hist/point 0.0125 0.013652
/gps/hist/point 0.013 0.013384
/gps/hist/point 0.0135 0.013064
/gps/hist/point 0.014 0.012701
/gps/hist/point 0.0145 0.012305
/gps/hist/point 0.015 0.011887
/gps/hist/point 0.0155 0.011453
/gps/hist/point 0.016 0.011009
/gps/hist/point 0.0165 0.010559
/gps/hist/point 0.017 0.010105
/gps/hist/point 0.0175 0.0096521
/gps/hist/point 0.018 0.0092004
/gps/hist/point 0.0185 0.0087529
/gps/hist/point 0.019 0.0083092
/gps/hist/point 0.0195 0.00787
/gps/hist/point 0.02 0.0074367
/gps/hist/point 0.0205 0.0070087
/gps/hist/point 0.021 0.0065869
/gps/hist/point 0.0215 0.0061715
/gps/hist/point 0.022 0.0057614
/gps/hist/point 0.0225 0.0053575
/gps/hist/point 0.023 0.0049597
/gps/hist/point 0.0235 0.0045678
/gps/hist/point 0.024 0.0041811
/gps/hist/point 0.0245 0.0038004
/gps/hist/point 0.025 0.0034259
/gps/hist/point 0.0255 0.0030567
/gps/hist/point 0.026 0.0026928
/gps/hist/point 0.0265 0.0023351
/gps/hist/point 0.027 0.0019832
/gps/hist/point 0.0275 0.001637
/gps/hist/point 0.028 0.001297
/gps/hist/point 0.0285 0.00096305
/gps/hist/point 0.029 0.00063549
/gps/hist/point 0.0295 0.00031454
/gps/hist/point 0.03 2.6046e-05
#####
#setup.mac
/gps/source/clear
/gps/source/add 1
```

```
/gps/particle gamma
/gps/pos/type Plane
/gps/pos/shape Circle
/gps/pos/centre -1 -1 -1 cm
/gps/pos/radius 0.5 cm
/gps/ang/type iso
/gps/ang/mintheta 85 deg
/gps/ang/maxtheta 95 deg
/gps/ang/minphi 265 deg
/gps/ang/maxphi 275 deg
/gps/ang/rot1 0 1 0
/gps/ang/rot2 0 0 1
/gps/polarization 1 0 0
/gps/ene/type User
/gps/hist/type energy
#####
#geometry.mac
#set your secondary target and thickness
/detector/st G4_Cu
/detector/thickness 87
#set your collimator widths
/detector/collimator 0.5 0.5 0.5
#add a material to the sample
/detector/element G4_Fe
/detector/ppm 100
/detector/rebuild
#allows you to overcome the integer limit for good statistics
/control/loop run.mac i 0 999 1
#####
#run.mac
/run/beamOn 10000000
#####
```

# Bibliography

- [1] Tatjana Paunesku, Stefan Vogt, Jrg Maser, Barry Lai, and Gayle Woloschak. X-ray fluorescence microprobe imaging in biology and medicine. *Journal of Cellular Biochemistry*, 99(6):1489–1502, 2006. ISSN 1097-4644. doi: 10.1002/jcb.21047. URL <http://dx.doi.org/10.1002/jcb.21047>.
- [2] Sahar Darvish-Molla, Alia Al-Ebraheem, and Michael J. Farquharson. The identification and differentiation of secondary colorectal cancer in human liver tissue using x-ray fluorescence, coherent scatter spectroscopy, and multivariate analysis. *Applied Spectroscopy*, 68(1):79–87, 2014-01-01T00:00:00. doi: doi:10.1366/13-07047. URL <http://www.ingentaconnect.com/content/sas/sas/2014/00000068/00000001/art00015>.
- [3] M. J. Farquharson and K. Geraki. The use of combined trace element xrf and edxrd data as a histopathology tool using a multivariate analysis approach in characterizing breast tissue. *X-Ray Spectrometry*, 33(4):240–245, 2004. ISSN 1097-4539. doi: 10.1002/xrs.684. URL <http://dx.doi.org/10.1002/xrs.684>.
- [4] J. Als-Nielsen and D. McMorrow. *Elements of Modern X-ray Physics*. Wiley, United Kingdom, 2nd edition, 2011.

- 
- [5] B. Beckhoff, B. Kanngiesser, N. Langhoff, R. Wedell, and H. Wolff. *Handbook of Practical X-Ray Fluorescence Analysis*. Springer, Germany, 1st edition, 2006.
- [6] Utz Kramar. Advances in energy-dispersive x-ray fluorescence. *Journal of Geochemical Exploration*, 58(1):73–80, 2 1997.
- [7] J. Heckel, M. Haschk, M. Brumme, and R. Schindler. Principles and applications of energy-dispersive x-ray fluorescence analysis with polarized radiation. *Journal of Analytical Atomic Spectrometry*, 7:281, 1992. URL <http://pubs.rsc.org/en/content/articlehtml/1992/ja/ja9920700281>.
- [8] S. Pessanha, A. Guilherme, and M. L. Carvalho. Comparison of matrix effects on portable and stationary xrf spectrometers for cultural heritage samples. *Applied Physics A*, 97(2):497–505, 2009. ISSN 1432-0630. doi: 10.1007/s00339-009-5251-x. URL <http://dx.doi.org/10.1007/s00339-009-5251-x>.
- [9] A. Guilherme, A. Cavaco, M. Pessanha, M. Costa, and M. L. Carvalho. Comparison of portable and stationary x-ray fluorescence spectrometers in the study of ancient artefacts. *X-Ray Spectrometry*, 37:444, 2008. URL <http://onlinelibrary.wiley.com/doi/10.1002/xrs.1016/pdf>.
- [10] Zhan. X. Application of polarized edxrf in geochemical sample analysis and comparison with wdxrf. *X-Ray Spectrometry*, 34:207, 2005. URL <http://onlinelibrary.wiley.com/doi/10.1002/xrs.794/abstract>.
- [11] A. A. Espinosa, J. Reyes-Herrera, J. Miranda, F. Mercado, M. A. Veytia,

- M. Cuautle, and J. I. Cruz. Development of an x-ray fluorescence spectrometer for environmental science applications. *Instrumentation Science and Technology*, 40(6):603–617, 11/01; 2013/01 2012. URL <http://dx.doi.org/10.1080/10739149.2012.693560>. doi: 10.1080/10739149.2012.693560; M3: doi: 10.1080/10739149.2012.693560; 23.
- [12] Z. Spolnik, K. Belikov, K. van Meel, E. Adriaenssens, F. de Roeck, and R. van Grieken. Optimization of Measurement Conditions of an Energy Dispersive X-ray Fluorescence Spectrometer with High-Energy Polarized Beam Excitation for Analysis of Aerosol Filters. *Applied Spectroscopy*, 59:1465–1469, December 2005. doi: 10.1366/000370205775142647.
- [13] Andrew C Todd. L-shell x-ray fluorescence measurements of lead in bone: system development. *Physics in Medicine and Biology*, 47(3):507, 2002. URL <http://stacks.iop.org/0031-9155/47/i=3/a=311>.
- [14] M.J. Farquharson, R.D. Luggar, and R.D. Speller. Multivariate calibration for quantitative analysis of edxrd spectra from a bone phantom. *Applied Radiation and Isotopes*, 48(8):1075 – 1082, 1997. ISSN 0969-8043. doi: [http://dx.doi.org/10.1016/S0969-8043\(96\)00328-4](http://dx.doi.org/10.1016/S0969-8043(96)00328-4). URL <http://www.sciencedirect.com/science/article/pii/S0969804396003284>.
- [15] A.W. Allday and M.J. Farquharson. Minimum detectable limits of measuring bone mineral density using an energy dispersive x-ray diffraction system. *Radiation Physics and Chemistry*, 61(36):589 – 592, 2001. ISSN 0969-806X. doi: [http://dx.doi.org/10.1016/S0969-806X\(01\)00341-3](http://dx.doi.org/10.1016/S0969-806X(01)00341-3). URL [http://dx.doi.org/10.1016/S0969-806X\(01\)00341-3](http://dx.doi.org/10.1016/S0969-806X(01)00341-3).

- [//www.sciencedirect.com/science/article/pii/S0969806X01003413](http://www.sciencedirect.com/science/article/pii/S0969806X01003413). 8th International Symposium on Radiation Physics - {ISRP8}.
- [16] W. Heitler. *The Quantum Theory of Radiation*. Dover Books on Physics. Dover Publications, 1954. ISBN 9780486645582.
- [17] M. J. Berger and J. H. Hubbel. Xcom: Photon cross sections on a personal computer., 1987.
- [18] R. Ryon. Polarization for background reduction in edxf - the technique that does indeed work. *International Centre for Diffraction Data*, 46:53, 2003. URL [http://www.icdd.com/resources/axa/vol46/V46\\_53.pdf](http://www.icdd.com/resources/axa/vol46/V46_53.pdf).
- [19] S. Agostinelli, J. Allison, K. Amako, J. Apostolakis, H. Araujo, and et al. Geant4 physics reference manual, 2016.
- [20] X-ray tube image. URL <http://medicalimagingworld.weebly.com/uploads/1/2/1/5/12157935/3807192.png?588>.
- [21] Burkhard Beckhoff, Birgit Kanngiesser, Norbert Langhoff, Reiner Wedell, and Helmut Wolff. *Handbook of Practical X-ray Fluorescence Analysis*. Springer-Verlag Berlin Heidelberg, 1st edition, 2006.
- [22] T. G. Dzubay, B. V. Jarrett, and J. M. Jaklevic. Background reduction in x-ray fluorescence spectra using polarization. *Nuclear Instruments and Methods*, 115 (1):297–299, 2/15 1974.
- [23] C. G. Barkla. Bakerian lecture: On x-rays and the theory of radiation.

- Philosophical Transactions of the Royal Society of London. Series A, Containing Papers of a Mathematical or Physical Character*, 217:315–360, 1918. URL <http://www.jstor.org/stable/91124>.
- [24] Charles G. Barkla. Polarised rontgen radiation. *Philosophical Transactions of the Royal Society of London. Series A, Containing Papers of a Mathematical or Physical Character*, 204:467–479, 1905. URL <http://www.jstor.org/stable/90923>.
- [25] J. Hudson. Polarization of compton-scattered gamma rays, paper 277, honors theses, western michigan university, 1968.
- [26] W. Swoboda, B. Beckhoff, B. Kanngiesser, and J. Scheer. Use of al<sub>2</sub>o<sub>3</sub> as a barkla scatterer for the production of polarized excitation radiation in edxrf. *X-Ray Spectrometry*, 22:317, 1993. URL <http://onlinelibrary.wiley.com/doi/10.1002/xrs.1300220426/abstract>.
- [27] E. M. Johnston, S. H. Byun, and M. J. Farquharson. Determination of optimal metallic secondary target thickness, collimation, and exposure parameters for x-ray tube-based polarized edxrf. *X-Ray Spectrometry*, 46(2):93–101, 2017.
- [28] K Geraki, M J Farquharson, and D A Bradley. X-ray fluorescence and energy dispersive x-ray diffraction for the quantification of elemental concentrations in breast tissue. *Physics in Medicine and Biology*, 49(1):99, 2004. URL <http://stacks.iop.org/0031-9155/49/i=1/a=007>.
- [29] P. Standzenieks and E. Selin. Background reduction of x-ray fluorescence spectra

- in a secondary target energy dispersive spectrometer. *Nuclear Instruments and Methods*, 165(1):63–65, 9/15 1979.
- [30] K. Cranley, B. Gilmore, G. Fogarty, and L. Desponds. Ipem report 78, 1997.
- [31] C. Zarkadas, A. Karydas, and T. Paradellis. Theoretical study of a secondary target xrf setup at different operational tube voltages. *X-Ray Spectrometry*, 30:99, 2001. URL <http://onlinelibrary.wiley.com/doi/10.1002/xrs.479/abstract>.
- [32] C. Zarkadas and A. Karydas. Fundamental parameters approach in tube-excited secondary target xrf setups: Comparison between theory and experiment. *X-Ray Spectrometry*, 33:447, 2004. URL <http://onlinelibrary.wiley.com/doi/10.1002/xrs.747/abstract>.
- [33] K. Bisgard, J. Laursen, and B. Nielsen. Energy-dispersive xrf spectrometry using secondary radiation in a cartesian geometry. *X-Ray Spectrometry*, 10(1), 2005. URL <http://onlinelibrary.wiley.com/doi/10.1002/xrs.1300100106/pdf>.
- [34] S. Agostinelli, J. Allison, K. Amako, J. Apostolakis, H. Araujo, and et al. Geant4. *Nucl. Instrum. Methods*, 2003.
- [35] L. C. Alves, A. P. Jesus, and M. A. Reis. Experimental x-ray peak-shape determination for a si(li) detector. *Nuclear Instruments and Methods in Physics Research Section B: Beam Interactions with Materials and Atoms*, 109110(0): 129–133, 4/1 1996.
- [36] J. L. Campbell and J. A. Maxwell. A cautionary note on the use of the hypermet tailing function in x-ray spectrometry with si(li) detectors. *Nuclear Instruments*

- and Methods in Physics Research Section B: Beam Interactions with Materials and Atoms*, 129(2):297–299, 7/1 1997.
- [37] J. L. Campbell, B. M. Millman, J. A. Maxwell, A. Perujo, and W. J. Teesdale. Analytic fitting of monoenergetic peaks from si(li) x-ray spectrometers. *Nuclear Instruments and Methods in Physics Research Section B: Beam Interactions with Materials and Atoms*, 9(1):71–79, 4 1985.
- [38] D. W. Marquardt. An algorithm for least-squares estimation of nonlinear parameters. *Journal of the Society for Industrial and Applied Mathematics*, 11(2): 431, 1963. URL <http://www.jstor.org/stable/2098941>.
- [39] L. Ruby and J.B. Rechen. A simpler approach to the geometrical efficiency of a parallel-disk source and detector system. *Nuclear Instruments and Methods*, 58(2):345 – 346, 1968. ISSN 0029-554X. doi: [http://dx.doi.org/10.1016/0029-554X\(68\)90491-6](http://dx.doi.org/10.1016/0029-554X(68)90491-6). URL <http://www.sciencedirect.com/science/article/pii/0029554X68904916>.
- [40] P. Obloinsky and I. Ribansk. The solid angle subtended at a disk source by a non-parallel disk detector. *Nuclear Instruments and Methods*, 94(1):187 – 188, 1971. ISSN 0029-554X. doi: [http://dx.doi.org/10.1016/0029-554X\(71\)90359-4](http://dx.doi.org/10.1016/0029-554X(71)90359-4). URL <http://www.sciencedirect.com/science/article/pii/0029554X71903594>.
- [41] Elaine A Ryan and Michael J Farquharson. Breast tissue classification using x-ray scattering measurements and multivariate data analysis. *Physics in Medicine and Biology*, 52(22):6679, 2007. URL <http://stacks.iop.org/0031-9155/52/i=22/a=009>.

- [42] National Research Council Canada. Luts-1: Non defatted lobster hepatopancreas. URL [http://www.nrc-cnrc.gc.ca/eng/solutions/advisory/crm/certificates/luts\\_1.html](http://www.nrc-cnrc.gc.ca/eng/solutions/advisory/crm/certificates/luts_1.html).
- [43] M.L. Lord, F.E. McNeill, J.L. Grfe, M.D. Noseworthy, and D.R. Chettle. A phantom-based feasibility study for detection of gadolinium in bone in-vivo using x-ray fluorescence. *Applied Radiation and Isotopes*, 112:103 – 109, 2016. ISSN 0969-8043. doi: <http://dx.doi.org/10.1016/j.apradiso.2016.03.021>. URL <http://www.sciencedirect.com/science/article/pii/S0969804316301142>.
- [44] M Chamberlain, J L Grfe, Aslam, S H Byun, D R Chettle, L M Egden, G M Orchard, C E Webber, and F E McNeill. The feasibility of in vivo quantification of bone-fluorine in humans by delayed neutron activation analysis: a pilot study. *Physiological Measurement*, 33(2):243, 2012. URL <http://stacks.iop.org/0967-3334/33/i=2/a=243>.
- [45] Sahar Darvish-Molla. The identification and differentiation between normal and secondary colorectal cancer in human liver tissue using x-ray techniques, m.sc. thesis, 2012.
- [46] E. Dao. X-ray fluorescence measurement of iron accumulation in skin as a surrogate marker for iron levels in critical organs and total body iron burden, m.sc. thesis, 2017.
- [47] J E Jackson. *A User's Guide to Principal Components*. John Wiley and Sons, 1st edition, 1991.
- [48] I T Jolliffe. *Principal Component Analysis*. Springer, 2nd edition, 2002.

- [49] M. Garg, R. Garg, and K. Malmqvist. Measurements of l x-ray fluorescence cross sections in rare-earth elements. *Journal of Physics B: Atomic and Molecular Physics*, 20:3705, 1987. URL [http://iopscience.iop.org/0022-3700/20/15/018/pdf/0022-3700\\_20\\_15\\_018.pdf](http://iopscience.iop.org/0022-3700/20/15/018/pdf/0022-3700_20_15_018.pdf).